Dissertation

submitted to the

Combined Faculty of Mathematics, Engineering and Natural Sciences

of Heidelberg University, Germany

for the degree of

Doctor of Natural Sciences

Put forward by

Hugo Freitas

born in: Aveiro, Portugal

Oral examination: 06-02-2025

Prompt Gamma-Ray Spectroscopy: Advancing Dose, Range, and Tumor Monitoring in Particle Therapy

Referees: Prof. Dr. João Seco

Prof. Dr. Christian Karger

Abstract

Random and systematic uncertainties pose significant risks in charged ion therapy, potentially leading to under-dosing of tumors or over-dosing of healthy tissues. This study introduces a novel method to measure dose, range, and tumor localization in real time using prompt gamma-ray spectroscopy (PGS) and gadolinium-based contrast agents (GBCA). Gd accumulates in tumors and emits prompt gamma-rays and X-rays upon irradiation. While neutron capture by Gd is well-understood, this research highlights the role of particle-induced X-ray emission (PIXE) as a key interaction affecting the Gd signal. The study benchmarks and improves PGS models for Monte Carlo simulations and experimentally investigates the spectral response of Gd under varying particle beam conditions. The underlying physics of characteristic X-rays was analyzed, and the feasibility of using Gd and PGS for accurate dose and tumor monitoring was explored. This work lays the groundwork for the clinical use of PGS with GBCAs, offering a promising approach to enhance accuracy in particle therapy.

Zusammenfassung

Zufällige und systematische Ungenauigkeiten stellen erhebliche Risiken in der Schwerionentherapie dar, da sie zur Unterdosierung im Tumor oder zur Überdosierung im gesunden Gewebe führen können. Diese Studie stellt eine neue Methode vor, Dosis, Reichweite und Tumorlokalisierung mithilfe von ”prompt gamma-ray spectroscopy (PGS)” und Kontrastmitteln auf Gadoliniumbasis (GBCA) in Echtzeit zu messen. Gd reichert sich in Tumoren an und emittiert Gamma- und Röntgenstrahlung bei Bestrahlung. Während Neutroneneinfang von Gd gut verstanden ist, unterstreicht diese Arbeit die Rolle von Partikel-induzierten Röntgenemissionen als Schlüsselinteraktion im Einfluss auf das Gd Signal. Diese Studie vergleicht und verfeinert PGS Modelle für Monte Carlo Simulationen und untersucht experimentell das Spektrum von Gd unter verschiedenen Einstellungen des Teilchenstrahls. Die zugrundeliegende Physik der charakteristischen Röntgenstrahlung wurde analysiert und die Umsetzbarkeit des Einsatzes von Gd und PGS zur akkuraten Dosis- und Tumorkontrolle wurde untersucht. Diese Arbeit legt den Grundstein für den klinischen Einsatz vom PGS mit GBCAs mit einer vielversprechenden Herangehensweise, die Genauigkeit in der Partikeltherapie zu verbessern.

Contents

List of Figures

List of Tables

Chapter 1

Introduction

It is widely recognized that particle beams offer superior physical selectivity compared to photons. This advantage is due to their unique dose deposition, which reaches its maximum (the *Bragg* peak) at an energy-dependent depth before abruptly falling off. These characteristics allow for reduced entrance and exit doses compared to conventional *X-ray* therapy. This enhanced precision in targeting tumors allows for greater conformity to the tumor region while significantly sparing healthy tissues. Moreover, due to the higher local ionization density of heavy ions, particle therapy offers increased biological effectiveness, increasing the tumor control probability of treatments. These advantages have driven the growth of this modality in medicine, leading to significant advancements in cancer treatment.

1.1 Motivation

The main argument for particle therapy in reducing the deposited dose to surrounding healthy tissue comes with significant challenges, as the steep dose gradient at the distal edge of the *Bragg* peak makes accurate range determination critical, as errors can profoundly impact the dose received by healthy tissue. Patient mispositioning, organ motion, and anatomical changes between and within treatment fractions (e.g., tumor shrinkage, weight loss, or cavity filling) are uncertainties that can lead to inefficient dose delivery to the target and overexposure of organs at risk to undesirable radiation. Furthermore, the treatment plans are also susceptible to errors, such as inaccuracies in tumor delineation and stopping power estimations.

As shown in Figure 1.1, safety margins are commonly applied in standard clinical practice to expand the treated volume, statistically accounting for these uncertainties. However, the use of safety margins can hinder the full potential of particle therapy, as shown in Figure 1.2, where suboptimal treatment strategies, such as multi-field or patched-field plans, are employed at the expense of potentially superior single-field plans. Alternatively, to this and

other solutions, working groups such as AAPM TG-40 and AAPM TG-62 (Kutcher et al. [1994], of Physicists in Medicine et al. [2005]), along with many researchers, support the application of *in vivo* particle therapy monitoring techniques such as positron emission tomography (PET), prompt gamma imaging (PGI), particle imaging and others. Successful implementation of these methods can minimize safety margins and allow new beam directions, enhancing the overall efficiency of the treatment.

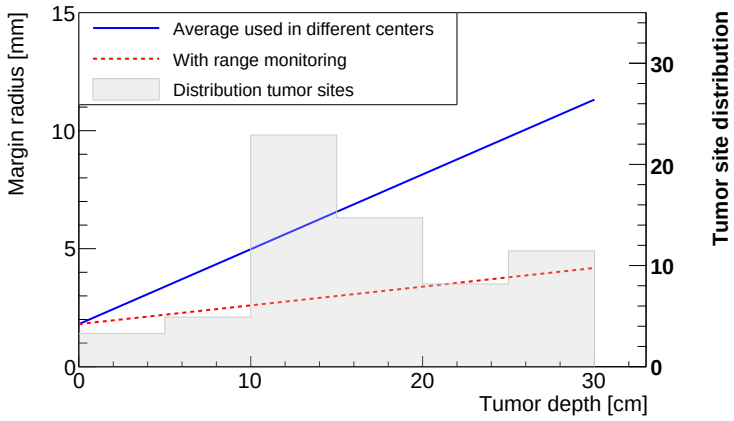

Figure 1.1. Averaged margins (solid, blue) used at different proton and ion therapy centers. Data adapted from Greilich [2017]. The distribution of tumor depths for patients is also shown as a histogram. The dashed red line represents the goal of range monitoring: reducing the margins used in treatment plans.

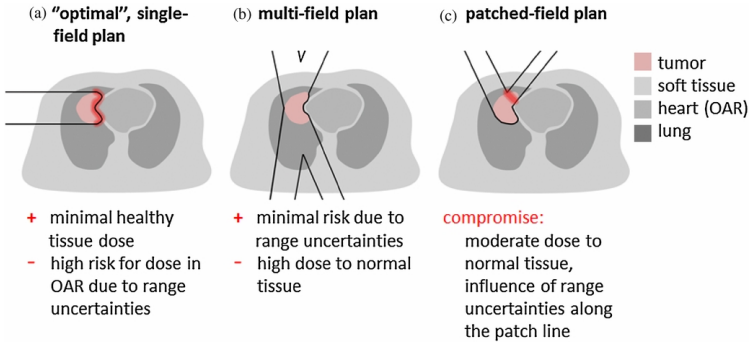

Figure 1.2. Planning strategies in proton therapy and their sensitivity to range uncertainties. Adapted from Knopf and Lomax [2013].

To be successfully integrated into clinical practice, these techniques must satisfy specific criteria: they must not interfere with the treatment beam or the patient, should be easily mountable, must not prolong treatment time, and should be compatible with the features of the therapy facility (e.g., beam time structure). Unlike particle imaging, PET and PGI are well-established methods that have already achieved clinical application (Moglioni et al.

[2022], Richter et al. [2016]). Both rely on secondary radiation induced by the particle beam to provide range and indirect dose measurements.

The main challenge with PET, which relies on gamma-rays emitted from positron annihilation, is its limited effectiveness due to delays in signal acquisition (e.g., the time required to transport the patient to a PET scanner). These delays result in reduced detection of radiation induced by short-lived isotopes due to their rapid decay and biological washout (Handrack et al. [2017]). Efforts to improve PET include the developing in-beam PET systems, which aim to capture signals quasi-instantaneously (Bisogni et al. [2017], Ferrero et al. [2018]). In contrast, PGI measures prompt radiation emitted on a nanosecond timescale, providing real-time feedback. Additionally, PGI signals are less affected by secondary interactions, background noise, or biological effects. However, the main challenge with PGI lies in detecting secondary photons, which can have energies up to $10\,\mathrm{MeV}$.

Various approaches for PGI have been proposed, utilizing features such as counts, time-of-flight, and energy. Among the most promising solutions for in-vivo particle therapy monitoring is prompt gamma-ray spectroscopy (PGS). Studies such as Hueso-González et al. [2018] have demonstrated that PGS achieves high statistical precision, with a mean accuracy of $\pm 1\,\mathrm{mm}$ for range measurements. In addition to its role as a range monitoring technique, PGS offers the unique capability to measure the elemental composition of tissues (Magalhaes Martins et al. [2020a], Polf et al. [2013]) and can be used as a beam probe in favorable anatomic sites (Freitas et al. [2021], Magalhaes Martins et al. [2021]). Furthermore, Tian et al. [2018] demonstrated the reliability of using prompt gamma-rays for *in vivo* dose monitoring. These findings demonstrate the potential of PGS for *in vivo* monitoring applications. Notably, while previous studies have primarily focused on using PGS for range measurements, direct dose measurements using PGS have yet to be reported.

1.2 Project's Description

This study introduces a novel method to simultaneously measure dose, range, and tumor localization in real-time and *in vivo* using PGS and gadolinium-based contrast agents (GBCA). Widely used in magnetic resonance imaging, these agents accumulate within tumors once administrated to patients. Interestingly, when GBCA is irradiated with a particle beam, the gadolinium (Gd) within the tumor can undergo a series of unique interactions (Gräfe et al. [2014]). While previous understanding has primarily focused on the neutron capture process by Gd, which results in the emission of energy in the forms of electrons, prompt gamma-rays, and characteristics *X-rays*, this study has focused on an additional interaction: the particle-induced *X-ray* emission (PIXE) from the Gd.

Gräfe et al. [2010, 2011] demonstrated the feasibility of using GBCA for *in vivo* studies, and Van Delinder et al. [2020] later proposed its use for tumor localization. These studies are grounded in the understanding that the emission of characteristics *X-rays* and prompt gamma-rays from Gd occurs through neutron capture. The unique properties of Gd make GBCA a valuable material for applications where tumor regions are studied in contrast to healthy tissue, particularly given that Gd has one of the most significant cross sections for thermal neutron capture when compared to other elements. A similar outcome is expected for PIXE. However, this interaction directly excites the electronic shells of Gd, also resulting in *X-ray* emission.

Building on this knowledge, the approach in this study aims to use these physical properties as a surrogate for dose and tumor localization measurements. Furthermore, it seeks to integrate these with PGS measurements for range monitoring.

Chapter 2

Theoretical Background

2.1 Physics of Particle Therapy

Particle therapy uses charged ions[1], including protons and heavier ions with kinetic energies of a few MeVs up to approximately $220\,\mathrm{MeV}$ and $430\,\mathrm{MeV/u}$, respectively, to target both superficial and deep-seated tumors effectively. This is achieved through sophisticated facilities capable of delivering mid-relativistic particle beams (velocities $> 50\%$ of the speed of light) with ranges varying from a few millimeters up to $\sim 30\,\mathrm{cm}$ (Haberer et al. [2004]). As they enter an absorbing medium, the charged ions are slowed down by losing their kinetic energy, mainly through inelastic collisions with atomic electrons (electromagnetic *Coulomb* interactions). In addition to energy loss mechanisms, the lateral scattering of charged ions is predominantly due to elastic collisions with atomic nuclei. It is equally important to consider the nuclear reactions between the particles and the targets within the medium. Despite the negligible energy loss associated with these interactions, they induce secondary radiation and nuclear fragmentation, which can be detected to achieve *in vivo* treatment monitoring in particle therapy. This chapter provides a comprehensive understanding of the physical principles underlying particle therapy treatments, focusing on potential mechanisms that can be used for therapy monitoring.

2.1.1 Energy Loss in a Medium

The energy loss of charged ions, which is primarily mediated by inelastic collisions, is a stochastic process. Consequently, due to the probabilistic nature of these interactions, physical models use statistical methods, treating it as a mean energy loss. Bohr [1915] proposed an initial model following Bragg and Kleeman's [1905] initial research on the field. Based on classical collision power, Bohr's theory correlated well with empirical data in in-

[1] In this study, the terms "charged ions" and "particles" are used interchangeably.

termediary energy ranges, but for lower and higher energies, the theory had a significant discrepancy. Subsequently, including quantum mechanical and relativistic effects, Bethe [1930] and Bloch [1933] developed a more accurate model for the mean energy loss. When defined per unit path length (dx), the mean energy loss is commonly known as the linear stopping power (dE/dx) and provided by the Bethe-Bloch equation,

$$-\langle\frac{dE}{dx}\rangle = \rho K \frac{Z}{A}\frac{1}{\beta^2} z^2 \left[\frac{1}{2}\ln\frac{2m_e c^2\beta^2\gamma^2\Delta E_{max}}{I^2} - \beta^2 - \frac{\delta}{2} - \frac{C}{Z}\right] \tag{2.1}$$

$$K = 4\pi N_A r_e^2 m_e c^2 \tag{2.2}$$

where N_A is *Avogadro*'s number, Z and A the atomic number and weight of the target, r_e and m_e the classic electron radius and mass, z and $\beta = v/c$ the atomic number and velocity of the projectile, the density of the medium, $\gamma = 1/\sqrt{1-\beta^2}$ the *Lorentz* factor, I the mean ionization/excitation energy[2], and ΔE_{max} represents the maximum energy a projectile can transfer in a single collision. The additional corrections are characterized by the density correction, $\delta/2$, and shell correction, C/Z, terms. The former accounts for the reduction in the effective electric field (polarization of the medium) experienced by ultra relativistic projectiles, whereas the latter accounts for the fact that electrons are not stationary and is more important for lower velocities.

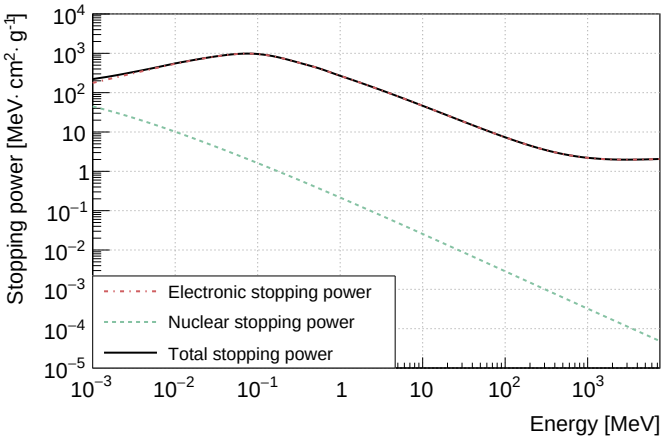

Figure 2.1. Total (solid, black), electronic (dash-dotted, red), nuclear (dashed, green) stopping power as function kinetic energy for protons shot into A-150 tissue equivalent plastic target. Data reproduced from the NIST database (M.J.Berger et al. [2017]).

A more practical representation is the mass stopping power, which accounts for the medium's density and is expressed in units of $\mathrm{MeVcm^2g^{-1}}$. In addition to the collision

[2]The mean ionization/excitation energy, I, is determined empirically from measurements. In practice, I is typically estimated using the ICRU and NIST tables, although empirical mathematical approximations are also possible.

stopping power (electronic), the total stopping power also includes radiative processes (nuclear stopping power), such as *Bremsstrahlung*. However, these processes have a negligible effect in the context of particle therapy, as shown in Figure 2.1, which depicts the total sopping power as a function of the kinetic energy of protons. The total stopping power is a propriety of the absorbing medium. It can divided into three distinct regions: at lower energies, increases and reaches a peak, in the intermediate energy range, decreases as a function of $1/\beta^2$. Finally, the last terms of equation 2.1 influence the behavior of the total stopping power at relativistic energies.

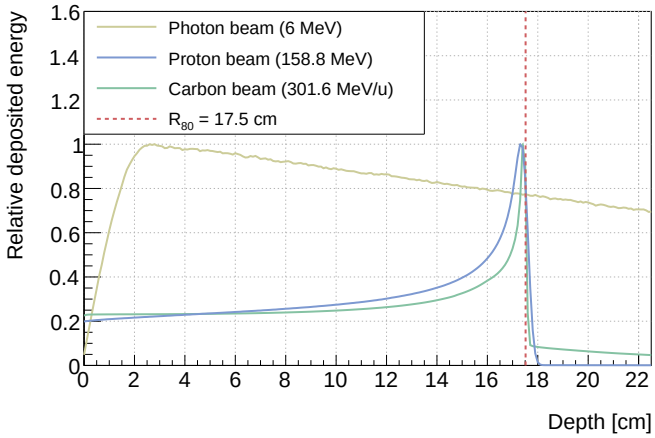

Figure 2.2. Relative deposited energy in an A-150 tissue-equivalent phantom as a function of depth for a photon beam of 6 MeV (solid, orange) compared to proton (solid, blue) and carbon beams (solid, green) of 158.8 MeV and 301.6MeV/u (or a range of 17.5cm, dashed, red), respectively. Data obtained from *Monte Carlo* simulations (`GEANT4 v11.1.2`, Agostinelli et al. [2003])

The rate of energy loss per unit area (usually with units of $keV/\mu m$) caused by ionizing interactions is then inversely proportional to the velocity of the particles. Consequently, as the particles slow down, the rate at which they lose their energy increases, resulting in a sharp peak near the end-of-range followed by a distal fall-off, known as the *Bragg* peak. This behavior can be observed in figure 2.2 for different charged ions and has a vital role in the rationale of using particle therapy as opposed to conventional radiotherapy.

Particle Range

The total distance a beam of charge ions travels within a tissue, regardless of the directions of motion, can be defined as a (projected) range, R (or $R_{Projected}$), and is the position where 50% of the initial number of particles come to at rest, or experimentally, at the depth along the distal fall-off of the *Bragg* peak where the relative energy deposited reaches 80% (R_{80})

of its maximum value (Paganetti [2012]). In particle therapy, however, the range is defined in terms of its mean due to statistical fluctuations in energy loss caused by inelastic interactions that the particles undergo. This results in slight differences in the total distance traveled by particles with the same energy, a concept known as range straggling. To account for these phenomena, Seltzer and Berger [1983] introduced the *Continuous Slowing Down Approximation* (CSDA) range. The approximation is that the charged ions between collisions travel small distances, losing their energy continuously to the tissue. In dosimetry, this energy transfer is known as linear energy transfer (LET). High LET radiation, typical of heavy charged particles, causes concentrated damage to biological tissues, enhancing cancer cell destruction while sparing surrounding healthy tissue.

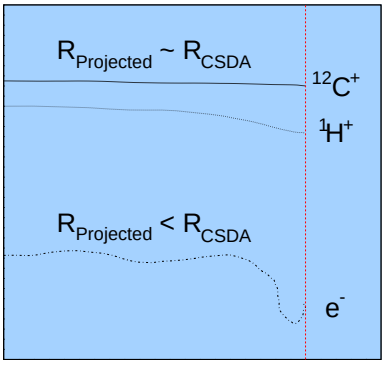

Figure 2.3. Schematic diagram of charged particles traversing an A-150 tissue-equivalent plastic target. The dashed red line denotes the projected range position, while the arc lengths of the black lines represent the CSDA range. Heavy charged particles such as protons (dotted, ${}^{1}H^{+}$) and carbons (solid, ${}^{12}C^{+}$) scatter less than electrons (dash-dotted), resulting in minimal differences between their projected and CSDA ranges.

Figure 2.3 shows the difference between the CSDA and projected range. It can be seen that the CSDA range, $R_{CSDA} \sim R_{Projected}$, for particles commonly used in particle therapy. The CSDA range, R_{CSDA}, can be calculated by integrating the inverse of the total stopping power (S_{tot}) with respect to the energy in the interval from their initial kinetic energy, E_k^{init}, to rest, $E_k = 0$,

$$R_{CSDA} = \int_{E_k^{init}}^{0} -S_{tot}^{-1}\, dE \tag{2.3}$$

Straggling and Multiple Scattering

The CSDA range provides a deterministic approach to estimating the range of charged ions in tissue. However, in particle therapy, it is necessary to consider the stochastic fluctuations of the energy loss of individual ions. These fluctuations, referred to as energy straggling,

cause a broadening of the *Bragg* curve when translated into range as particles move progressively deeper into a tissue. In the limit of a thin target and many collisions, the distribution of these fluctuations becomes *Gaussian* (Ahlen [1980], Lewis [1952]). Its variance, σ_E^2, is related with the variance of range straggling, σ_R^2, by equation 2.4. For a charged ion, σ_R is approximately proportional to R and inversely proportional to the square root of the particle's mass. The latter is a key rationale for the use of heavier ions in particle therapy, allowing for better targeting of the tumor site while maximizing the spare of healthy tissues.

$$\sigma_R^2 = \int_0^{E_k^{init}} \left(\frac{d\sigma_E}{dx}\right) \left(\frac{dE}{dx}\right)^{-3} dE \tag{2.4}$$

Elastic multiple *Coulomb* scattering (MCS) experienced by the charged ions may also alter the range, albeit to a significantly lesser degree. The importance of MCS comes from its effect in the lateral scattering, spreading an initially parallel beam into an approximated *Gaussian* angular distribution (Attix [2008]). Figure 2.4 demonstrates the lateral scattering for protons of different energies and carbon. MCS decreases with particle mass and energy, and it is clinically relevant for particle therapy when treating tumors close to organs at risk (OAR). It plays a significant role in defining the lateral penumbra and contributes to range uncertainties of particle therapy treatments.

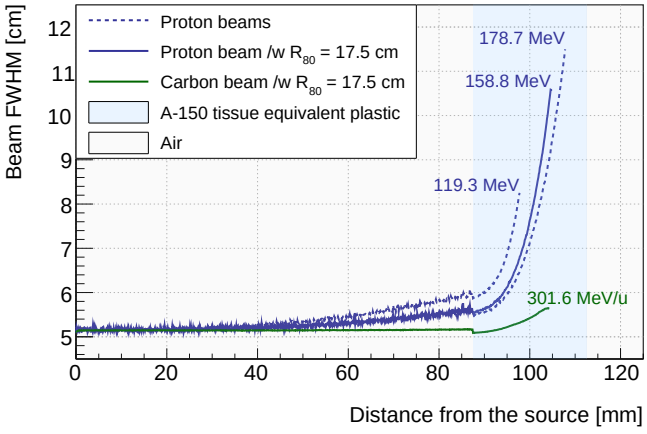

Figure 2.4. Lateral scattering of a proton (solid and dashed, blue) and carbon (solid, green) initially parallel beams of 5 mm full width at half maximum traversing air and then an A-150 tissue-equivalent plastic target. A comparison of the lateral scattering of a proton with that of a carbon ion of the same range (solid lines) shows that heavier charged ions have a lower lateral scattering. Data obtained from *Monte Carlo* simulations (`GEANT4 v11.1.2`, Agostinelli et al. [2003]).

2.1.2 Nuclear Reactions

In addition to the energy loss through *Coulomb* interactions, charged ions also lose energy due to direct interactions with target nuclei. While these nuclear interactions contribute significantly less to overall energy deposition than electromagnetic processes, they play a critical role in range monitoring techniques. In such reactions, physical quantities such as the charge, energy-momentum and angular momentum are conserved (Basdevant et al. [2005]). Figure 2.5 illustrates the primary mechanisms through which a charged ion can undergo a nuclear reaction during particle therapy treatments.

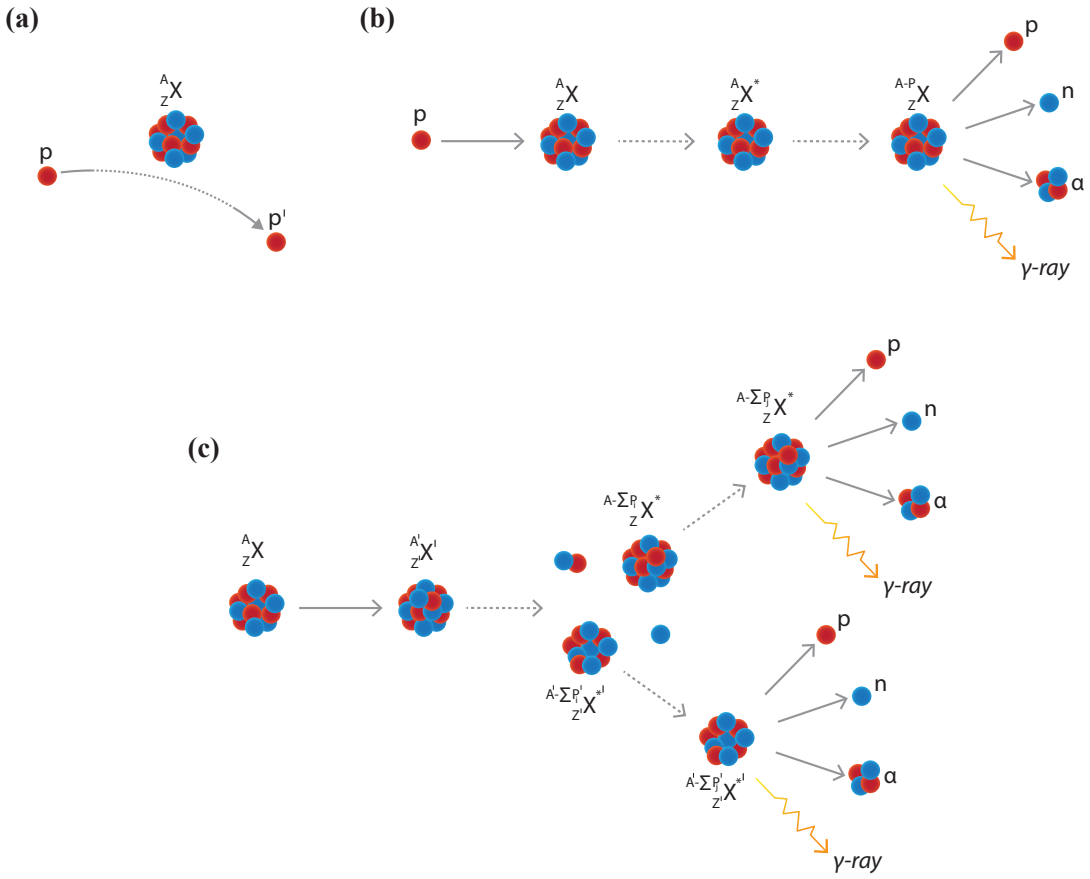

Figure 2.5. Primary mechanisms through which a charged ion can undergo a nuclear reaction during particle therapy treatments: (a) elastic nuclear reactions; (b) inelastic nuclear reaction with single emission of a particle and de-excitation gamma-rays; (c) inelastic nuclear reaction with fragmentation of the projectile.

In the case of elastic nuclear reactions (or MCS), the scattered charged ion exchanges momentum with the target nucleus but remains unchanged, contributing only to the lateral scattering of the particle beam. For an inelastic nuclear reaction to occur, the charged ion needs sufficient energy to overcome the *Coulomb* barrier of the nucleus (Podgoršak et al. [2006]). Additionally, as an endothermic reaction, the nuclear reaction cannot take place unless the energy in center-of-mass exceeds a specific threshold energy, $E_{k,thr}$, approxi-

mated by equation 2.5, where Q-value is the reaction energy, m_p and m_t, the masses of the projectile and target, respectively.

$$E_{k,thr} \sim -Q\left(1 + \frac{m_p}{m_t}\right) \tag{2.5}$$

Inelastic nuclear interactions can be further divided into two categories: reactions where the recoil nucleus remains intact but is left in an excited state, which may later decay by emission of secondary radiation (e.g., prompt gamma-rays); and spallation reactions, in which a high-energy charged ion interacts with the nucleus, leading to ejection of multiple nucleons (e.g., protons, neutrons or fragments). This results in the transformation of the original nuclide into a different one, with the nucleus undergoing significant changes (Newhauser and Zhang [2015]). At the moment, there is no definitive model that accurately describes nuclear interactions. However, various approaches have been developed to simulate these interactions. In *Monte Carlo* simulations, the process is usually divided into four stages. The first is the intra-nuclear cascade, characterized by a fast exchange of energy and momentum. Following the pre-equilibrium phase, the system can form an intermediate, highly excited compound nucleus, in which the total energy of the reaction is distributed among the nucleus. The third is the decay of the compound nucleus through evaporation. Finally, the de-excitation phase of the residual nucleus occurs.

Neutron Induced Reactions

In particle therapy dosimetry, neutron emission is an important by-product of nuclear reactions, as their interactions contribute to the additional dose absorbed by healthy tissue. These neutrons cover a wide range of energies in tissue. Figure 2.6 illustrates this with an example of neutron energy spectra at different depths resulting from proton ($E_{proton} = 158.8\,\text{MeV}$) irradiation of an A-150 tissue equivalent plastic target. Neutrons lose energy primarily by elastic scattering with atomic nuclei such as ${}^1H$. Inelastic scattering is another interaction where neutrons transfer energy to the nucleus, leading to excited states and emission of secondary radiation. As the neutrons slow down, the probability and significance of neutron capture increases inversely with velocity ($1/\beta$), reaching a maximum for thermal neutrons with energies of $0.025\,\text{eV}$. This interaction produces a heavier isotope in an excited state of the same element with an increased mass number, releasing the excess energy by emitting secondary radiation.

Neutron capture by hydrogen, $n + {}^1H \rightarrow {}^2H + \gamma_{2.22\,\text{MeV}}$, is an example of such interaction, where a deuteron is formed, and the binding energy of the deuteron nucleus is emitted, with 100% of probability, as a gamma-ray with an energy of $2.22\,\text{MeV}$. While often considered noise in range monitoring, these gamma-rays can be useful for energy calibration

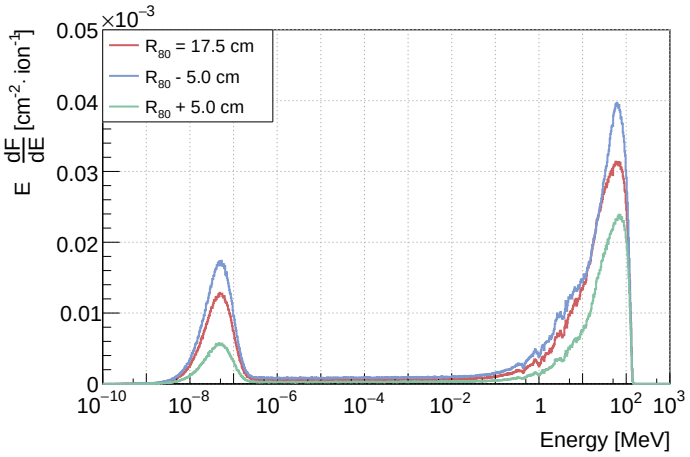

Figure 2.6. Energy-weighted differential neutron fluence spectra at 3 different depths: $R_{80} = 17.5\,\text{cm}$ (solid, red), $R_{80} + 5.0\,\text{cm}$ (solid, green) and $R_{80} - 5.0\,\text{cm}$ (solid, blue), for a proton beam with $158.8\,\text{MeV}$ shot into an A-150 tissue-equivalent phantom. Data obtained from Monte Carlo simulations (GEANT4 v11.1.2, Agostinelli et al. [2003]).

purposes (Hueso-González et al. [2018]). If the neutron capture cross-section is significant, this reaction can also be utilized in neutron capture therapy (NCT). In this case, elements with a high neutron capture cross section, such as ^{10}B and ^{157}Gd, are injected intravenously, intratumorally, or peritumorally. Then, they are irradiated with neutrons to induce neutron capture, resulting in localized release of high LET ionizing radiation, beneficial for targeting cancer cells (Malouff et al. [2021]).

Cross-Section

The cross section, σ, is generally used to describe the collision or interaction of two particles. This quantity measures the probability of a reaction occurring and can be calculated if the particle flux, Φ, the number of reactions per unit time, $N_{reactions}$, and the number of targets, $N_{targets}$ per unit volume are known. In the case of thin targets, σ is given by equation 2.6. Conversely, in *Monte Carlo* simulations, σ is usually calculated using equation 2.7, where λ is the mean free path of the particle and n is the density number of targets.

$$\sigma_{\substack{thin \\ target}} = \frac{N_{reactions}}{\Phi N_{targets}} \tag{2.6}$$

$$\sigma_{\substack{thick \\ target}} = \frac{1}{n\lambda} \tag{2.7}$$

In general, the cross-section varies with both the energy and the angle at which the particle is scattered. Therefore, the total σ can be expressed as an integral over the scattering angle, θ, and the azimuthal angle ϕ, as a double differential cross section as seen in equation 2.8, where $d\Omega = \sin\theta d\theta d\phi$ is the infinitesimal solid angle element.

$$\sigma = \int \int_{\Omega} \frac{d^2\sigma}{dE\, d\Omega}\, d\Omega\, dE \tag{2.8}$$

In the context of nuclear reactions in particle therapy, it is frequently observed that σ for inelastic nuclear interactions between the particles and the tissue rises sharply and then smoothly transits towards a power-law, $\sigma(E) \propto E^{-n}$, or exponential fall off, $\sigma(E) \propto e^{(-\alpha E)}$, at higher energies. Figure 2.7 depicts the values of the proton-carbon and proton-oxygen inelastic cross sections as a function of the proton kinetic energy. In both cases, the inelastic cross section is related to the energy deposited by the particles, and the by-products of these interactions (e.g.: de-excitation gamma-rays) play a significant role in beam monitoring.

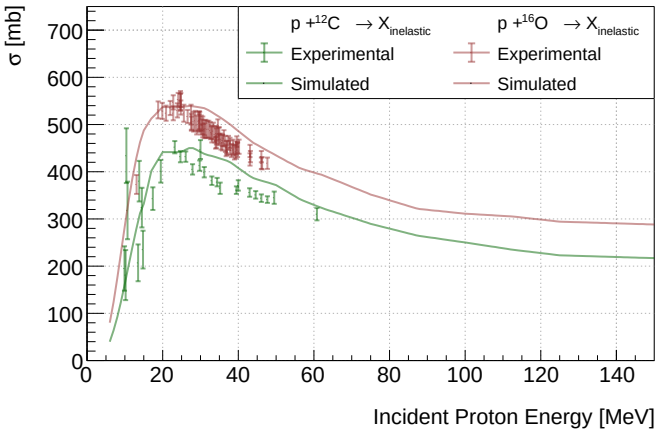

Figure 2.7. Proton-carbon (green) and proton-oxygen (red) inelastic cross sections values as function of the proton kinetic energy. Experimental data obtained from Bauhoff [1986] and *Monte Carlo* simulations (GEANT4 v11.1.2, Agostinelli et al. [2003]).

2.1.3 Induced Secondary Radiation

In particle therapy, induced secondary radiation represents an important tool for treatment monitoring, particularly in the context of range monitoring. Several types of induced secondary radiation act as probes, providing important information about the interactions between the particle beam and the tissue. Nuclear fragmentation results in the production of secondary particles, while prompt gamma-ray radiation is emitted immediately after nuclear reactions and provides real-time data. Equally important is the delayed radiation produced by the decay of unstable nuclei. Less common, but recently important due to the use of new high-Z materials, is Particle-Induced *X-ray* Emission (PIXE). The following sections describe these emissions in more detail.

Nuclear Fragmentation

The pre-equilibrium and evaporation stages of an inelastic nuclear reaction govern nuclear fragmentation. In general, it results in the loss of the primary ion flux in the beam, the transmutation of the recoil target and (or) the primary nucleus, and leads to isotropic emission of neutrons and charged particles such as protons and light ions (fragments). The resulting nucleus may be further excited and subsequently emit additional secondary radiation, such as gamma-rays. In proton therapy, the flux decreases by approximately $1\,\%$ per cm (Newhauser and Zhang [2015]) and the emitted target fragments locally contribute to the deposited energy and the lateral spread of the beam. On the other hand, heavier ions comprising multiple nucleons can undergo additional nuclear fragmentation. Projectile fragments are produced with a *Lorentz* boost in the beam direction, deviating only slightly in angle. Consequently, the lighter charged fragments result in energy deposition behind the *Bragg* peak. This effect can be observed in Figure 2.2, which shows a characteristic dose-tail in the depth-deposited energy profile of the carbon beam. It is, therefore, fundamental to consider the characteristic dose-tail when considering treatment directions aiming at OARs.

Prompt Gamma-Rays

A class of secondary radiation induced by the nuclear interaction of a particle beam with organic tissue involves prompt gamma-rays emitted during the de-excitation phase of inelastic nuclear interactions. In the context of particle therapy, for lighter isotopes, such as ^4He, the relaxation of the nucleus occurs by the emission of lighter nuclei. In contrast, the nuclear energy level gaps in heavier isotopes are narrower, with possible nuclear transitions ranging from a few keVs to $10\,\mathrm{MeV}$. In this case, discrete and continuum gamma-ray emission is promoted. As an example, Figure 2.8 shows part of the nuclear energy level structure of a common element found in particle therapy, ^{16}O.

In general, other elements have a similar structure and de-excitation process, where the ground state is reached either with a single transition or with a series of sequential transitions through intermediate energy levels. Each transition may involve gamma-rays emission with energies specific to the differences between these levels, resulting in a characteristic gamma-ray spectrum for every isotope. Additionally, nuclear transitions occur almost instantaneously, with characteristic times on the nanosecond scale. When de-excitation occurs in the projectile rather than the target, *Doppler* broadening occurs due to the varying velocities of primary particles, which can complicate the analysis of discrete spectral lines. Due to its high cross-section values, dependence on deposited energy, and high energies that allow photons to escape the body with negligible attenuation, prompt gamma-ray emission is one of the most extensively studied types of secondary radiation for beam monitoring.

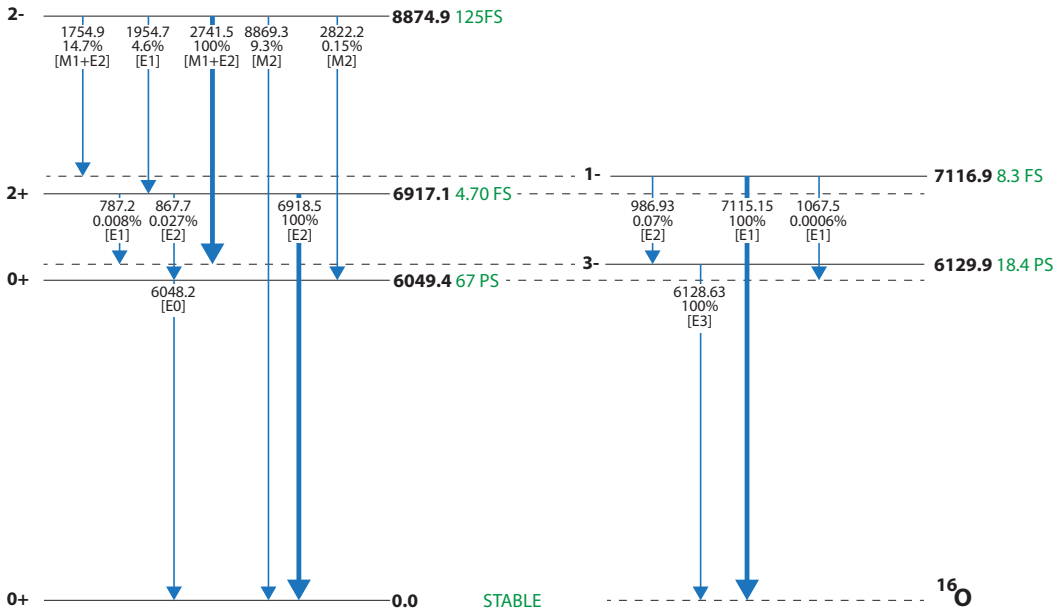

Figure 2.8. Nuclear energy levels (solid, black) for ^{16}O. Energy level states up to 9 MeV and their correspondent total angular momentum are shown. The principal de-excitation channels (blue arrows) and their characteristic decay times are also reported. Adapted from NuDat [2024].

Delayed Radiation

In particle therapy, nuclear reactions can produce unstable isotopes that, contrary to prompt gamma-rays, emit radiation over a relatively long period; these are known as delayed emissions. The most common and valuable emission for beam monitoring is the positron (β^+) resulting from the production of neutron-deficient nuclei isotopes during beam irradiation. Example of such isotopes in living tissue, are ^{11}C, ^{13}N and ^{15}O with half-lives ($T_{1/2}$) of about 20, 10, and 2 min , respectively. Physically similar to prompt gamma-rays, and depending on the used charged ion, β^+ activation results either from target fragmentation only or from the formation of both target and projectile positron-emitting fragments (Parodi et al. [2001]). Subsequent interactions of β^+ through inelastic *Coulomb* collisions with the atomic electrons lead to the most likely annihilation at rest with the emission of two 511 keV photons, emitted in opposite directions (at an angle of 180 °) due to the conversation laws of energy-momentum. Alongside prompt gamma-ray, positron emission is one of the most important and widely researched features for beam monitoring.

Particle Induced *X-Ray* Emission

As the charged ion moves through the material, atomic ionization mediated by *Coulomb* interactions leaves vacancies in the inner and outer shells of the atoms that pass by, resulting in a unstable electron atomic distribution. In a very short period of time (order of fem-

tosecond), the electronic structure is reorganized by the drop down of electrons of higher shells into the former vacancies. In the process, a competition of secondary radiation is emitted, including characteristic *X-rays*, *Auger* electrons and *Super Coster-Kronig* (SCK) electrons. The latter occurs only for transitions involving the L shell and higher. For low atomic number targets, and assuming K transitions, most transitions are non-radiative. As Z increases, the probability of *X-ray* emission increases and becomes predominant. In addition, the binding energy of inner shell electrons increases, and so does the photon energy. This is particularly important when using high Z materials in particle therapy. The relative high-energetic *X-ray* photons are no longer fully attenuated by the body, and can potentially be used as a new source of information for beam monitoring.

2.2 Therapeutic Concepts

In the following sub-sections, key therapeutic concepts pertinent to particle therapy and to this study are briefly introduced.

2.2.1 Absorbed Dose

In radiation therapy and dosimetry, an essential physical quantity is the absorbed dose, D. This quantity is prescribed by physicians for tumor treatment, by radiation protection officers as exposure limits to workers, and referenced by researchers while performing irradiation studies in radiotherapy. The International Commission on Radiation Units (ICRU, Thomas [2012]) defines absorbed dose as the mean energy, dE, per unit mass, dm, imparted to an absorber, $D = \frac{dE}{dm}$ with units of $\mathrm{Gy} = \mathrm{J\,kg^{-1}}$. The absorbed dose quantity is applies to both direct and indirect ionization radiations. The rate at which the absorbed dose is delivered over time, t, is defined by $\dot{D} = D/dt$.

2.2.2 Linear Energy Transference

As mentioned before, the chemical and biological effects of the absorbed dose depend on its LET, therefore knowing the LET of a given radiation beam is important when prescribing doses in radiotherapy. The LET is measured in units of $\mathrm{keV/\mu m}$, with low LET (sparsely ionizing) radiation classified as bellow $10\,\mathrm{keV/\mu m}$ when compared with high-LET (densely ionizing) radiation (Podgoršak et al. [2006]). Photons ($2\,\mathrm{keV/\mu m}$ for *X-rays* produced by a $250\,\mathrm{kVp}$ source) are considered low LET radiation, while neutrons, low energetic electrons and heavier charged particles, such as protons ($17\,\mathrm{keV/\mu m}$ at $2\,\mathrm{MeV}$) and heavier ions ($100\,\mathrm{keV/\mu m}$ to $2000\,\mathrm{keV/\mu m}$), are usually high LET radiation (Podgoršak et al. [2006]). It

is important to know that, in most cases, the LET value depends on the energy of the particle and is inversely related to its energy.

2.2.3 Relative Biological Effectiveness

The relative biological effectiveness (RBE) is used to quantify this individual chemical and biological response of different ionizing radiation and is defined as the ratio of reference dose (usually *X-ray* photons from a $250\,\mathrm{kVp}$ source or gamma-rays from a Co_{60} source) and tested dose that produces the same biological effect. The RBE varies not only with the type of radiation but also with type of tissue, dose, dose rate, and fractionation. In general, the RBE increases with LET to reach a maximum (> 3 for heavier charged particles) before decreasing as LET continues to increase.

2.2.4 Tumor Control vs. Tissue Complications

The objective of radiotherapy is to give dose to a tumor while minimizing exposure to healthy tissues. Therefore, it is important to analyze two distinct features when planning a treatment: tumor control probability (TCP) and normal tissue complication probability (NTCP). The former measures the likelihood that a specific radiation dose will provide tumor control or eradication, while the latter measures the likelihood of adverse side effects on healthy tissue for a specific dose.

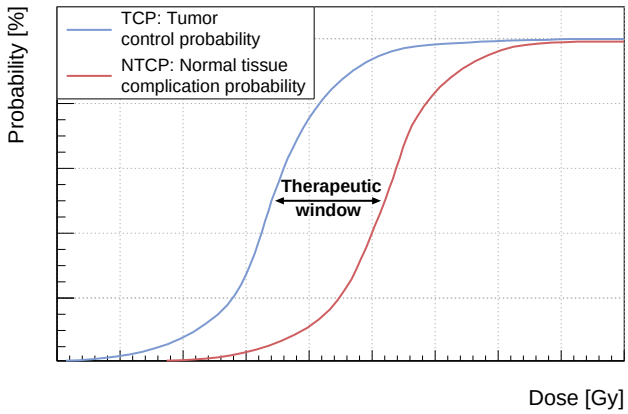

Figure 2.9. Therapeutic window defined by the tumor control probability (solid, blue) and the normal tissue complication probability (solid, red).

Figure 2.9 depicts the TCP and NTCP curves as a function of the dose. These curves define the therapeutic window for radiation therapy, representing the range of radiation doses that achieve effective TCP while minimizing NTCP. Increasing the radiation dose improves

TCP but also raises NTCP, requiring careful optimization of treatment plans to maximize outcomes while reducing side effects.

2.3 Particle Beam Delivery

The production of moderately relativistic charged ions has a long history. Lawrence and Livingston [1932] first developed the cyclotron to accelerate protons, and later advancements led to the development of synchrotrons, allowing higher energies and delivery of protons and heavier ions (McMillan [1945], Veksler [1957]). Today, clinical facilities are based on either of these technologies or a combination of both (synchrocyclotron). As reported by the Particle Therapy Co-Operative Group (Particle Therapy Co-Operative Group), in 2024, there are 67 cyclotron facilities, 43 synchrotron facilities, and 18 synchrocyclotron facilities, with many more under construction. In this section, the concepts of particle beam delivery will be briefly introduced. Additionally, the Heidelberg Ion Therapy Center (HIT) and the Marburg Ion Therapy Center (MIT) are also described due to their relevance to this study.

2.3.1 Ion Sources

The beam delivery process starts with the distinct production methods for protons and heavier ions. Protons can be produced by several methods (Muramatsu and Kitagawa [2012]), while heavier ions are created exclusively by using an electron cyclotron resonance (ECR) ion source. A duoplasmatron ion source is often sufficient for producing protons. The source produces the ions by applying an arc discharge of hydrogen gas, ionizing the hydrogen atoms and leaving behind individual electrons and singly charged protons (^1H). ECR can also be used for protons but is, generally, the only method available to produce heavier ions at particle therapy facilities. The ions are produced as a result of collisions between accelerated electrons and a gas consisting of molecules with the desired ion (e.g., CO_2 for carbons). This process dissociates the molecules and strips away electrons, creating positive charged ions. Both protons and carbons are then extracted from the created plasma by strong electric fields. If not fully stripped of their electrons, as is usually the case, the ions pass by a further process where the remaining electrons are removed by a stripping foil.

2.3.2 Accelerators

To effectively treat deep-seated tumors, ions must be accelerated to achieve sufficient kinetic energy. The most common accelerators, cyclotrons and synchrotrons, use electric fields to impart kinetic energy to charged ions while relying on magnetic fields to control and direct their motion.

In a cyclotron, particles are accelerated by an electric field that oscillates at a certain radio frequency (RF). This acceleration occurs within a uniform magnetic field created by two D-shaped dipole magnets with their straight sides facing each other. The perpendicular magnetic field causes the particles to undergo cyclotron motion. The particles are accelerated until they reach the maximum energy (ranging from $200\,\mathrm{MeV}$ to $250\,\mathrm{MeV}$, Braccini [2017]), limited by the cyclotron's radius and strength of the magnetic field. Variable-thickness absorbers, known as energy degrades, are used to adjust the final beam energy to desired levels. The quasi-continuous particle beam is delivered collimated, with short bunch widths of $T_{bw} < 2\,\mathrm{ns}$ in micro-periods of $T\mu = 10\,\mathrm{ns}$ (Krimmer et al. [2018]).

In contrast, synchrotrons rely on a different mechanism for particle acceleration. They consist of a circular ring in which electromagnetic resonant cavities accelerate particles to high energies. Unlike in cyclotrons, particles are kept at a constant radius by strong variable magnetic fields. The beam is typically delivered in macro-periods of $T_M = 10\,\mathrm{s}$, corresponding to the injection, acceleration, and extraction cycle of the accelerator. The duty cycle extraction of the particles is done over several seconds (varying from hundreds of ms to $8\,\mathrm{s}$, depending on the facility and mode of operation) and is referred to as a spill. Within a spill, particles are extracted with T_{bw} ranging from 15 to $75\,\mathrm{ns}$ and $T\mu$ ranging from 100 to $350\,\mathrm{ns}$, depending on the energy and type of the particle (Magalhaes Martins et al. [2020b]).

Particle therapy monitoring techniques depend on the beam micro- and macro-periods for effectively detecting induced secondary radiation. Therefore, its use and limits vary depending on the type of accelerator considered. While the shorted T_{bw} in cyclotrons allows the use of the RF signal without any additional detector to distinguish between prompt radiation and delayed radiation (Testa et al. [2010]), the also shorted $T\mu$ complicates their independent detection. Proton bunch drifts against the RF signal have been observed (Petzoldt et al. [2016]), complicating this process even further and requiring re-synchronization. In contrast, synchrotrons have a longer T_{bw}, and the RF signal is not sufficient for defining a useful time window for the independent detection of prompt radiation. Here, an additional detector to track the beam delivery with sub-nanosecond resolution and capable of handling high intensities is needed. A positive aspect is the longer T_μ and T_M, improving the separation of background signals and enabling more efficient data processing, especially during the spill pause (Dal Bello [2020]). In the case of particle imaging, the ion beam macro-structure sets the minimum constraints to complete a full particle imaging (Volz [2021]).

Towards Ultra High Dose Rates

Recently, a novel approach called FLASH radiotherapy has been shaping the future technology of accelerators. The modality uses ultra-high beam intensities (UHDR), depositing a significant amount of dose in a short period of time. The rationale, validated experimen-

tally by different groups (Atkinson et al. [2023]), is that using these UHDR ($> 40\,\mathrm{Gy/s}$), which are significantly higher than those used in conventional radiotherapy ($< 0.03\,\mathrm{Gy/s}$), reduces the side effects on healthy tissue (shifting the NTCP curve to the right in Figure 2.9), while maintaining the TCP, thereby increasing the therapeutic window (Limoli and Vozenin [2023]). FLASH doses are relatively easy to achieve with photons and electrons. However, current particle facilities are not prepared to deliver ultra-high intensity beams at the levels required. Due to the high beam currents available in some existing commercial devices, cyclotrons can more readily be adapted for FLASH irradiation. In contrast, synchrotrons require sophisticated beam techniques to achieve FLASH dose rates. Nevertheless, new accelerators are emerging to support this modality. These include laser-driven proton accelerators, for which further research is required before they can be applied in the clinic (Kroll et al. [2022]). With regard to particle therapy monitoring, this technique presents an additional challenge, as the high intensities and new macro- and micro-structures impose additional limits.

2.3.3 Techniques for Beam Shaping and Delivery

The final step of beam delivering is the modulation of the energy and spatial distribution of the beam. The energy modulation objective is to spread out the *Bragg Peak* (SOBP) width over a usable area. The modulation is achieved by using a range modulator wheel (passive scattering) of by varying the beam energy (pencil beam scanning).

Passive beam systems start with a narrow particle beam of width, $\sigma = 1\,\mathrm{cm}$ (Bortfeld et al. [2005]). Subsequently, the beam is broadened into the desired field size through the use of scatter foils. A rotating range modulator wheel is then used to achieve optimal tumor coverage (or distal conformation) with a SOBP. The final beam shape is achieved using milled apertures and compensators. The apertures are used to define the lateral boundaries of the treatment field, ensuring that the radiation conforms to the tumor's outline. At the same time, the compensator shapes the distal edge of the dose distribution.

In contrast, active beam delivery methods, such as the raster scanning method developed at *Gesellschaft für Schwerionenforschung* (GSI, Haberer et al. [1993]), represent a more advanced, efficient and precise approach. In pencil beam scanning, the beam is directed across the transverse plane, perpendicular to the beam axis, using dipole magnets, while the particle range is controlled by varying the beam energy. This enables a three-dimensional dose conformity. As an alternative to the raster scanning method, the scanning process can occur as discrete spots or in continuous motion. Pencil beam scanning offers superior dose conformity to the target, reduces unwanted beam contamination (e.g., neutron production), and minimizes the need for extensive hardware. Treatment plans based on active beams use

multiple energy layers, each with a specific distribution of spots to match the prescribed dose to the target. These plans are typically calculated using sophisticated algorithms based on *Monte Carlo* simulations (Knopf and Lomax [2013]), achieving greater accuracy, albeit at a higher computation cost. Spot separations generally range from 2 mm to 10 mm (Ur Rehman et al. [2022]), with beam delivery times governed by magnetic adjustments occurring within milliseconds. The beam position and energy are closely monitored during delivery using multi-wire proportional chambers and ionization chambers to ensure precise targeting.

2.3.4 Heidelberg and Marburg Ion Therapy Centers

The experimental measurements for this study were carried out at Heidelberg Ion Therapy Center (HIT) and Marburg Ion Therapy Center (MIT), two leading particle therapy facilities in Europe. HIT, operational since 2009, was the first European center to use both protons and carbon ions for treatment, treating over 8,000 patients to date. The center layout is shown in Figure 2.10a. It is equipped with four beam stations: two with a fixed horizontal beam (H1 and H2 rooms), one with a gantry and other one used for quality assurance (Q-A room), development and research activities. Its state-of-the-art accelerator system comprises ECR ion sources, a linear accelerator (LINAC), and a synchrotron. The facility provides a wide range of beam parameters for protons and ions such as ^4He, ^{12}C and ^{16}O. Proton and carbons energies up to $250\,\mathrm{MeV/u}$ and $430\,\mathrm{MeV/u}$, respectively, allowing penetration depths of up to 35 cm in patients. The spill macrostructure comprehends a $T_M \approx 10\,\mathrm{s}$ with a duty cycle of 55% (Magalhaes Martins et al. [2020b]). In 2021, HIT achieved a milestone by treating the first patient with helium ion therapy using pencil beam scanning, a world-first (Jäkel et al. [2022]).

Similarly, MIT shares much of HIT's technology, including the use of a raster scanning method developed at GSI and a similar accelerator chain, as shown in Figure 2.10b. It features four treatment rooms: three with horizontal beams (H1, H2 and H3 rooms) and one with a semi-vertical ($45°$) medical beam outlet (Scheeler et al. [2016]). While delivering protons and carbon ions with characteristics comparable to HIT, its beam delivery system differs slightly, with a longer extraction time of 80%. Additionally, MIT is actively pursuing the development of FLASH irradiation techniques for research purposes (Zink et al. [2024]). Both centers achieve UHDR through fast extraction, using kicker magnets to deflect the circulating beam in a single turn, typically within a few milliseconds (Scheeler et al. [2016]).

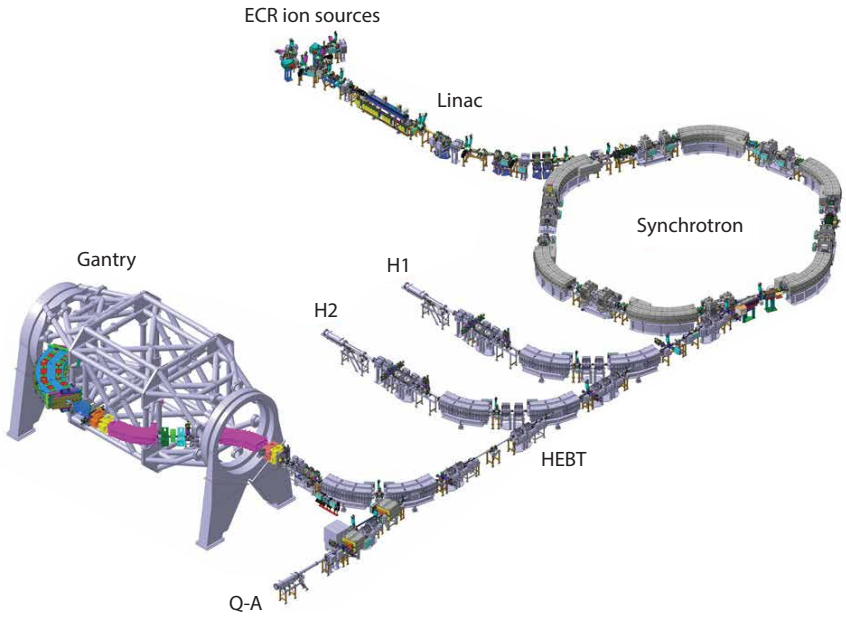

(a) Heidelberg Ion Therapy Center

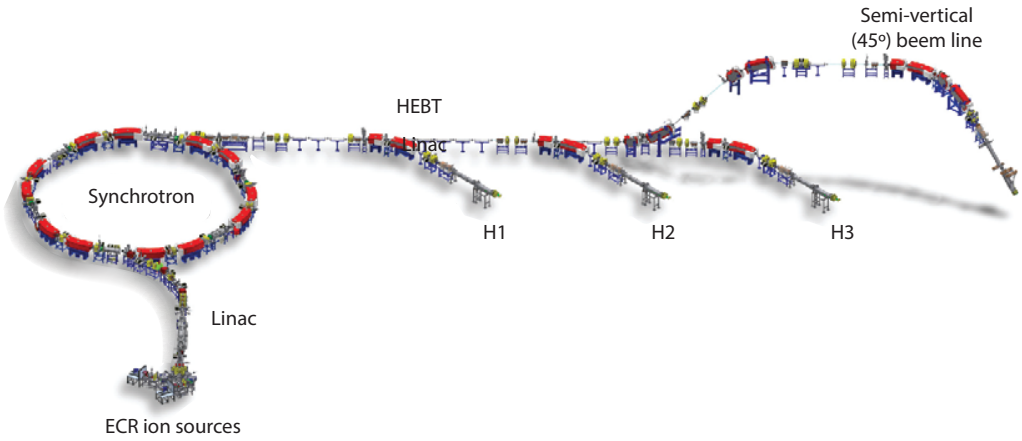

(b) Marburg Ion Therapy Center

Figure 2.10. An overview of (a) Heidelberg Ion Therapy Center and (b) Marburg Ion Therapy accelerator. The ECT ion sources feed the LINAC, where the ions undergo a first stage acceleration. This is followed by further acceleration in the synchrotron. Next, the beam is distrusted by the high-energy beam transport line (HEBT) to one of several destinations: the horizontal treatment rooms (H1, H2, H3), the gantry, the semi-vertical beamline, or the quality assurance (Q-A) room. Adapted from Ondreka and Weinrich [2008] and Scheeler et al. [2016].

2.4 In Vivo Particle Therapy Monitoring

The unique physical and radiobiological characteristics of particle therapy provide an opportunity for highly targeted and biologically effective radiotherapy, potentially improving clinical outcomes across various tumors types when compared to conventional radiotherapy. However, the steep dose gradient at the distal edge of *Bragg* peak makes particle therapy more sensitive to discrepancies between the delivered and prescribed treatment conditions. Patient mispositioning, organ motion, and anatomical changes between intra- and inter-fraction (e.g., tumor shrinkage, weight loss, or cavity filling) are examples of uncertainties that can lead to significant underdosing of the clinical target tumor (CTV) region and over-dosing of OAR, compromising TCP and NTCP. Furthermore, the treatment plans are also susceptible to errors, including the clinician's estimation of the tumor volume and the determination of stopping power values from computed tomography (CT). To account for such factors, safety margins are introduced in standard treatment plans, where a larger target volume (planning target volume, PTV) is defined as the area to be treated.

Figure 1.1 shows the averaged safety margins dimensions used in clinical practice. These margins typically vary from 2 to 3 % of the proton range, with an additional fixed margin ranging from 2 to 3 mm. For deep-seated tumors, these values are approximately 1 cm. Another constrain is that clinicians are reluctant to aim a beam at a tumor right in front of an organ-at-risk (see Figure 1.2), and particle treatments are delivered using sub-optimal beam angles in multi-field or patched-field plans. This avoid the placement of the distal-edge towards the OAR with the cost of a less conformal therapy. In this context, significant efforts have been made to address these limitations introduced by range uncertainties and to develop a system capable of *in vivo* particle therapy monitoring, ideally in real-time and under clinical conditions. The following sections outline the latest advancements in this field.

2.4.1 Particle Imaging

In particle therapy, *X-ray* CT images are commonly used to estimate stopping power values by measuring electron densities of the tissue. However, due to intrinsic differences in how photons and charged ions interact with matter, these estimations are a major source of range uncertainties. An ideal solution would be to directly measure the stopping power using charged ions. To achieve this, a transmission particle beam is necessary for patient imaging. The concept of proton CT was first proposed by Koehler [1968], but technological limitations at the time prevented its full exploration. Subsequent studies demonstrated that proton CT could offer improved contrast and dosimetric benefits, with potential dose reductions by a factor of 10 to 20 when compared to conventional CT images (Schneider and Pedroni [1995]). Despite its potential, proton CT has faced challenges with spatial res-

olution due to MCS of protons, although recent advancements have achieved resolutions of 1 mm, sufficient to meet clinical requirements, as outlined by Schulte et al. [2004]. Dedicated reconstruction algorithms have been developed to further mitigate the effects of MCS, enhancing image quality. In theory, heavier ions such as ^{4+}He scatter less than protons, potentially offering improved image quality. However, studies on helium CT have shown marginal improvements over proton CT (Piersimoni et al. [2018], Volz et al. [2021]). A more interesting approach involves the use of a mixed-beam technique, where a small proportion (10 %, corresponding to a 1 % dose increase to the patient) of ^{4+}He is added to a ^{12+}C ion beam. In this novel technique, both ions share the same kinetic energy, but ^{4+}He has a greater range, allowing its use for beam monitoring (Volz et al. [2020]). Ion imaging represents a promising solution as an indirect beam monitoring technique.

2.4.2 Positron Emission Tomography

The first method to be successfully applied as in-vivo range monitoring was the positron emission tomography (PET). This technique uses the annihilation photons from β^+ emitters, as detailed in section 2.1.3. The process occurs from the point of particle entrance until the nuclear reaction channel cross-section reaches zero at the *Coulomb* barrier. These cross-sections are generally within the range of 10 to 20 MeV/u, corresponding to a residual particle range of approximately a few mm in tissue. In cases where the process is induced only by target fragmentation (e.g., proton-induced), the general activity is, in first approximation, constant from the skin until the final range of the primaries. However, when including processes involving positron-emitting fragments of the projectile (induced by heavier charged ions than protons), the depth activation profile typically shows a pronounced maximum shortly before the end-of-range of the ions (Parodi et al. [2001]). Additionally, for projectiles heavier than protons, significantly lighter fragments create a tail of β^+ emitting target fragments extending beyond the *Bragg* peak. The resulting photons have a high probability of escaping the patient, and their coincident detection and activity distribution have the potential to retrieve the *Bragg* peak position during particle therapy treatments.

PET scans can be performed either shortly after treatment (in-beam or quasi-online, Bisogni et al. [2017], Ferrero et al. [2018]) or a few minutes post-treatment (offline, Handrack et al. [2017]). The in-beam approach allows the detection of processes induced by β^+ emitting species with shorter half-lives, whereas offline scanning is conducted in a nearby room and only isotopes with half-lives exceeding a few minutes contribute to the PET image. Consequently, offline PET accuracy is limited to a precision of a few millimeters due to low statistics caused by patient repositioning, scanning delays, and, most significantly, the biological washout of the isotopes (Handrack et al. [2017]). In contrast, in-beam PET

benefits from substantially higher β^+ activity, potentially achieving sub-millimeter precision (Cuccagna et al. [2024]). However, this precision is constrained by prompt and neutron radiation, making the implementation of real-time in-beam PET with cyclotrons particularly challenging. Its use is more suitable for synchrotron-based facilities, where off-spill times are free from prompt radiation (Ferrero et al. [2018]). In-spill acquisitions are still feasible using short-lived emitters (Sportelli et al. [2013]). Nevertheless, to achieve sufficient statistics, PET imaging typically requires scan times of several minutes, often extending post-treatment Ferrero et al. [2018]. This limits PET imaging to integral dose deposition, making spot-by-spot range monitoring difficult.

PET-based beam monitoring has already reached clinical implementation and is now undergoing clinical trials (Moglioni et al. [2022], Tashima et al. [2020]). Further research focuses on time-resolved measurements of the arrival time differences (time-of-flight, TOF) of photon pairs detected in coincidence Knopf and Lomax [2013]. TOF-PET's practical advantage is based on the improvement of the signal-to-noise ratio of reconstruction images rather than the spatial resolution, which reduces artifacts and alleviates issues related to limited-angle image reconstruction.

2.4.3 Prompt Gamma-Ray Imaging

[3]Systems based on prompt gamma-rays can be classified into two main categories: imaging systems with physical or electronic collimation and non-imaging systems. The determination of the beam range is achieved through the use of specific physical quantities, including energy, TOF of charged ions, and spatial distribution of emission. The depth profile of proton induced prompt gamma-rays is similar to target-emitting β^+ in PET but with a smaller gap to the distal edge of the *Bragg* peak. The translation of these features to an imaging technique was first proposed by Stichelbaut and Jongen [2003], who suggested determining the beam range by measuring the yield of prompt gamma-rays along the beam's depth-dose distribution. Following preliminary validation through experimental results, several research groups emerged worldwide to further validate this technique, later termed prompt gamma-ray imaging (PGI).

The most straightforward collimator geometry for PGI is the multilayered collimator system (Min et al. [2012]). The concept, known as the multi-slit camera and depicted in Figure 2.11a, is to obtain axial depth profiles of the prompt gamma-ray yield at $90°$ relative to the beam direction. A more sophisticated approach is the knife-edge slit camera depicted in Figure 2.11b (Smeets et al. [2012]). This design is based on the physical principle of

[3]Note: This section includes modified excerpts from the chapter "Imaging for Daily Range Monitoring of Treatment Beam," authored by Pryanichnikov, A.A., **Freitas, H.**, Parodi, K., and Volz, L., in the book "Introduction to Particle Therapy: An Educational Handbook" (Foka, Y., Vretenar, M., & Seco, J., eds.)

classical optics, which has been adapted for PGI. The concept can be applied using either passive (Richter et al. [2016]) or pencil beams (Xie et al. [2017]) and enables the detection of emitted prompt gamma-rays along the longitudinal axis with standard deviations of $2\,mm$.

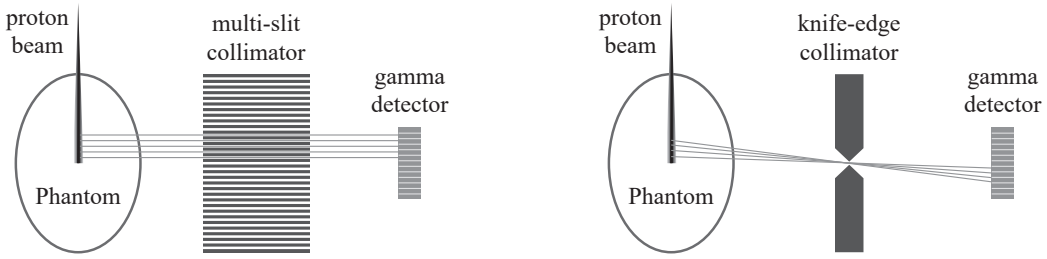

(a) Multi-slit camera schematic

(b) Knife-edge camera schematic

Figure 2.11. Schematics of two types of cameras: (a) multi-slit camera using simple collimation of prompt gamma rays to obtain their $1D$ spatial distribution, and (b) knife-edge camera, which combines collimation with optical principles to achieve the same result.

Previous PGI techniques rely on heavy collimators, which present a significant obstacle to their clinical feasibility. A promising alternative approach is the *Compton camera*, which is depicted in Figure 2.12. This technique uses an electronically collimated system comprising multiple position-sensitive detectors to obtain the spatial distribution of prompt gamma-rays. At least one scattered detector and one absorber are required, although multiple scattered planes are typically used. The physical principal of the technique is based on the *Compton* formula, $\cos\theta_\gamma = 1 - m_e c^2 \left(E_{\gamma'}^{-1} - E_\gamma^{-1}\right)$, where E_γ is the incident photon energy, $E_{\gamma'}$ the photon energy after the scatter with a angle θ_γ, $m_e c^2 = 511\,\text{keV}$ the mass rest energy of the electron. The total energy of the photon is obtained by summing the deposited energy in both the scatter and absorber plan. The prompt gamma-ray energy- and position-resolved detection from the multiple detectors restricts the direction of the incident photon in the so-called *Compton* cones. The origin of the photon can then be determined with the vertex superposition of a few cones. Reconstruction algorithms, generally based on iterative methods, allow for the generation of $2D$ or even $3D$ images of the charged ions path. Despite its complexity associated with the high detector load, and the high percentage of random noise (or false coincidences), Draeger et al. [2018] reported $3D$ images possible of detecting range shifts of 2 mm for the delivery of a 2 Gy spot beam.

A further uncollimated technique is the concept proposed by Golnik et al. [2014], Prompt Gamma-Ray Timing (PGT), which uses the time interval between the particle exit at the nozzle (including the process of transport through the tissue) and the detection of a prompt gamma-ray, for beam monitoring. The transit time, $t_p\,(x_p)$, between the initial position, x_0, and the range of the particle, $x_(p)$, is indirectly measured by the temporal prompt gamma-ray

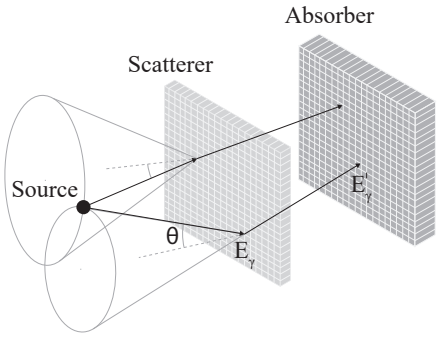

Figure 2.12. Schematic illustrating the principle of a *Compton* camera, in which prompt gamma-rays scatter in the first detector and are absorbed in the second. The design enables reconstruction of the spatial distribution of emitted photons by determining their incoming direction based on the physical principle of *Compton* scattering.

emission, thus determining the particle TOF, as described by,

$$t_p(x_p) = \int_{x_0}^{x_p} v(E(x))^{-1}\, dx = \int_{E_{x_p}}^{E_0} [v(E)\rho(x_p(E))S_{tot}(E)]^{-1}\, dE \tag{2.9}$$

where, v the velocity of the ion, E its energy and S the associated mass stopping power for a material of density ρ. PGT is particularly suitable for treatments using cyclotron accelerators, as they can provide a time reference from the bunch RF. The final range of the particle is derived mathematically through CSDA. The technique achieves maximum efficiency at photon energies ranging from 3 MeV to 7 MeV, which allows for neutron background rejection. Depending on the statistics, Hueso-González et al. [2015] demonstrated the detections of range shifts ranging from 5 mm to 2 mm. As previously mentioned, a common issue in cyclotrons is the drift of the accelerator bunch time. To address this, Petzoldt et al. [2016] proposed using an external particle bunch tracker to compensate for the drift, ensuring more precise synchronization with the accelerator's reference timing and its use in synchrotron facilities. The principle relied on the detection of scattered ions in a hydrogen-containing foil placed at the nozzle exit. Later, more sophisticated bunch monitors based on scintillating fibers were used. These advancements make it possible to perform precise TOF measurements and background correction of uncorrelated events. A similar technique to PGT, is the Prompt Gamma-Ray Peak Integration (PGPI) proposed by Krimmer et al. [2017]. PGPI exploits the integral in prompt gamma-ray TOF distributions, along with count rate ratios, to determine the particle beam range. It potentially achieves a range accuracy of 3 mm with a standard number of particles per spot (10^8).

First proposed by Verburg et al. [2012], energy-resolved measurements offer an alternative to time-resolved methods for range monitoring. This approach, coined prompt gamma-ray spectroscopy (PGS), uses the energy spectrum of prompt gamma-ray emissions to pro-

vide absolute range monitoring of a particle beam. Specifically, it uses the intensity ratio of the characteristic lines of the gamma-ray spectrum, which are monotonic and unequivocally invariant, to achieve beam monitoring. Furthermore, the spectroscopy nature of PGS makes it possible to obtain information about the composition of the targets. Thus, one can measure elemental concentration changes (e.g., levels of tumor hypoxia and tracking of the calcification in brain metastases) and tailor the treatments accordingly (Magalhaes Martins et al. [2020a]). PGS can be used independently or as an adjunct to other techniques based on secondary prompt gamma-ray emission. The combination of PGS and time-resolved measurements has led to significant improvements in determination of the beam range. Dal Bello et al. [2020] demonstrated the versatility of the technique for heavier charged particles, such as ^{12}C, where features extracted from PGS spectra can be used for beam monitoring. Despite challenges such as the statistics per prompt gamma-ray line and target heterogeneities, PGS has a statistical precision of approximately 1 mm.

New techniques for prompt gamma-ray monitoring are still evolving, with a shift towards cost-effective options like coaxial detectors (Hueso-González and Bortfeld [2019]) and the use of nanoparticles to enhance prompt gamma-ray emission (Galanakou et al. [2022], Penninckx et al. [2021]). As it nears clinical integration, the focus is increasingly on dose measurements and reconstruction strategies (Foglia et al. [2024]), making it a tool for both range measurement and dose monitoring.

2.4.4 Emergent Techniques

Techniques such as magnetic resonance image (MRI) and ionoacoustic imaging are alternatives that can also be used as particle monitoring technique. Instead of secondary induced radiation, they use different physical features to achieve particle therapy monitoring.

MRI has previously been applied on the unconventional interpretation of standard $T1$-weighted images. The $T1$ weighted signal is dependent on tissue properties that undergo changes after the particle irradiation, indicating the dose distribution of a particle beam (Pham et al. [2022]). However, the signal becomes visible only as early as 10 days following radiation therapy and can, therefore, only be used retrospectively. In particle therapy monitoring, this technique has recently become a major area of research as a guided therapy technique. Its in-beam integration into particle therapy allows real-time tracking of tumor position and movement, enabling treatment plans to be better aligned with the target. The use of MRI in this modality leads to improved TCP with less toxic treatment margins and the potential for adaptive particle therapy. A major breakthrough was recently achieved by OncoRay [2024] (National Center for Radiation Research in Oncology), which inaugurated the world's first prototype of a whole-body MRI system for online imaging. This development

marks an important step forward in particle therapy monitoring techniques.

Ionoacoustic imaging is an innovative monitoring technique based on the principles of acoustic wave generation that combine the possibility of obtaining anatomical structure images, as in MRI, with the additional capability of range measurements (Kellnberger et al. [2016]). For each pulse of charged ions, local thermal expansion and contraction of the tissue occur due to heat generation where the dose is deposited. This process emits pressure waves whose amplitude is directly proportional to the dose. In turn, these waves propagate as ultrasound signals, which can be detected using ultrasound imaging devices. The ideal beam macrostructure for optimal conversion of energy into thermoacoustic is achieved when $T_\mu \leq 1\,\mu$s and high-intensity pulses are used, making synchrocyclotrons the most suitable accelerator to be used with this technique (Lehrack et al. [2017]). Alternatively, ionoacoustic imaging can be used in other accelerators through artificial modulation of the beam profile (Jones et al. [2015]). Under these conditions, in the plateau region of the depth-dose profile, the energy deposition is relatively uniform and extends over a larger volume, generating cylindrical waves that propagate outward from the beam axis. In contrast, at the *Bragg* peak, where the energy deposition is highly localized, the resulting wavefront is approximately spherical. This distinction enables the use of temporal and spatial properties of acoustic signals to determine the particle range with high precision. The former property is a dual of TOF in PET and PGI, and plays a critical role in achieving sub-millimeter edge detections. The first *in vivo* observation of ionoacoustic imaging was reported in 1995 during liver tumor treatment with a proton beam delivered by a pulsed synchrotron accelerator (Hayakawa et al. [1995]). Recent research has focused on pencil beam scanning, and efforts aim to optimize electronics and data processing, with promising applications for advanced delivery techniques like FLASH.

Chapter 3

Gadolinium in Medical Physics

Gadolinium-based contrast agents (GBCA) are widely used in MRI due to the paramagnetic properties of the Gd^{+3} ion. In this oxidation state, where Gd loses three electrons, its electron configuration becomes $[Xe]\,4f^7$ with seven unpaired electrons in the 4f sub-shell (Gao et al. [2015]). Following administration to a patient, the GDCA will be distributed between the blood and the extracellular spaces. Given that tumors possess a leaky blood vasculature, a compromised endothelium, or an underdeveloped lymphatic drainage system, molecular contrast agents can passively accumulate in tumors via their vascular permeability to macromolecules (Zhou and Lu [2013]). This results in a transient increase in permeability and retention. Free Gd^{+3} ions are toxic, therefore in medical applications, they are sealed inside a linear or macrocyclic ligand that is either non-ionic or ionic to prevent them from interacting with healthy tissue. In contrast to their linear counterparts, macrocyclic ligands form closed rings, thereby conferring greater stability. Ionic ligands are charged and more water-soluble, whereas non-ionic ligands are uncharged and generally cause fewer side effects. The Gd^{+3} ion in GBCAs interacts strongly with the main magnetic field, shortening tissue relaxation times ($T1$ and $T2$), which enhances the visibility of internal structures and abnormalities during imaging procedures (Mahmood et al. [2022]). Approximately 35% of MRI examinations involve the use of GBCAs (Fraum et al. [2017]).

Among the seven naturally occurring isotopes of Gd, ^{155}Gd (14.8% abundance) and ^{157}Gd (15.7%) have some of the most significant cross-section values for thermal neutron capture, at 6.074×10^4 and $2.537 \times 10^5\ barns$ (NuDat [2024]), respectively. Only the noble gas nuclide ^{135}Xe has a higher cross-section value. The process for a neutron capture of ^{157}Gd is depicted in Figure 3.1a. Following Gd neutron capture event, *Auger* (including SCK) electrons, internal conversion (IC) electrons, gamma-rays, and *X-rays* are released. On the one hand, *Auger* and IC electrons are exploited in NCT because of their very short ranges, causing highly localized damage directly to cells containing Gd, especially in the nucleus if Gd has accumulated there. This makes them effective in targeting cancer cells

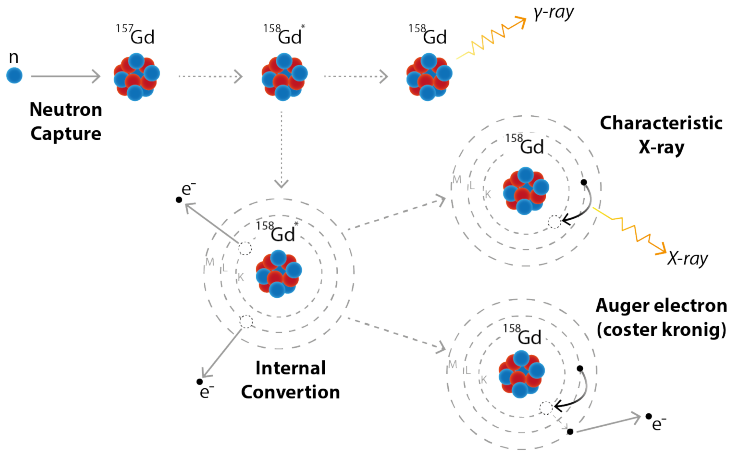

(a) Neutron capture

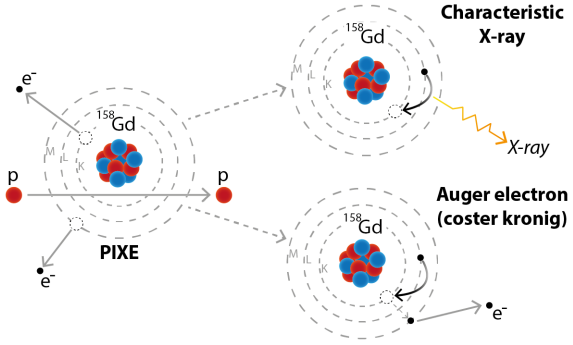

(b) Particle Induced *X-Ray* Emission

Figure 3.1. The diagrams depict two distinct physical processes that may occur when Gd is irradiated with particles. (a) Neutron capture process: a neutron is absorbed by a ^{157}Gd nucleus, resulting in an excited $^{158}Gd^*$ state. This state quickly decays to the stable ^{158}Gd, releasing energy in the form of gamma-rays, *X-rays*, and electrons through internal conversion and *Auger* processes. ($^{157}Gd + n = ^{158}Gd^* = ^{158}Gd + \gamma\text{-}rays + X\text{-}rays + e^-_{\text{internal conversion}} + e^-_{\text{auger}}$). (b) PIXE: A charged particle (proton) interacts with the electron shells of an atom, causing inner-shell ionization, followed by the emission of characteristics X-rays.

while minimizing effects on surrounding cells. On the other hand, photon emission, not as relevant in NCT, can be used to obtain information about the outgoing treatment, particularly for applications where the tumor region wants to be studied against healthy tissue. Table 3.1 describes the primary photon emissions from thermal neutron capture and their relative probability. Gräfe et al. [2010, 2011], first demonstrated the feasibility of using the photon emission to measure the distribution and uptake of the GBCAs during *in vivo* studies. Van Delinder et al. [2020] subsequently proposed its use for tumor localization in proton therapy.

Table 3.1. The most relevant isotopic emissions of ^{157}Gd and ^{155}Gd resulting from neutron capture by Gd, including *X-Ray* and prompt gamma-ray energies with their respective probabilities.

Isotope	Abundance [%]	Cross Section [b]	Emission Type	Energy [keV] / Probability [%]
^{157}Gd	15.7	2.537×10^5	X-ray (K_α)	43.0 / 18.2
			X-ray (K_β)	49.0 / 4.5
			Prompt gamma-ray	79.5 / 9.8
				181.9 / 18.1
				944.2 / 7.8
				6750 / 2.4
^{155}Gd	14.8	6.074×10^4	X-ray (K_α)	43.0 / 29.1
			X-ray (K_β)	49.0 / 7.1
			Prompt gamma-ray	88.9 / 15.3
				199.2 / 22.4

While previous understanding focused primarily on the thermal neutron capture by Gd, it maintains open its study for additional physical interactions such as PIXE and the removal of neutrons within the target region. The former is depicted in Figure 3.1b and results in the emission of supplementary *X-rays*. The latter, has the consequence of reducing the emission of 2.22 MeV gamma-rays resulting from hydrogen neutron capture. Moreover, the study of Gd as surrogate for dose measurements and its use with heavier charged ions than protons is still to be researched.

Chapter 4

Research Methodology

The chapter describes all the materials used in the experimental measurements and *Monte Carlo* simulations. It is followed by a brief overview of the acquisition system's main components, including example results obtained with the system and an outline of the data processing methods. Finally, the methodology of the research campaigns conducted to obtain the results for this study is presented.

4.1 Experimental Targets

4.1.1 Gadolinium Based Contrast Agent

A commercially available GBCA Dotarem® (gadoteric acid from Guerbet LLC) was used. This GBCA is valued for its low risk of nephrogenic systemic fibrosis and is commonly used in MRI of the brain, spine, and associated tissues (U.S. Food and Drug Administration [2017]). Dotarem® consists of a $0.5\,\mathrm{mmol\,mL^{-1}}$ aqueous solution of gadoterate meglumine, with a density of $1.18\,\mathrm{g\,cm^{-3}}$ at $20\,^{\circ}\mathrm{C}$. Its empirical formula is $C_{23}H_{42}O_{13}N_5Gd$, and it is classified as an ionic, macrocyclic molecule. Water was used as a control in the experimental measurements to serve as a baseline for comparison with the Gd results.

4.1.2 *PMMA* Blocks

Polymethyl-methacrylate (or PMMA) was used to access changes in spectra as a function of the tissue and to study the underlying physics behind the emission of Gd signal. In general, blocks with an area of $15 \times 15\,\mathrm{cm^2}$ and variable thickness were used. The block were aligned to obtain a different tissue equivalent thickness between the beam and the target. It should be also mentioned that the PMMA material was defined in *Monte Carlo* simulations based on the study that has been done by Hünemohr et al. [2013].

4.1.3 Sample Containers

Two different containers were used to hold the GBCA solutions and the reference (water): the original 15 mL glass vial provided by Guerbet LLC and 5 mL Eppendorf® tubes. In both cases, the room isocenter was consistently aligned with the center of the vials during experimental measurements.

4.2 Detectors and Acquisition Systems

The experimental measurements in this study followed a standard setup, as illustrated in Figure 4.1. The majority of experimental campaigns were performed using a PGS prototype system that had been previously developed at DKFZ in collaboration with HIT (Dal Bello [2020]). The PGS system is capable of measuring photon energy spectra with energies ranging from tens of keVs up to 10 MeV, including both gamma- and *X-ray* spectra. The prototype consists of a photon detector, an anti-coincident shield, a beam tracker, and associated electronics. Limited to a few experimental campaigns, a cadmium telluride (CdTe) detector was also employed, significantly improving the resolution photon energy spectra up to 200 keV. The following sections described the detector system and data analysis, focusing on the PGS prototype.

4.2.1 Prompt Gamma-Ray Prototype

Photon Detector

The photon detector for most of this work was based on an inorganic $CeBr_3$ hygroscopic scintillating crystals optically coupled to a Hamamatsu photomultiplier tube (PMT) R9240-100. It has a decay time, $\tau_{CeBr_3} = 20$ ns and a 5.1 g cm^{-3} density. The crystal is protected by Teflon™ and aluminum and has a cylindrical shape with a diameter 3.81 cm and length $l =$ 7.62 cm. When compared with other crystals used in PGI, such as $LaBr^3$, the $CeBr^3$ has similar characteristics but a lower background. The resolution of the detector as a function of the energy in keV is given by,

$$\frac{FWHM}{E} \times 100\,[\%] = c \sum_{i=0}^{3} \frac{A_i}{\left(\sqrt{E}\right)^i} \tag{4.1}$$

where the A_i coefficients are given in Roemer et al. [2015] and c is a correction factor due to crystal-dependent variations (e.g., shape, size, and other intrinsic properties). The crystals used in this study exhibited a resolution of approximately 20 % and 4 % at 32 keV and 662 keV, respectively.

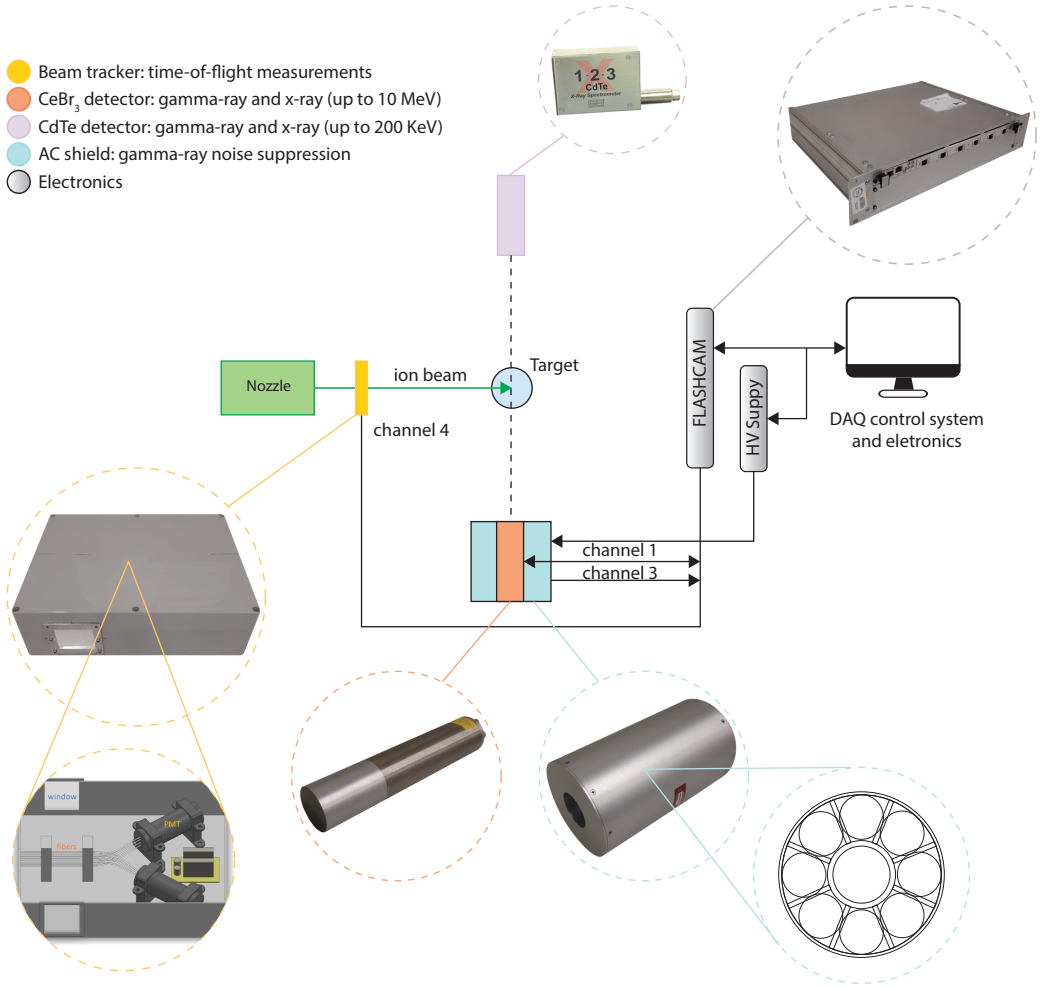

Figure 4.1. Schematic representation of the general experimental setup used in this study, including a beam tracker for time-of-flight measurements, an inorganic scintillator ($CeBr_3$), a semiconductor ($CdTe$) for photon measurements, and an anti-coincidence shield for noise suppression. The system can be used as a whole or with individual detectors for specific configurations.

Anti-Coincident Shield

The anti-coincidence (AC) detector surrounds the photon detector with eight optically separated, azimuthally symmetric segments of bismuth germanate (BGO) crystals. Each segment is optically coupled to an independent Hamamatsu R1924 PMT with a custom preamplification circuit. With a decay time of $\tau_{BGO} = 300\,\text{ns}$, the BGO crystals provide an energy- and time-resolved signal, serving as an AC shield in PGS measurements. This setup suppresses the background due to photons that are not fully absorbed, with partial energy escaping from the photon detector due to *Compton* scattering or single and double escape events arising from pair production and subsequent annihilation. The time resolution between the photon detector and the AC shield is $3.58\,\text{ns}$ FWHM (Dal Bello et al. [2019]).

Beam Tracker

To obtain prompt gamma-ray events correlated with the particle bunch delivered by the accelerator, a beam tracker detector was used. The prototype is equipped with an array of sixty scintillating fibers with a decay time of $\tau_{Beamtracker}$ and a sub-nanosecond time resolution of 0.8 ns (Magalhaes Martins et al. [2020b]). The fibers, designed $BCF-12$, and manufactured by Saint Gobain Crystals, have a diameter of 0.5 mm and are agglomerated in an alternating even-odd pattern. Each group of fibers is optically coupled to two Hamamatsu PMTs R657, resulting in a configuration of 30 fibers per PMT. The entire system is enclosed in a light-shielding plastic box with external windows for the particle beam, constructed from $10\,\mu$m-thick aluminized mylar. The beam tracker is typically placed between the beam nozzle and the target, enabling TOF measurements and background suppression of uncorrelated events (e.g., gamma-rays induced by hydrogen neutron capture).

FlashCam FADC Electronic Module

The PMTs readout was performed with a high-performance analog-to-digital (ADC) converter, namely the FlashCam FADC (Puehlhofer et al. [2015]). The system offers a 12-bit resolution in a multi-channel acquisition mode, with the capacity to digitize data at a rate of $250\,\mathrm{MS\,s^{-1}}$. The readout of all active channels is controlled by a single internal trigger, which can be pre-configured for each channel and initiated individually. The transmission of data is performed by a flexible ethernet-based interface with a data transfer rate of $2\,\mathrm{GByte\,s^{-1}}$. Each acquisition in this study was conducted on an event-by-event basis, with single traces ranging from $\Delta t = 200$ ns to $\Delta t = 400$ ns and sampling intervals of $\delta t = 4$ ns for the photon and AC-shield detector setup and $\delta t = 1$ ns for the beam tracker detector. The Flashcam FADC operates as a non-paralyzable system and follows the dead time correction model, where the true count rate N is approximated by

$$N \approx \frac{N_m}{(1 - N_m \frac{\tau}{\Delta t})}. \tag{4.2}$$

where, N_m represents the measured count rate, τ the dead time Knoll [2010]. A dead time measurement follows each trace, allowing the use of this model for dead time corrections. In this study, dead time was found to be negligible for beam intensities bellow $1 \times 10^9\,\mathrm{ions\,s^{-1}}$. For higher intensities, dead time corrections were applied to account for system limitations.

4.2.2 Cadmium Telluride

In order to gain a better understanding of the low energy levels observed in the photon energy spectra, a subset of experimental measurements were conducted using the Amptek® *X-123* Cadmium Telluride (CdTe) detector (Amptek [2017]), which includes the CdTe semiconductor detector, a preamplifier, and its own digital pulse processor. The CdTe detector as an active area of $25\,\text{mm}^2$ (180 times smaller than the photon detector) and a thickness of $1\,\text{mm}$, optimized for detecting *X-rays* and gamma-rays in the energy range of 5 to $150\,\text{keV}$. The energy resolution is lower than $1.5\,\text{keV}$ at $122\,\text{keV}$, improving significantly the spectra lines analysis within its intended energy range when compared with the $CeBr_3$ detector. It should be noted that, due to its limited availability, the system was used only in a subset of experimental measurements.

4.2.3 Data Analysis

The analysis algorithms were implemented in both C++ and Python. For Python, the libraries used included *numpy* (Harris et al. [2020]), *scipy* (Virtanen et al. [2020]), and *scikit-learn* (Pedregosa et al. [2011]). For C++, the ROOT framework (Brun and Rademakers [1997]) was utilized. The following sections describe the data steps used to obtain the photon energy spectra for each experiment, including background suppression using the anti-coincidence shield and time-resolved measurements. The raw data processing and background suppression were performed exclusively for the prompt gamma-ray detector system. The calibration and extraction of spectral features procedure was similarly applied in both, the PGS system and the $CdTe$ detector.

Raw Data Processing

The data processing starts by determining the features of each event acquire by the photon detector. This process implies a baseline restoration and single or multiple fits for each peak found in the event (with minimum peak separation of $20\,\text{ns}$) with Exponential modified *Gaussian* (EMG) model(s),

$$f(t,a,\mu,\sigma,\lambda) = \frac{a\lambda}{2} e^{\left[-(t-\mu)^2/2\sigma^2\right]} \left\{1 + erf\left[\frac{\mu+\lambda\sigma^2-t}{\sqrt{2}\pi}\right]\right\} \tag{4.3}$$

The EMG distribution is defined as the sum of independent normal and exponential random variables, where t is the time, a is the *Gaussian* amplitude, σ is the *Gaussian* sigma, μ is the position of the unmodified *Gaussian*, λ is the relaxation time parameter of exponent used to modify *Gaussian* and $erf = \frac{2}{\sqrt{\pi}} \int_0^z e^{-t^2}\, dt$ (Kalambet et al. [2011]). For each event and peak, the detected information on the event identification, a, μ, σ, λ, and a score based on

the adjusted coefficient of determination ($R^2_{adjusted}$ metric) were recorded. Not all detected peaks were considered valid. Some events exhibited poor shapes (e.g., due to overflows or pile-ups), while others were uncorrelated with prompt gamma-rays. Figure 4.2 shows the distribution of two key features, λ and $R^2_{adjusted}$, obtained from experimental measurements. Events were filtered based on these features to reduce noise in the data. For the $R^2_{adjusted}$, a threshold of $thr_{score} = \mu - 7.5\sigma$ was defined. For the λ, a *Gaussian* fit was applied to the peak associated with the no-noise events, and only events within a 5σ window were considered.

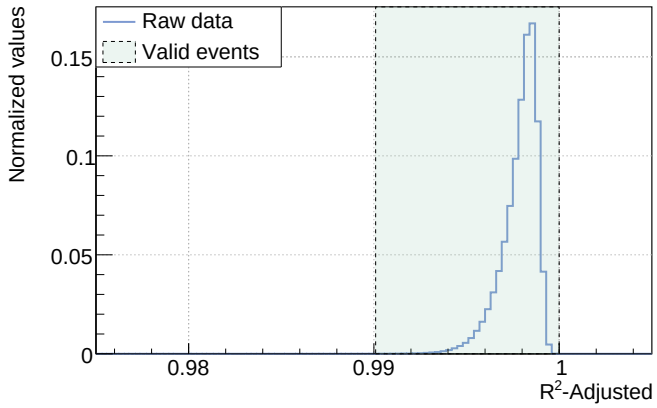

(a) $R^2_{adjusted}$ distribution

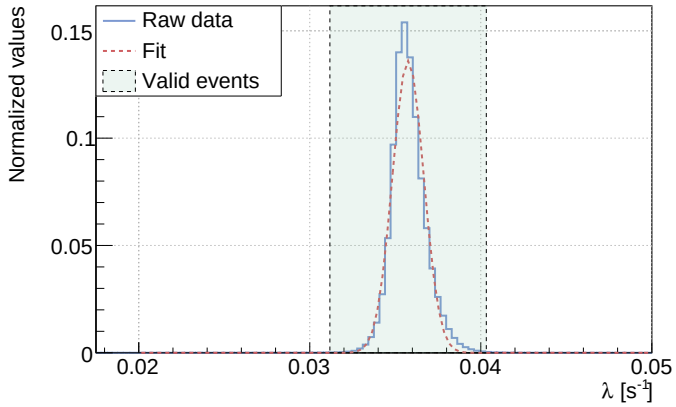

(b) λ distribution

Figure 4.2. Example distributions of (a) $R^2_{adjusted}$ and (b) λ obtained from a PGS measurement. Only events within the green area are selected to construct the photon energy spectra and perform the analysis.

Beam Macro-Structure

As mentioned in Section 2.3.2, a spill is defined as the duty cycle period during which the beam is active within its macro-structure. For each event, a timestamp is recorded by the photon detector and the beam tracker. By measuring the rate at which events are detected, it is possible to extract information about the duration of each spill and off-spill period, as well as the total number of spills. Additionally, this analysis enabled the distinction between events occurring within a spill and delayed events detected off-spill, with the photon energy spectra obtained from spill-associated events. Figure 4.3 depicts the results of a spill analysis as an example. Spill identification was accomplished by calculating the event rate through derivation and applying a threshold cut. The experimental values obtained were consistent with those reported by Haberer et al. [2004] ($5\,\mathrm{s}$) and Scheeler et al. [2016] ($8\,\mathrm{s}$) for the HIT and MIT institutes, respectively.

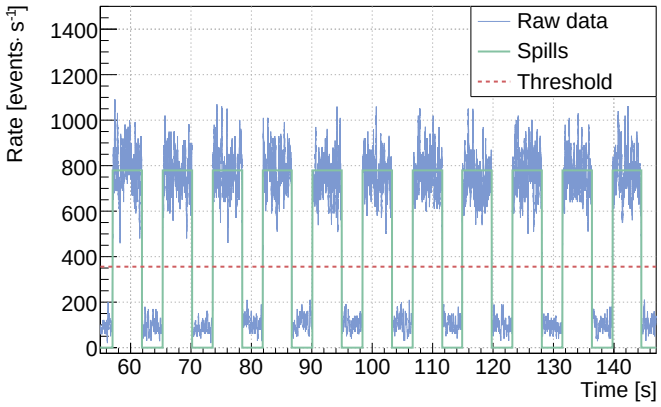

Figure 4.3. Extracted section of a PGS measurement at HIT, where is depicted the event rate (solid, blue) as function of time. A threshold is applied to generate a square wave, enabling the identification of spills or periods when the beam is active during the high phase of the pulse. For this specific measurement, the average duration of the active beam and inactive phase is $4.84 \pm 0.25\,\mathrm{s}$ and $3.44 \pm 0.73\,\mathrm{s}$, respectively.

Background Suppression

Background suppression due to neutrons and scattered and delayed radiation was achieved using the photon detector, the AC shield and the beam tracker. The application of the AC shield suppresses events where the photon energy is not fully absorbed by the detector. Only events registered by the photon detector in anti-coincidence with the following conditions were included in the spectra: events arriving at the AC shield after being detected by the photon detector, $\Delta t_{AC} = t^{event}_{CeBr_3} - t^{event}_{BGO} < 0$, and events with energies, $E_{BGO} > 225\,\mathrm{keV}$.

The beam tracker detector is essential for filtering uncorrelated events that would otherwise distort the prompt gamma-ray spectra. A typical TOF spectrum derived from the timestamp differences between the photon detector and the beam tracker is shown in Figure 4.4. The spectrum can be divided into three regions: the prompt radiation region, the scattered radiation region, and the time-independent radiation region. The prompt gamma-ray region consists of a $\Delta t_{TOF}^{PG} \approx 3\,\text{ns}$ to $10\,\text{ns}$ window and is followed outward by the scattered radiation (*Compton* events) region, which exceeds $\Delta t_{TOF}^{scattered} \approx 5\,\text{ns}$ or more beyond the prompt gamma-ray region, depending on the experimental setup and the charged ion used. The time-independent radiation region, consisting mostly of delayed radiation, occurs largely outside the previously defined regions.

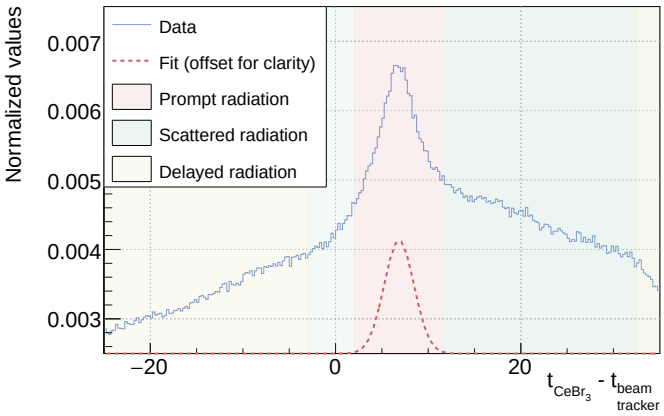

Figure 4.4. TOF spectrum divided into three sections: prompt radiation (red), scattered radiation (green) and delayed or time-independent radiation (yellow). Prompt radiation (dashed, red) events were fitted with a *Gaussian* distribution. In PGS, only events defined at $\mu \pm 3\sigma$ ($\Delta t_{TOF}^{PG} = 9.65\,\text{ns}$) are included in the photon energy spectra.

The application of these techniques and their effects on the photon energy spectra are shown in Figure 4.5. As a result of the AC technique, suppression of the *Compton* continuum is evident at low energies ($< 3\,\text{MeV}$), and the single and double escape peaks are effectively suppressed in the de-excitation lines of ^{12}C and ^{16}O. Moreover, hydrogen neutron capture and the β^+ annihilation line, a time-uncorrelated event, is also mitigated after the application of the TOF technique. These and previous filters improve the signal-to-noise ratio (SNR) and provide better resolved photo-peaks.

Energy Calibration

This study uses two calibration techniques to interpret the photon spectra in terms of energy rather than a non-informative quantity, such as ADC channels: offline and on-the-fly calibration. For the offline calibration, various radiation sources with well-known decay lines

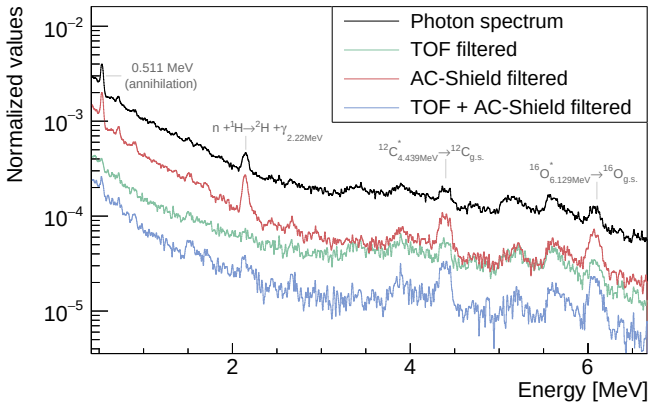

Figure 4.5. A calibrated photon spectra of a PGS measurement is presented, including: raw data, data filtered using the TOF technique, data filtered using the AC shield, and the combination of both methods. The annihilation peak (from β^+ decay, 0.511 MeV), hydrogen neutron capture peak (2.22 MeV), and the de-excitation lines of ^{12}C and ^{16}O are highlighted in gray.

were used. The following sources were used: ^{22}Na with a positron annihilation peak at 511 keV; ^{60}Co with decay lines at 1.173 MeV and 1.333 MeV; ^{133}Ba with selected decay lines at 32 keV, 81 keV and 356 keV; ^{137}Cs with characteristic *X-ray* and gamma-ray peaks at 32 keV and 662 keV, respectively; and ^{241}Am with the 60 keV peak specifically used. This initial calibration is subject to several sources of error, such as energy shifts caused by variations in the particle beam intensity, discrepancies in source-detector orientation, and intrinsic non-linearities of the photon detector. To mitigate these issues, an online calibration is performed using the known positions of high-energy spectral lines produced during charged ions' interactions with the medium. This approach allows for fine-tuning of the calibration process. The AC detector was calibrated exclusively using the offline method.

Extraction of Spectral Features

The photon spectra in this study typically consist of characteristic energy lines superimposed on a continuum background, which primarily results from *Compton* scattering interactions on the target and detectors. The background in itself can complicate the analysis of spectral features. Therefore, after obtaining the photon spectra, a baseline restoration based on the sensitive non-linear iterative peak (SNIP) algorithm ([Ryan et al., 1988]) was applied. Then, peaks of interest were identified and analyzed. These peaks were fitted with single or multiple *Gaussian* or *Lorentzian* functions in order to extract parameters such as mean energy, amplitude, and area.

4.3 Research Campaigns

4.3.1 Prompt Gamma-Ray Benchmarking

[1]Reflecting the crucial role of *Monte Carlo* simulations in the progress of beam monitoring techniques, this study starts by developing models for `GEANT4 v11.1.2` (Agostinelli et al. [2003], Allison et al. [2006, 2016]), `FLUKA v4-4.1` (Böhlen et al. [2014], Ferrari et al. [2005]) and `MCNP6 v2` (Werner et al. [2018]). A comparative analysis of these models was conducted with experimental results obtained at HIT, aiming to improve the accuracy and effectiveness of PGS in clinical settings.

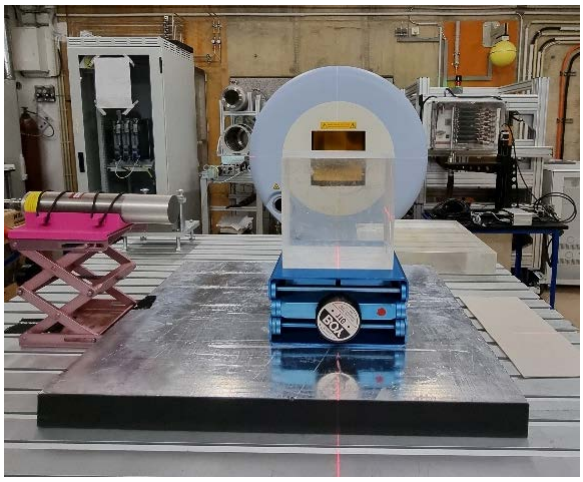

Figure 4.6. Experimental set-up. The detector is on the left, the PMMA is in the middle, and the exit point of the proton beam is in the background.

Figure 4.6 shows the general experimental setup used for the experimental measurements. PGS spectra measurements were obtained by shooting a proton beam into a *PMMA target*, which was placed 100.0 ± 0.5 cm away from the nozzle. In total, three blocks of size $15 \times 15 \times 5\,\text{cm}^3$ were used. The blocks were aligned to obtain a tissue equivalent block thickness of 15 cm. The PG detector was located 25.0 ± 0.5 cm away from the proton beam isocenter and perpendicular to the beam. A total of 5 proton irradiations was conducted with similar durations (~ 150 s) but different beam characteristics. Table 4.1 contains a summary of the beam information. The range of particles was determined using the calculated CSDA ranges at different energy values, with the assistance of NIST (M.J.Berger et al. [2017]) data. To replicate the experimental data, different *Monte Carlo* codes were used. Next, follows the description of the physics lists and methods used in each toolkit.

[1]Note: This section includes modified excerpts from the submitted work: **Freitas, H.**, Nobakht, E., Grüner, F., & Seco, J. (2024). A Comparative Analysis of GEANT4, MCNP6, and FLUKA on Proton-Induced Gamma-Ray Simulation.

Table 4.1. Run number, initial proton kinetic energy, beam lateral FWHM and the corresponding R_{CSDA} range used in Prompt Gamma-ray Benchmarking campaign.

Run	Energy [MeV]	FWHM [cm]	R_{CSDA} [cm]
1	89.91	1.75	5.514
2	99.74	1.58	6.633
3	110.24	1.44	7.923
4	120.05	1.34	9.212
5	129.52	1.25	10.53

`MCNP6`

Initially, only the proton data libraries were used. However, the gamma-ray emission spectra in these datasets are very coarse and lack the precision required to identify specific gamma-ray lines, especially in the low energy range. Therefore, all proton-induced reactions were simulated using the physics models. It is generally assumed that when a proton strikes an atomic nucleus, it initiates a sequence of nuclear reactions, including an intranuclear cascade (INC), pre-equilibrium, evaporation or fission, and finally, the de-excitation of the residual nuclei through gamma-ray emission. This process can be divided into two main stages, and there are several different models for modeling each stage: INC models predict nucleon-nucleon collisions resulting in the emission of prompt particles. Subsequently, evaporation/fission models address some or all of the following: pre-equilibrium, evaporation, fission, and the de-excitation of residual nuclei (Kraan [2015]). In `MCNP6`, the default INC model is Bertini for nucleons and pions, while the `ISABEL` model is used for other particle types (Werner et al. [2017]). For this study, however, the `ISABEL` model was used for all incident particle types. Upon completion of the INC stage, the energy of the highly excited nucleus is dissipated by the evaporation of neutrons, protons, and light ions. This was achieved in this study by using the Dresden evaporation model combined with the Rutherford Appleton Laboratory fission model. Several discrete and continuous energy neutron data libraries were tested for neutron induced interactions. Regarding scattering gamma-ray emissions, the default ACE model was changed to the Cascading Gamma-Ray Multiplicity model, which has been integrated into version 6.2 of `MCNP6` code and has several advantages over the use of ACE data libraries (Wilcox et al. [2014]). Finally, the pulse height tally *F8* was used, which records the number of pulses detected in a user-specified energy bin, analogous to a detector response function.

GEANT4

In GEANT4, the investigation begins by identifying the combinations of models and cross-sections that are most suitable for this analysis. Among those recommended by GEANT4 for medical physics applications, the following physics were selected: QBBC, QGSP_BIC_HP, and QGSP_BIC_AllHP. These physics lists were combined into a modular physics list with the G4EmStandardPhysics_option4. All physics lists are hybrid models that combine the Bertini pre-compound models (for energies $< 6\,\text{GeV}$) with the Binary Ion Cascade. The main differences lie in the cross sections values used and in the application of high precision models for neutrons (HP) and for both neutrons and protons (AllHP) (Agostinelli et al. [2003], Allison et al. [2006, 2016]). In the simulation settings, a custom scoring system capable of recording essential information about each interaction event was developed. This scoring system specifically recorded data on the amount of energy deposited in the detector per event, the time at which each event initially interacted with the detector, and the type of particle involved. Only the energy deposited by photons was exclusively considered to construct the prompt gamma-ray spectrum, while neutrons and electrons were excluded from the analysis. Furthermore, the scoring process was also restricted to the active part of the detector to focus on the relevant interactions.

FLUKA

In the FLUKA toolkit, for the energy ranges employed in this study, the PEANUT package was used, including its General Intra-Nuclear Cascade (GINC). This package provides a higher level of detail and consists of a comprehensive pre-equilibrium stage followed by different equilibrium processes (e.g., evaporation, gamma de-excitation). Inelastic cross sections for hadron-hadron and hadron-nucleus interactions are derived from experimental data and established data tables (Böhlen et al. [2014], Ferrari et al. [2005]). Unlike previous toolkits, FLUKA adopts certain default settings predefined for specific problems. For this study, two settings were used: HADROTHE, adapted for particle therapy calculations, and PRECISIO, designed for precise simulations. The DETECTOR card was employed to gather all the PG spectra.

4.3.2 Gadolinium Response to Ion Irradiation

A set of experiments and equivalent simulations was designed to acquire the photon energy spectra of a GBCA target resulting from ion irradiation. The experimental measurements were based on the setup depicted in Figure 4.1. Either the prompt gamma-ray system or the $CdTe$ detector (when available) to assess the response of the GBCA to ion irradiation. Dotarem® was used with pre administration concentrations (see Section 4.1) as the GBCA for this study. The following subsections describe the *Monte Carlo* physics used in this study, followed by the experimental setups and a description of the obtained measurements.

Monte Carlo Physics

The two primary mechanisms, neutron capture and PIXE, of photon emission as a result of proton interactions with Gd are considered. A similar approach to the previous benchmarking simulation was used, and the physics list was constructed based on `QGSP_BIC_HP` and `G4EmStandardPhysics_option4` modules. The latter has a crucial role in the simulations, as it is responsible for the fluorescent, auger, and PIXE processes. By default, only fluorescence is active; however, the *Auger* production and PIXE were also activated for this simulation. Moreover, the `ECPSSR_ANSTO` model was used. This model is based on the theoretical work of Bakr et al. [2018], providing the proton and α ionization cross section of the K, L and M shells up to $5\,\mathrm{MeV}/u$, in targets with $Z < 93$. Beyond the energy range where shell ionization cross sections are explicitly provided, the ECPSSR model (Paul and Bolik [1993], Paul and Sacher [1989]) employs its internal calculation method. The model is extensible to the ionization cross section σ_h^{PIXE} of a generic ion by scaling the proton ionization cross section, σ_p^{PIXE} using the following scaling relation (Bakr et al. [2022]),

$$\sigma_h^{PIXE} = Z_{eff}^2\, \sigma_p^{PIXE} \left(E_{beam}\, \frac{M_p}{M_h} \right) \tag{4.4}$$

where, Z_{eff} is the effective electric charge, E_{beam} the kinetic energy of the incident ion, M_p and M_h are the masses of the proton and the ion, respectively.

Photon Spectral Response

The first set of experiments aimed to access and compare the spectra of a vial filled with either Dotarem® or water. The experimental setup was analogous to the one in Figure 4.7. The beam and the targets were aligned with the isocenter, and only the photon detector was used. The detector was placed at $90°$ relative to the beam direction and $15.0 \pm 0.5\,\mathrm{cm}$ from the isocenter. Both solutions were directly irradiated with monoenergetic single-spot proton beams with energies of $E_{beam} = 51.82\,\mathrm{MeV}$ (with *Bragg* peak beyond the isocenter) and $E_{beam} = 100.45\,\mathrm{MeV}$ (transmission beam). The corresponding beam currents were $I_{beam} =$

2×10^8 ions s^{-1} and $I_{beam} = 8 \times 10^7$ ions s^{-1}, respectively. Spectra ranging approximately from 30 keV to 700 keV (low energy spectra or LES) and from 350 keV to 7 MeV (high energy spectra or HES) were measured and obtained for the Gd and water solutions. The experience was replicated for the Gd solution using *Monte Carlo* simulations.

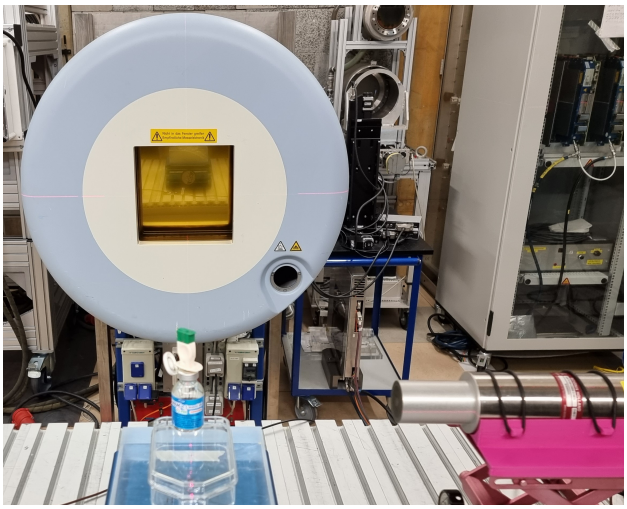

Figure 4.7. Experimental setup used for measuring the energy spectra of water and Dotarem® solution. The photo, taken at the HIT institute, shows the vial target, the nozzle, and the $CeBr_3$ detector. The target vial contained either water or Dotarem®.

Signal Quantification

As discussed later (see Section 5), the previous results narrow the focus of this study to the gadolinium K_α and K_β characteristics *X-rays* emissions induced by proton irradiation of the Dotarem® and water solution. In a subsequent step, the quantification of the gadolinium signal as a function of the dose is focused on. In this case, three different proton beam energies were used, $E_{beam} = 51.82$ MeV, 55.34 MeV and 58.72 MeV. The individual depth-dose profile of each beam is depicted in Figure 4.8. The corresponding deposited doses per ion in the gadolinium target, determined by *Monte Carlo* simulations were, $(1.63 \times 10^{-10} \pm 8.4 \times 10^{-12})$ Gy ion^{-1}, $(1.85 \times 10^{-12} \pm 8.1 \times 10^{-12})$ Gy ion^{-1}, and $(2.04 \times 10^{-12} \pm 7.7 \times 10^{-14})$ Gy ion^{-1}, respectively. The photon detector was placed at $90°$ relative to the beam direction and 25.0 ± 0.5 cm from the isocenter. Due to the poor resolution of the photon detector, the K_α and K_β were merged in the spectra (see Section 5), and therefore, quantified as one signal, $K^{Gd}_{\alpha,\beta}$.

To evaluate the influence of the dose rate on the photon spectra response, additional measurements with a fixed proton beam energy of $E_{beam} = 55.34$ MeV were conducted at different dose rates, 0.03 Gy s^{-1}, 0.09 Gy s^{-1} and 0.30 Gy s^{-1}. The irradiation time was varied to achieve the same set of doses (2.5, 5.0, 7.5, 10 and 12.5 Gy) for each dose rate.

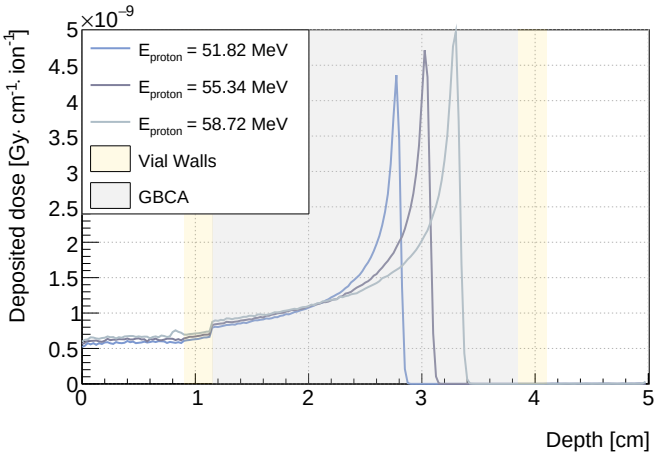

Figure 4.8. Depth-dose profile for three different beam energies: $E_{beam} = 51.82\,\text{MeV}$ (blue), $55.34\,\text{MeV}$ (purple) and $58.72\,\text{MeV}$ (green), resulting from proton irradiation of a vial filled with Dotarem®.

Two sets of measurements were acquired, one with the photon detector at $90°$ relative to the beam direction and $25.0 \pm 0.5\,\text{cm}$ from the isocenter (vial) and the other at $50.0 \pm 0.5\,\text{cm}$.

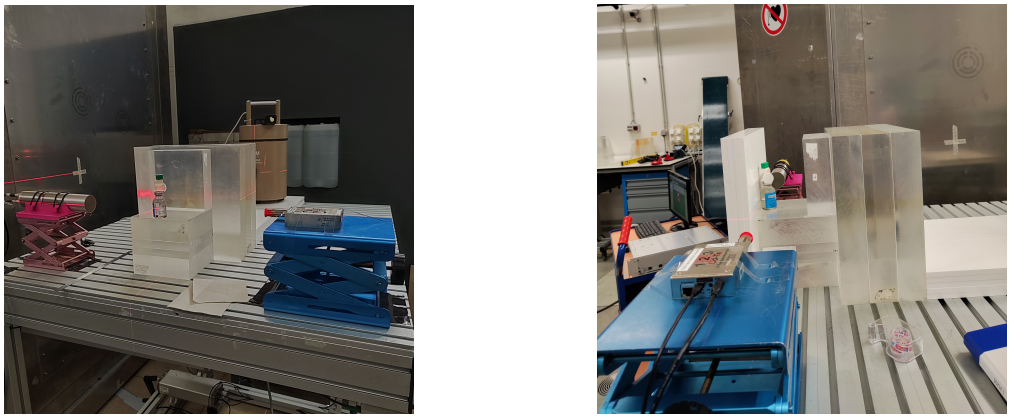

(a) Vial Irradiation **(b)** Vial Irradiation with PMMA

Figure 4.9. Experimental setup used for ion (proton, helium and carbon) irradiation of water and Dotarem® solutions without (a) and with (b) a PMMA between the nozzle and the target. The photos, taken at the HIT institute, show the vial target, the $CeBr_3$ detector and the $CdTe$ detector. A energy spectra was measured for each configuration.

Various Charged Ions

To evaluate the capabilities of PGS in detecting GBCA agents for different charged ions, a vial filled with either Dotarem® or water was irradiated. The charged ions used for irradiation were: proton with an energy of $51.82\,\text{MeV}$, helium with $54.15\,\text{MeV u}^{-1}$, as well as carbon ions with an energy of $95.67\,\text{MeV u}^{-1}$. The beam intensities were, $2 \times 10^8\,\text{ions s}^{-1}$,

2×10^7 ions s^{-1}, 2×10^6 ions s^{-1}, respectively. For each irradiation, the photon spectra were obtained using the photon and the $CdTe$ detector. The experimental setup used for these measurements is shown in Figure 4.9. Similar to previous experiments, the detectors were places at $90°$ relative to the beam direction and 25.0 ± 0.5 cm from the isocenter. To preliminarily determine whether the $K^{Gd}_{\alpha,\beta}$ emission was primarily due to PIXE or neutron capture, four PMMA slabs of 1 cm each were introduced between the nozzle and the target, positioning the proton beam's end-of-range within the PMMA. This setup ensures that if a signal is detected, it is highly likely to be due to neutron capture.

Underlying Physics

Previous measurements indicate that at lower energies, the primary physical process associated with $K^{Gd}_{\alpha,\beta}$ emission is PIXE. Through *Monte Carlo* simulations, the underlying mechanisms of *X-ray* emission by Gd were studied. Before obtaining the cross-sections for processes associated with the irradiation of Dotarem®, benchmarking was successfully conducted using a thin Gd target, with the results shown in Figures 4.10 and 4.11. Additionally simulations involved the study of the Gd PIXE and neutron capture cross-sections for a thin target consisted of GBCA and for different thickness of PMMA.

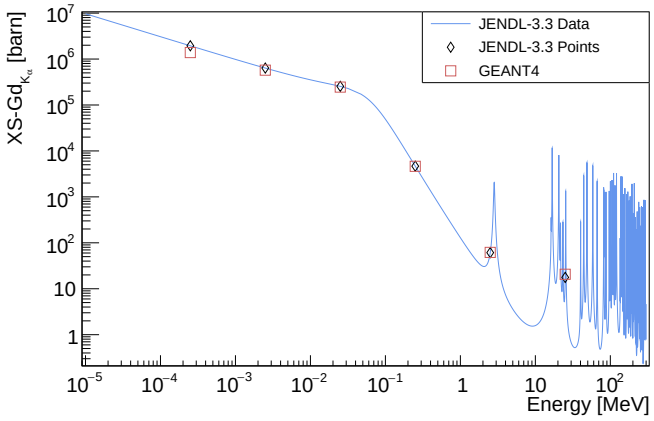

Figure 4.10. Benchmarking of neutron capture cross-sections in GEANT4 for a thin Gd target.

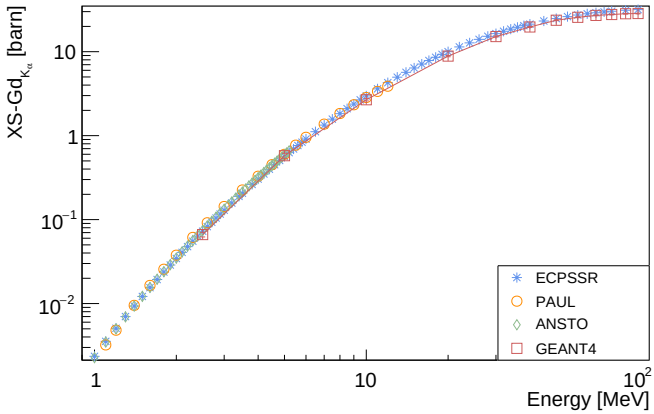

Figure 4.11. Benchmarking of PIXE cross-sections in GEANT4 for a thin Gd target.

4.3.3 Dose-Dependent Spectra Variations in Gadolinium

[2]*Monte Carlo* simulations (using the same physics described in the previous section) were performed using `GEANT4` to investigate the dose-dependent spectra of GBCA under various conditions of proton irradiation and evaluate the feasibility of using GBCA for in vivo dosimetry. The study used an elliptic cylinder water phantom with a major and minor axis of 25 cm and 15 cm, respectively. At the center of the phantom, a target volume measuring $2 \times 2 \times 2\,\text{cm}^3$, composed of Dotarem®, was placed, as shown in Figure 4.12. A uniform dose of 2 Gy was delivered to the target using pencil beam scanning, and the deposited doses in the target, as well was the phase space of secondary photons, were analyzed under different transverse and longitudinal displacements of the target. The phase space was recorded in a box of $7.5 \times 7.5 \times 7.5\,\text{cm}^3$, surrounding the target. The next sub-sections describe in detail the treatment plan used and the applied conditions.

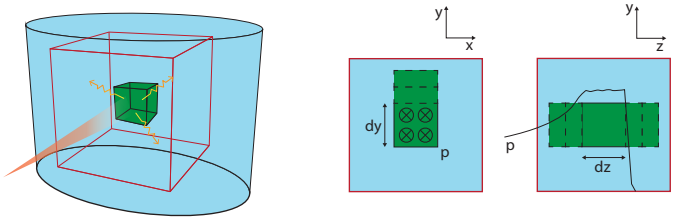

Figure 4.12. Schematic representation of the setup used in the *Monte Carlo* simulations of the Dose-Dependent Spectra Variations in Gadolinium and Simultaneous Range and Tumor Localization using Gadolinium campaigns. The blue area represents the elliptical cylinder water phantom, the green area represents the target and the scorer volume is delineated in red.

Design and Optimization of the Treatment Plan

An optimized pencil beam scanning treatment plan was created to uniformly cover the entire target (tumor) volume with a physical dose of 2 Gy per fraction, as is typical in a fractionated irradiation schedule. Pencil beams were arranged in a squared matrix with a theoretical spacing of 3 mm along the longitudinal (beam) direction and 5 mm in the transverse orthogonal plane. This resulted in the use of 8 energy layers ranging from 124.44 MeV to 139.27 MeV (see table 4.2) and 25 points per layer (see table 4.3), forming a total 200 pencil beams. In practice, the available energies at HIT were used, adding slightly different distances for the longitudinal spacing. The layers and points configuration are depicted in Figure 4.13.

[2]Note: This section includes modified parts from the submitted work: Brás, M., **Freitas, H.**, Gonçalves, P., & Seco, J. (2024). In vivo dosimetry for proton therapy: A Monte Carlo study of the Gadolinium spectral response throughout the course of treatment.

Table 4.2. Energy layer number, initial proton kinetic energy (E_{Beam}), beam lateral FWHM and the corresponding CSDA range used in the Dose-Dependent Spectra Variations in Gadolinium campaign.

Energy Layer	$E_{Beam}\,[MeV]$	$FWHM$ [cm]	$R_{80}\,[cm]$
1	124.44	1.34	113.73
2	126.90	1.33	117.24
3	129.32	1.33	120.80
4	131.11	1.32	123.28
5	133.48	1.31	126.79
6	135.23	1.31	129.35
7	137.55	1.30	132.90
8	139.2 7	1.30	135.64

Table 4.3. Sorted pencil beam number in the transverse plan and their correspondent *Cartesian* coordinates in cm for the treatment plan (with isocenter at $(x, y, z) = (0, 0, 12.5)$ cm) used in the Dose-Dependent Spectra Variations in Gadolinium campaign.

Point 1-5	Point 6-10	Point 11-15	Point 16-20	Point 21-25
(-1.0, -1.0)	(-0.5, -1.0)	(0, -1.0)	(0.5, -1.0)	(1.0, -1.0)
(-1.0, -0.5)	(-0.5, -0.5)	(0, -0.5)	(0.5, -0.5)	(1.0, -0.5)
(-1.0, 0)	(-0.5, 0)	(0, 0)	(0.5, 0)	(1.0, 0)
(-1.0, 0.5)	(-0.5, 0.5)	(0, 0.5)	(0.5, 0.5)	(1.0, 0.5)
(-1.0, 1.0)	(-0.5, 1.0)	(0, 1.0)	(0.5, 1.0)	(1.0, 1.0)

The treatment plan optimization was based on the Sequential Least Squares Quadratic Programming (SLSQP, Kraft [1988]) algorithm, an iterative method for constrained non-linear optimization problems. The minimization problem, which minimizes the square deviation of the dose, is given by

$$\begin{aligned} \min_{\mathbf{w}} \quad & f(\mathbf{w}) = \frac{\lambda_{target}}{N_{target}} \sum_i \left(D_i(\mathbf{w})^t - D_{target}\right)^2 + \frac{\lambda_{tissue}}{N_{tissue}} \sum_j \left(D_j(\mathbf{w}) - D_{tissue}\right)^2 \\ \text{subject to} \quad & D_j(\mathbf{w}) \leq D_{\text{max}}, \forall j \in \text{tissue} \\ & w_k \geq 0, \forall k \end{aligned} \tag{4.5}$$

where, $\mathbf{w}$ are the weights of each pencil beam, $D_i(\mathbf{w})$ is the dose at the i-th voxel in target region, D_{target} is the prescribed dose to the target, $D_j(\mathbf{w})$ is the dose at the j-th voxel in healthy tissue, D_{tissue} and D_{max} are the reference and maximum doses in healthy tissue,

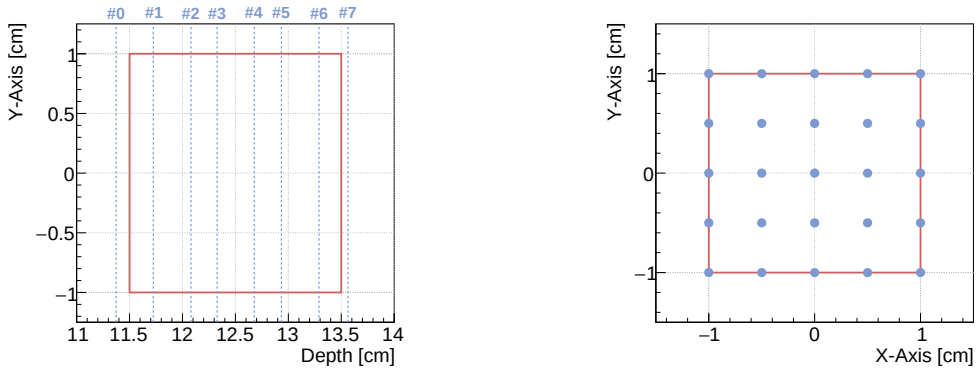

Figure 4.13. Longitudinal (zy) and transverse planes for the treatment plan (with isocenter at $(x, y, z) = (0, 0, 12.5)$ cm) used in the Dose-Dependent Spectra Variations in Gadolinium campaign. The energy layers (dashed, blue), the distribution of pencil beams (circle, blue) in the transversal plan and the target limits (solid, red) are represented.

λ_{target} and λ_{tissue} are penalty factors for the target and tissue regions, and N_{target} and N_{tissue} are the number of voxels in the target an non-target regions, respectively. No margins were applied when creating the optimized treatment plan. The resulting dose distribution in the target for the longitudinal plan is depicted in Figure 4.14.

Longitudinal and Transversal Displacements

To recreate a realistic scenario in which target movements occur both intra- and inter-fraction, the target was shifted both in transversal and longitudinal axis. Since the adopted geometry is simple and symmetrical, movements in the transversal plane were represented by 1.0 mm, 3.0 mm, 8.5 mm and 16.0 mm shifts only in y-axis and in the positive direction relatively to the target's original position. In the longitudinal axis, the same shifts were applied in both the upstream (toward the beam nozzle) and downstream directions. The effects of these movements on dose to target are depicted in Figure 4.15 as dose-volume histograms (DVHs) of the Gross Tumor Volume (GTV) for each scenario. For the optimal treatment plan, the dose received by 95% of the target volume ($D_{95\,\%}$) is 1.96 Gy, and $100.0\,\%$ of the target volume receives at least $95\,\%$ ($V_{95\,\%}$) of the prescribed dose. The corresponding metrics for scenarios with target displacements are presented in Table 4.4.

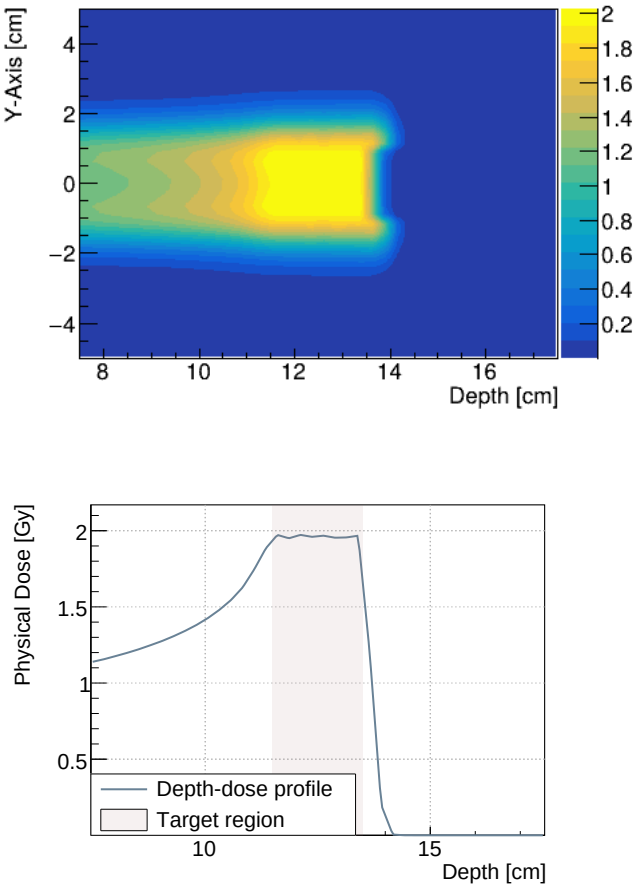

Figure 4.14. Dose distribution map (upper) and dose-depth profile (bottom) for the optimized treatment plan. The targets limits are represented by the red region.

Table 4.4. Dose metrics, $D_{95\,\%}$ and $V_{95\,\%}$, for the GTV under different target displacement scenarios in both transverse (positive direction of y-axis) and longitudinal (downstream and upstream) directions in the optimized treatment plan. The reference values for no displacement are $D_{95\,\%} = 1.96\,\text{Gy}$ and $V_{95\,\%} = 100.0\,\%$.

	Transversal		Downstream		Upstream	
Shift [mm]	$D_{95\,\%}$ [Gy]	$V_{95\,\%}$ [%]	$D_{95\,\%}$ [Gy]	$V_{95\,\%}$ [%]	$D_{95\,\%}$ [Gy]	$V_{95\,\%}$ [%]
1.0	1.95	99.42	1.94	96.72	1.96	100.0
3.5	1.76	85.57	1.25	83.12	1.93	97.51
8.5	1.00	57.48	0.04	57.83	1.69	73.51
16.0	0.18	16.12	0.00	24.67	1.48	38.82

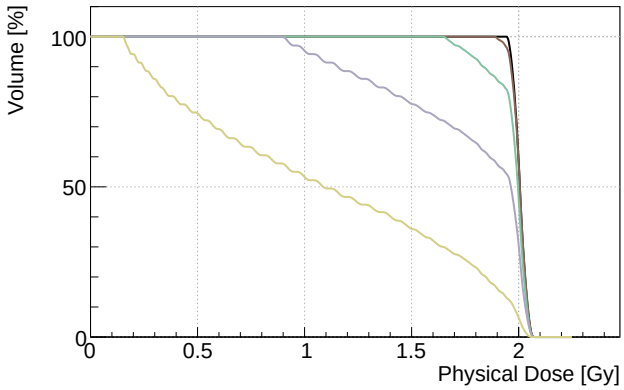

(a) Transversal displacement

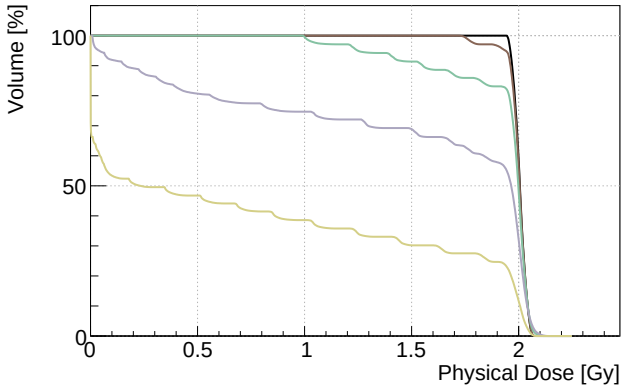

(b) Downstream displacement

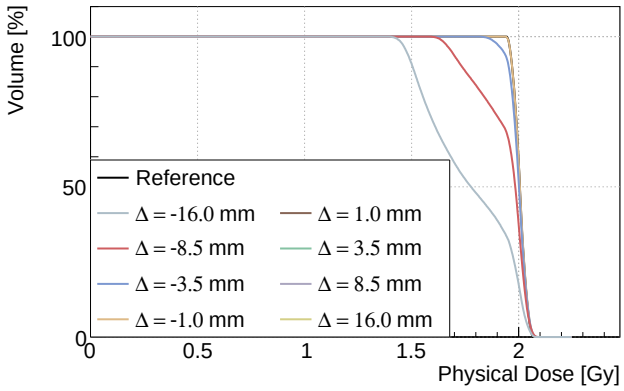

(c) Upstream displacement

Figure 4.15. DVHs of the GTV for the optimized treatment plan (solid black line) without target displacements, and with target displacements: (a) transverse displacement along the positive y-axis, (b) displacement in the downstream direction, and (c) displacement in the upstream direction.

4.3.4 Range and Tumor Monitoring using Gadolinium and PGS

The *Monte Carlo* simulation shown in Figure 4.12, along with the treatment plan described in Section 4.3.3, was used to evaluate how PGS can be combined with GBCA to achieve synchronized range monitoring and tumor localization. The previous score volume was divided into 2 mm slits, and the photon spectra were recorded for each slit. By extracting the features of $K^{Gd}_{\alpha,\beta}$ emission and C^{12} de-excitation line, range and tumor localization measurements for individual energy layers were obtained. Additionally, cases of beam overshoot and beam undershoot were simulated to further demonstrate the potential of this technique.

Chapter 5

Results

This chapter presents all the experimental and *Monte Carlo* results divided according to the experimental campaigns defined in the research methodology chapter. All experimental data were collected at HIT and MIT in collaboration with DKFZ.

5.1 Prompt Gamma-Ray Benchmarking

[1]This campaign started by irradiating the PMMA target with single-spot and monoenergetic proton beams in the first set of experiments. Figure 5.1 shows the spectra obtained for the various beam energies used in this work.

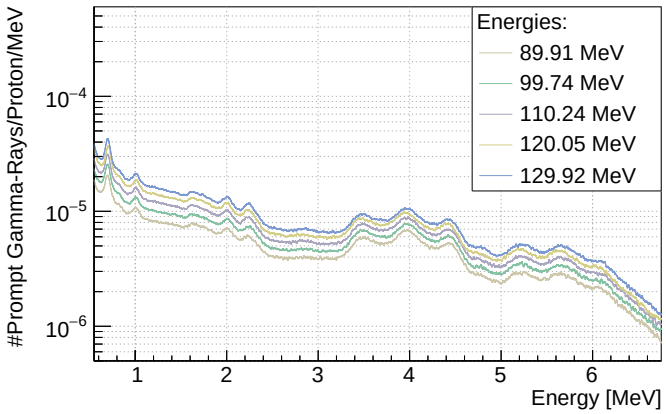

Figure 5.1. Prompt gamma-ray spectra resulting from proton irradiation of PMMA. Measurements were obtained for different proton energies.

[1]Note: This section includes modified excerpts from the submitted work: **Freitas, H.**, Nobakht, E., Grüner, F., & Seco, J. (2024). A Comparative Analysis of GEANT4, MCNP6, and FLUKA on Proton-Induced Gamma-Ray Simulation.

The most statistically relevant lines in the spectra, resulting from inelastic interactions of the proton with the target, include the boron ($^{10}B^{*}_{1.740MeV} \rightarrow {}^{10}B^{*}_{0.718\,\mathrm{MeV}}$, $^{10}B^{*}_{0.718\,\mathrm{MeV}} \rightarrow {}^{10}B_{g.s.}$), carbon ($^{11}C^{*}_{2.000\,\mathrm{MeV}} \rightarrow {}^{11}C_{g.s.}$, $^{12}C^{*}_{4.439\,\mathrm{MeV}} \rightarrow {}^{12}C_{g.s.}$), nitrogen ($^{14}N^{*}_{3.948MeV} \rightarrow {}^{10}B^{*}_{2.313\,\mathrm{MeV}}$, $^{14}N^{*}_{2.313\,\mathrm{MeV}} \rightarrow {}^{14}N_{g.s.}$), and oxygen de-excitation lines ($^{16}O^{*}_{6.130\,\mathrm{MeV}} \rightarrow {}^{16}O_{g.s.}$). Additionally, neutron activation of hydrogen ($n + {}^{1}H \rightarrow {}^{2}H + \gamma_{2.223\,\mathrm{MeV}}$) is present.

Monte Carlo Spectra

The benchmark analysis began by selecting the most suitable options for `MCNP6`. Then, the simulations were ran using the data tables and models. The `MCNP6` results, for the beam energy of $E_{beam} = 110.24\,\mathrm{MeV}$, are shown in Figure 5.2. It is evident from the figure that data tables are inconsistent when compared to the experimental spectra. Therefore, all the proton-induced reactions were simulated using physics models. Among the various models tested, the `ISABEL` model provided the best fit to the data. However, none of the models could account for the oxygen de-excitation line ($^{16}O^{*}_{6.130\,\mathrm{MeV}} \rightarrow {}^{16}O_{g.s.}$) observed in the experimental results.

In `GEANT4`, two models were tested, the `QBBC` and the `QGSP_BIC` and its extensions. The results for both models and their extensions are depicted in Figure 5.3. The `QGSP_BIC_HP`, excluding background considerations, shows good agreement with the experimental data for energies below $3\,\mathrm{MeV}$. However, an exception is the ^{11}C de-excitation line, which is overestimated. Regarding the ^{12}C de-excitation line, it is underestimated, which is consistent with findings in previous studies (Wrońska et al. [2021]). Similar to the results from `MCNP6`, the oxygen de-excitation line is also missing from the spectra.

In `FLUKA`, only two default options were used, the `HADROTHE` and `PRECISIO` defaults. The results, depicted in Figure 5.4, exhibit similar behavior between the two, with the former displaying a small artifact near the double escape peak of the carbon de-excitation line ($^{12}C^{*}_{4.439\,\mathrm{MeV}} \rightarrow {}^{12}C_{g.s.}$). Although the oxygen de-excitation line is more prominent in FLUKA, it is still significantly underestimated.

`EMPIRICAL` Spectra

The results observed in Figures 5.2 to 5.4 are not satisfactory enough for future research on PGS, especially regarding the oxygen PG line, $^{16}O^{*}_{6.130\,\mathrm{MeV}} \rightarrow {}^{16}O_{g.s.}$. To address this issue, a new model was developed to simulate the de-excitations resulting from inelastic interactions between protons and carbon and oxygen nuclei. This new model is referred to as the `EMPIRICAL` model. The new model was integrated into the `GEANT4` toolkit due to its open-source nature, though it can be implemented in any generic simulator toolkit. The model relies on experimental and theoretical cross-sections, σ_{PG}, obtained from the literature[2],

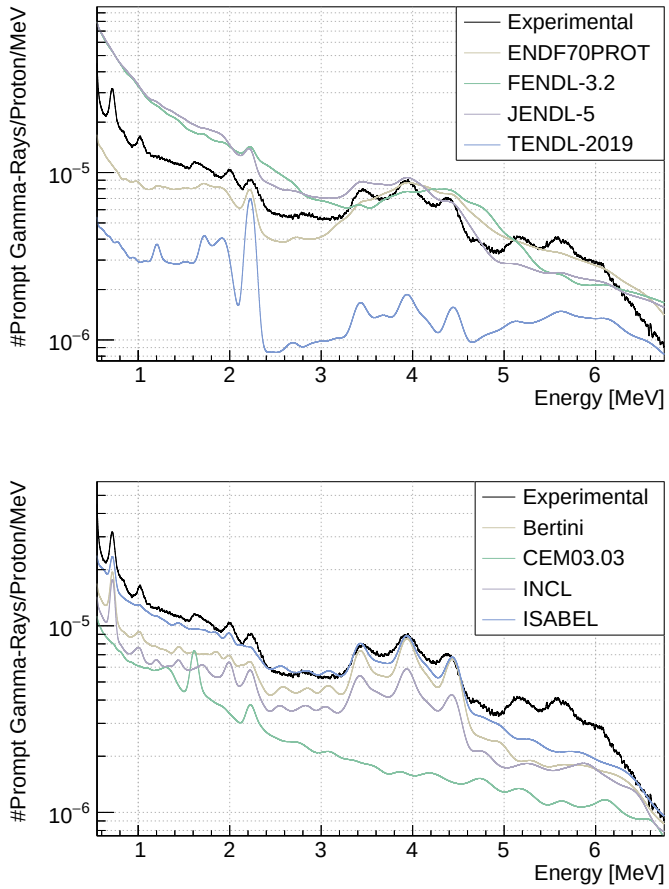

Figure 5.2. Simulated prompt gamma-ray spectra in MCNP6 using various nuclear data tables (upper) different intra-nuclear cascade models (bottom).

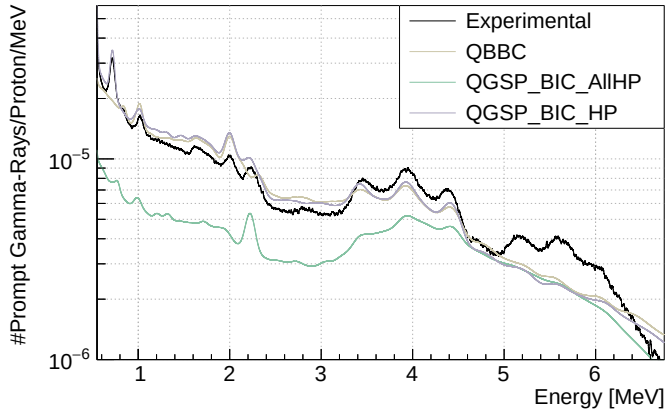

Figure 5.3. Simulated prompt gamma-ray spectra in GEANT4 using a model based on experimental and theoretical cross-sections obtained from the literature.

particularly when sufficient experimental data is not available. This model disregards all gamma-ray emissions resulting from inelastic processes during a G4Step of primary parti-

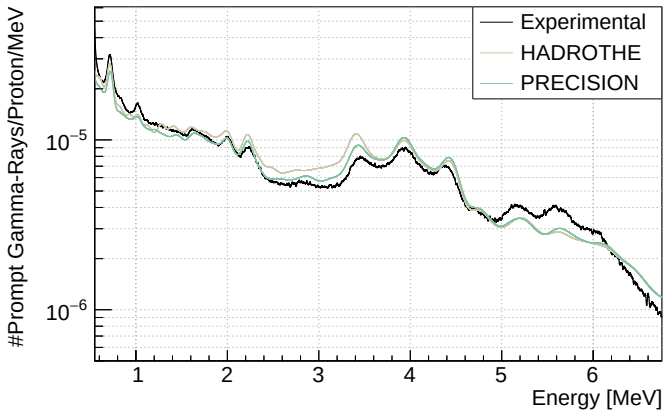

Figure 5.4. Simulated prompt gamma-ray spectra in FLUKA for different defaults.

cles and evaluates whether de-excitation emissions occur. At each step and for each possible gamma-ray energy of interest, the step length, Δx, and the kinetic energy, E_{kin} of the particle are obtained, then the mean free path (see equation 2.7), is determined, followed by the cumulative probability, $1 - \exp^{-\frac{\Delta x}{\lambda}}$. Finally, a random number is generated; if the event is accepted, a new secondary gamma-ray with a specific energy of a de-excitation line is added to the event for subsequent processing. The resulting PGS spectra for $E_{beam} = 110.24\,\text{MeV}$ is depicted in Figure 5.5.

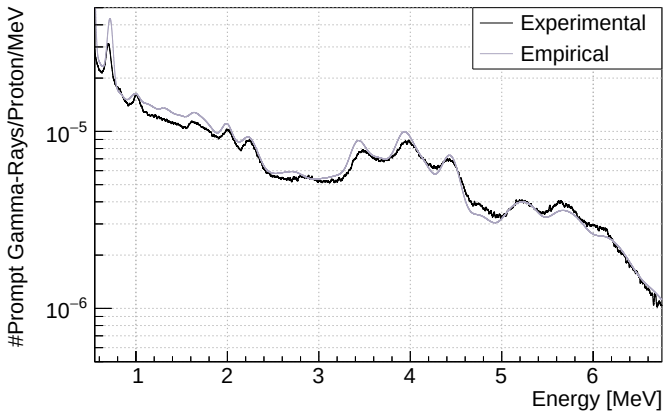

Figure 5.5. Simulated prompt gamma-ray spectra in GEANT4 using a model based on experimental and theoretical cross-sections obtained from the literature.

[2]Data based on results from Belhout et al. [2007], Boromiza et al. [2020], Dyer et al. [1981], Foley et al. [1962], Hosobuchi et al. [2023], Kiener et al. [1998], Kozlovsky et al. [2002], Lang et al. [1987], Lesko et al. [1988], Narayanaswamy et al. [1981], Rahma et al. [2023], Yoneda et al. [2023].

Quantification of Spectra Lines

The most relevant statistical results for the lines are depicted in Figures 5.6 to 5.9 as a function of beam energy for both experimental and *Monte Carlo* data.

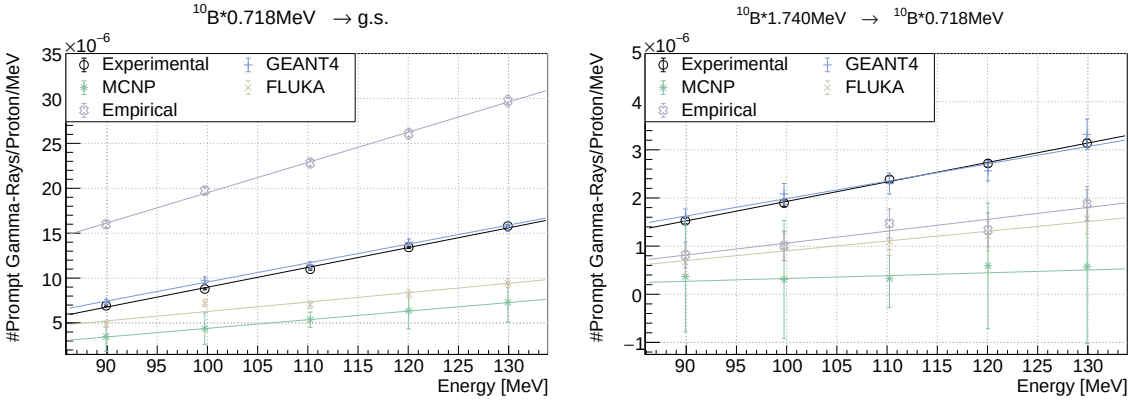

Figure 5.6. Quantification and comparison of the ^{10}B de-excitation lines observed in the PGS resulting from proton irradiation of PMMA.

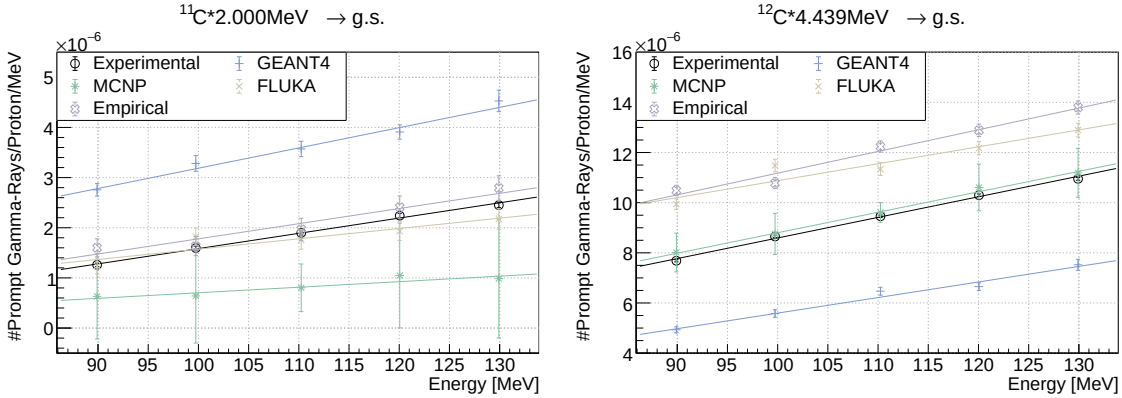

Figure 5.7. Quantification and comparison of the ^{11}C and ^{12}C de-excitation lines observed in the PGS resulting from proton irradiation of PMMA.

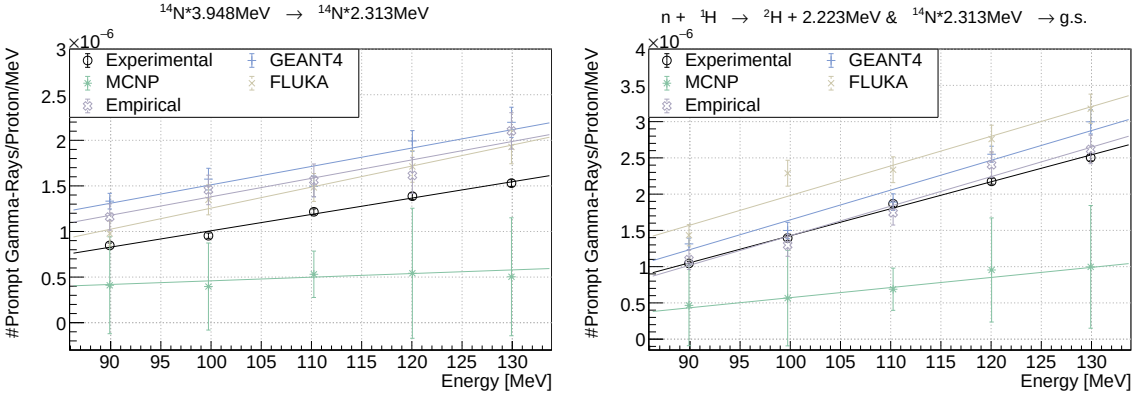

Figure 5.8. Quantification and comparison of the ^{14}N and ^{2}H (resulting from neutron capture of ^{1}H) de-excitation lines observed in the PGS resulting from proton irradiation of PMMA.

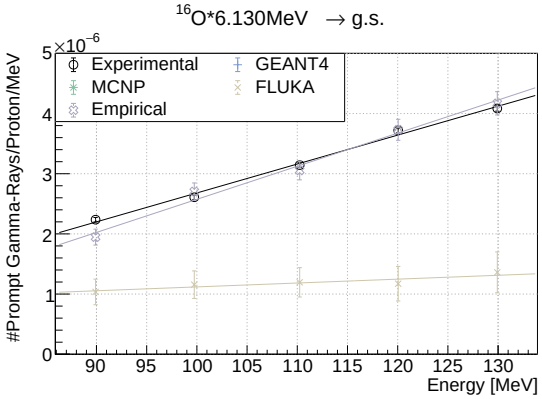

Figure 5.9. Quantification and comparison of the ^{16}O de-excitation line observed in the PGS resulting from proton irradiation of PMMA. The results of `GEANT4` and `MCNP6` are suppressed due to their inability to reproduce the ^{16}O de-excitation line.

5.2 Gadolinium Response to Ion Irradiation

This campaign began by irradiating vials filled with either Dotarem® or water with monoenergetic proton beams to better understand the gadolinium (Gd) response to ion irradiation (see Figure 4.7). Figures 5.10 to 5.13 show the spectra obtained from both solutions across different spectral energy ranges. The measurements were performed using two beam modalities: one with the *Bragg* peak positioned inside the sample and the other in the transmission beam modality. The mirrored experiment results using *Monte Carlo* simulations are depicted in Figure 5.14 and 5.15 only for the Gd solution target.

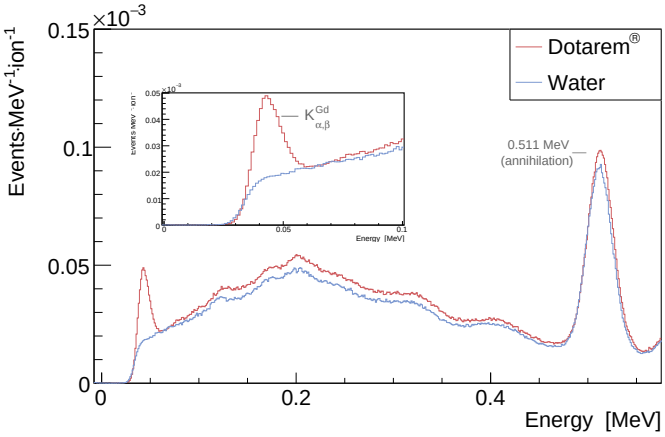

Figure 5.10. Low energy spectra of vials containing Dotarem® (solid red) and water (solid blue), irradiated by a proton beam with $E_{beam} = 51.82\,\text{MeV}\,\text{u}^{-1}$ and $I_{beam} = 2 \times 10^8\,\text{ions}\,\text{s}^{-1}$. The inset highlights the $K^{Gd}_{\alpha,\beta}$ signal.

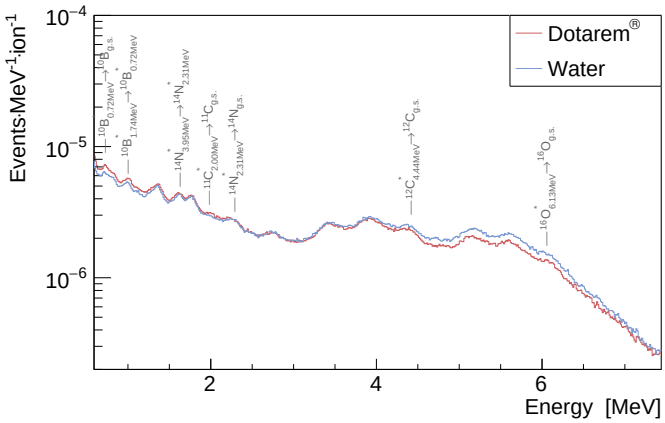

Figure 5.11. High energy spectra of vials containing Dotarem® (solid red) and water (solid blue), irradiated by a proton beam at $E_{beam} = 51.82\,\text{MeV}\,\text{u}^{-1}$ and $I_{beam} = 2 \times 10^8\,\text{ions}\,\text{s}^{-1}$. The most relevant prompt gamma-ray lines are labeled in the figure.

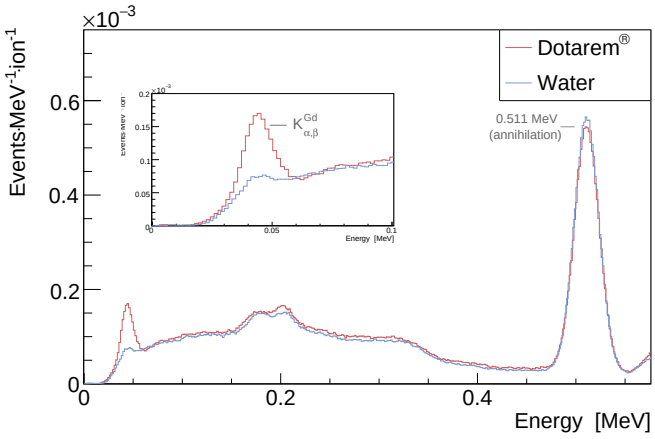

Figure 5.12. Low energy spectra of vials containing Dotarem® (solid red) and water (solid blue), irradiated by a transmission proton beam with $E_{beam} = 100.45\,\text{MeV u}^{-1}$ and $I_{beam} = 8 \times 10^7\,\text{ions s}^{-1}$. The inset highlights the $K^{Gd}_{\alpha,\beta}$ signal.

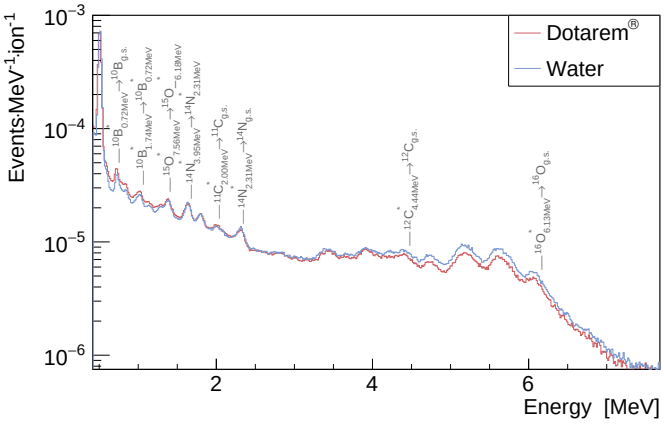

Figure 5.13. High energy spectra of vials containing Dotarem® (solid red) and water (solid blue), irradiated by a transmission proton beam with $E_{beam} = 100.45\,\text{MeV u}^{-1}$ and $I_{beam} = 8 \times 10^7\,\text{ions s}^{-1}$. The most relevant prompt gamma-ray lines are labeled in the figure.

When comparing the Gd-based solution LES and water spectra, the results reveal a distinguishable peak. The Gd peak can be identified as electronic transitions (K_α and K_β) related emissions. Due to the poor resolution of the detector, the K'edges peaks merge in this region of the spectra. The merged peak was designated as the $K^{Gd}_{\alpha,\beta}$ signal. At higher energies, no peaks expected from Table 3.1 were observed.

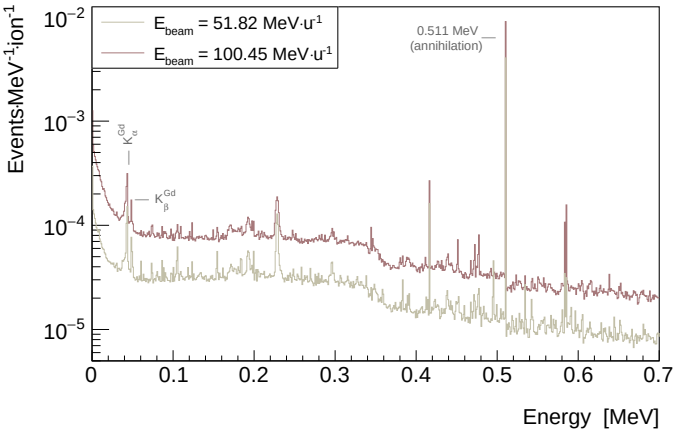

Figure 5.14. *Monte Carlo* simulated low energy spectra of a vial containing Dotarem®, irradiated by a proton beams with energies of $51.82\,\mathrm{MeV\,u^{-1}}$ (solid, yellow) and $E_{beam} = 100.45\,\mathrm{MeV\,u^{-1}}$ (solid, red). The K_{α}^{Gd} and K_{β}^{Gd} peaks are clearly identified and distinguished.

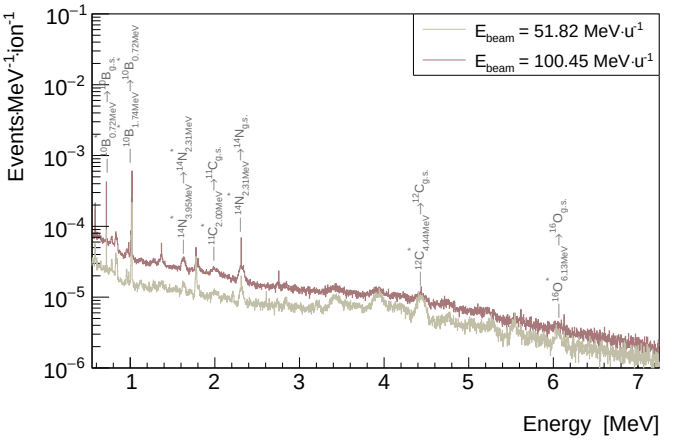

Figure 5.15. *Monte Carlo* simulated high energy spectra of a vial containing Dotarem®, irradiated by a proton beams with energies of $51.82\,\mathrm{MeV\,u^{-1}}$ (solid, yellow) and $E_{beam} = 100.45\,\mathrm{MeV\,u^{-1}}$ (solid, red). The most relevant prompt gamma-ray lines are labeled in the figure.

The *Monte Carlo* simulations produced a spectra response similar to the experimental results regarding the Gd emissions presented in Table 3.1. The high resolution of the spectra allow the individual identification of K_{α}^{Gd} and K_{β}^{Gd} peaks. The several lines observed in the spectra are not related with Gd response or their yield is to low to draw any conclusions. As a result of the first experiments in the following steps, only the LES spectra were considered.

Photon Spectral Response

The $K^{Gd}_{\alpha,\beta}$ signal was characterized for three different proton beam energies, corresponding to three different doses, as shown in Figure 5.16. The dose-rate dependence of the photon detector was also analyzed at three different intensities. The results are presented in Figures 5.17 for two different setups, with the photon detector positioned at 25.0 ± 0.5 cm and 50.0 ± 0.5 cm from the isocenter. To better understand this dose rate dependent behavior, Figures 5.18 and 5.19 present an analysis of the raw data processing parameters, $R^2_{adjusted}$ and λ.

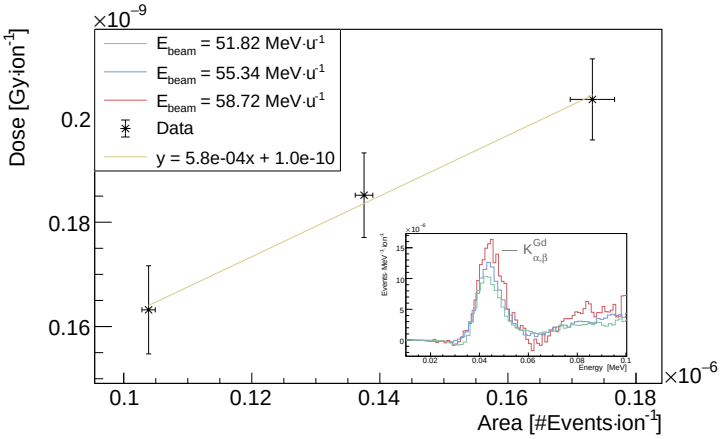

Figure 5.16. The $K^{Gd}_{\alpha,\beta}$ signal as a function of the dose for a vial filled with Dotarem®, irradiated with three different proton beam energies: $E_{beam} = 51.82\,\mathrm{MeV\,u^{-1}}$ (solid green), $55.34\,\mathrm{MeV\,u^{-1}}$ (solid blue), and $58.72\,\mathrm{MeV\,u^{-1}}$ (solid red).

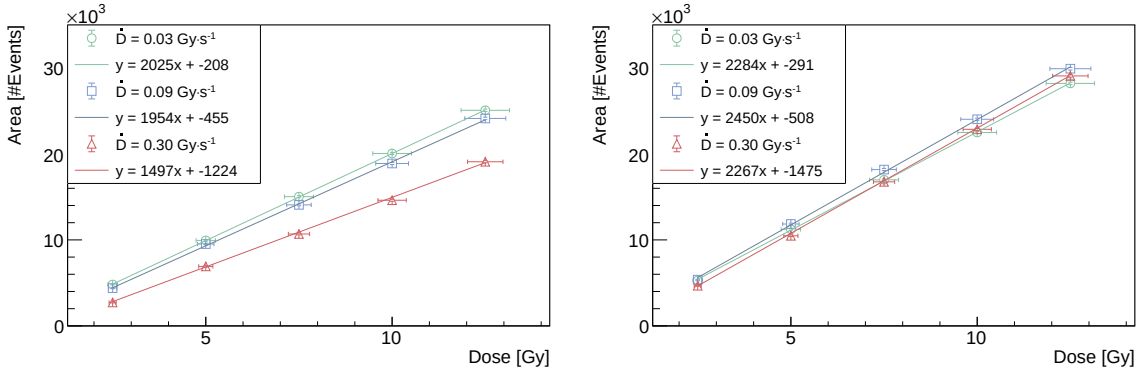

(a) Detector at 25.0 ± 0.5 cm

(b) Detector at 50.0 ± 0.5 cm

Figure 5.17. The $K^{Gd}_{\alpha,\beta}$ signal as a function of the dose and dose-rate ($\dot{D}$) for a vial filled with Dotarem® and irradiated by protons with $E_{beam} = 55.34\,\mathrm{MeV\,u^{-1}}$. The signal was measured with a detector at (a) 25.0 ± 0.5 cm and (b) 50.0 ± 0.5 cm from the vial.

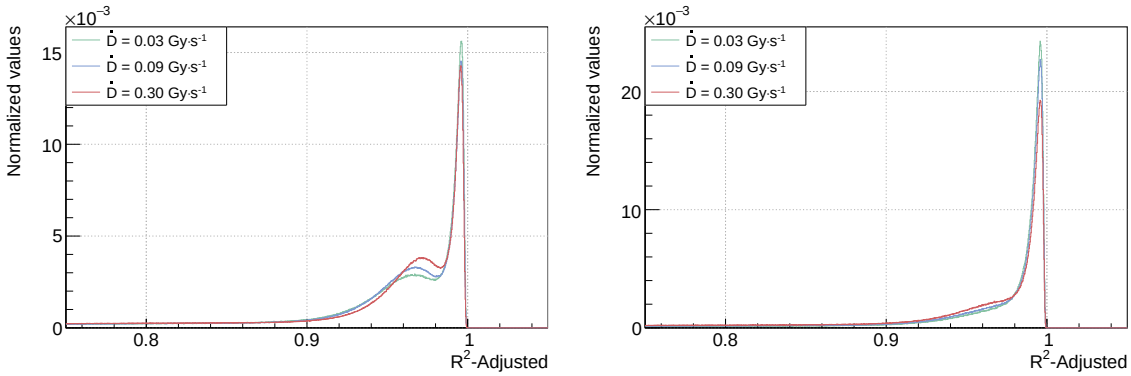

(a) Detector at 25.0 ± 0.5 cm **(b)** Detector at 50.0 ± 0.5 cm

Figure 5.18. Distribution of the $R^2_{adjusted}$ parameter for different dose rates, $0.03\,\mathrm{Gy\,s^{-1}}$ (solid, green), $0.09\,\mathrm{Gy\,s^{-1}}$ (solid, blue) and $0.30\,\mathrm{Gy\,s^{-1}}$ (solid, red), and positions of the detector: (a) at 25.0 ± 0.5 cm cm from the target and (b) at 50.0 ± 0.5 cm cm of the target.

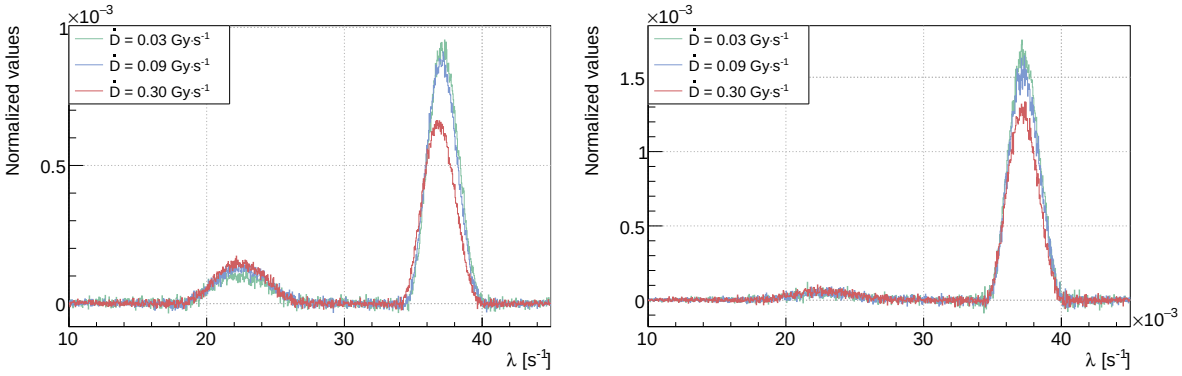

(a) Detector at 25.0 ± 0.5 cm **(b)** Detector at 50.0 ± 0.5 cm

Figure 5.19. Distribution of the λ parameter for different dose rates, $0.03\,\mathrm{Gy\,s^{-1}}$ (solid, green), $0.09\,\mathrm{Gy\,s^{-1}}$ (solid, blue) and $0.30\,\mathrm{Gy\,s^{-1}}$ (solid, red), and positions of the detector: (a) at 25 cm from the target and (b) at 50 cm of the target.

Various Charged Ions

Spectral measurements resulting from GBCA irradiation with different ions are shown in Figure 5.20 and 5.21, for the $CeBr_3$ and the $CdTe$ detector. A significant improvement in the resolution of the spectra is noticed with the $CdTe$ detector, at the cost a lower photon detection efficiency due to its reduced active volume. The quantification of the $K_\alpha + K_\beta$ peaks of Gd for the spectra measured with the $CdTe$ yielded areas of $(8.12 \pm 0.49) \times 10^{-5}$ events, $(1.30 \pm 0.01) \times 10^{-3}$; events, and $(2.22 \pm 0.01) \times 10^{-2}$; events for proton, helium and carbon, respectively. The corresponding doses were, $(1.63 \pm 0.11) \times 10^{-10}$ Gy proton^{-1},

$(1.11 \pm 0.11) \times 10^{-9}$ Gy $helium^{-1}$ and $(6.59 \pm 0.46) \times 10^{-9}$ Gy $carbon^{-1}$. The insertion of a 4 cm slab between the nozzle and the Gd target resulted in the suppression of the Gd signal, most likely indicating that the interactions were primarily due to PIXE.

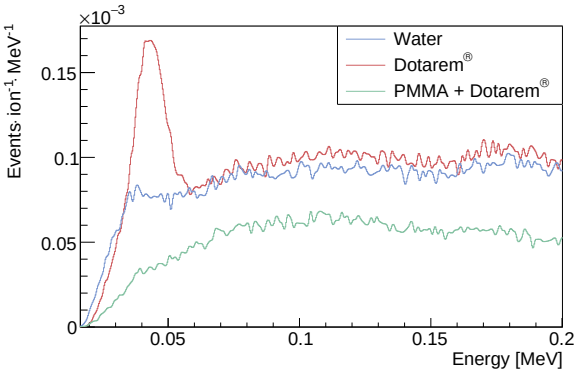

(a) Proton irradiation

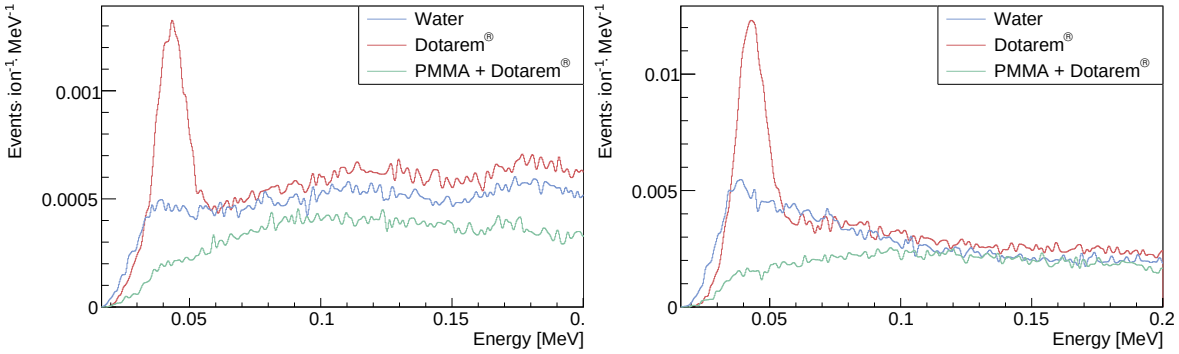

(b) Helium irradiation

(c) Carbon irradiation

Figure 5.20. Spectra measurements of a vial filled with water or Dotarem®, irradiated with (a) protons, (b) helium, and (c) carbon. The spectra were obtained using the $CeBr_3$ detector, including an additional configuration where 4 cm of PMMA was placed in front of the gadolinium solution.

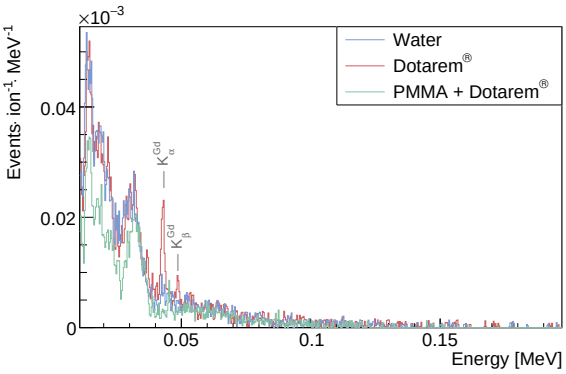

(a) Proton irradiation

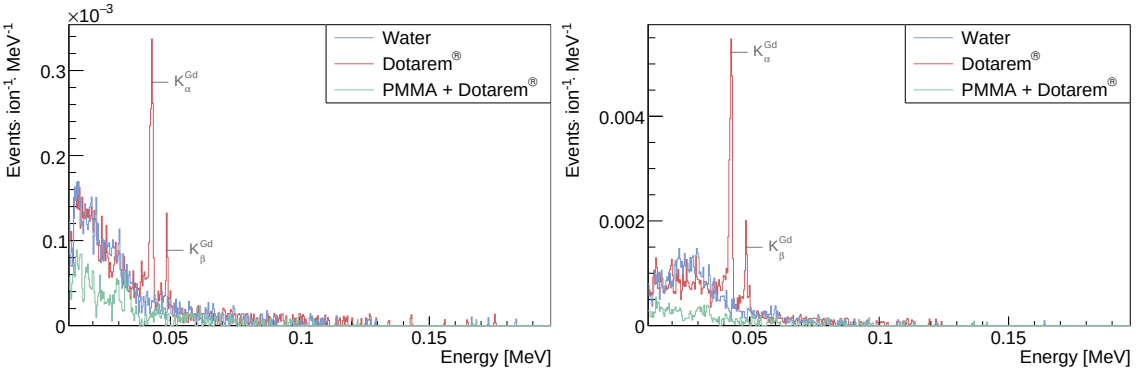

(b) Helium irradiation

(c) Carbon irradiation

Figure 5.21. Spectra measurements of a vial filled with water or Dotarem®, irradiated with (a) protons, (b) helium, and (c) carbon. The spectra were obtained using the $CdTe$ detector, including an additional configuration where 4 cm of PMMA was placed in front of the gadolinium solution.

To further address the physics behind these processes, *Monte Carlo* simulations were performed to obtain the $PIXE$ and neutron capture cross-sections for the irradiation of a GBCA thin target with a proton beam. Additionally, PMMA was included, and its thickness was varied to account for changes in the neutron capture cross-section as a function of tissue thickness. The results are presented in Figures 5.22 and 5.23.

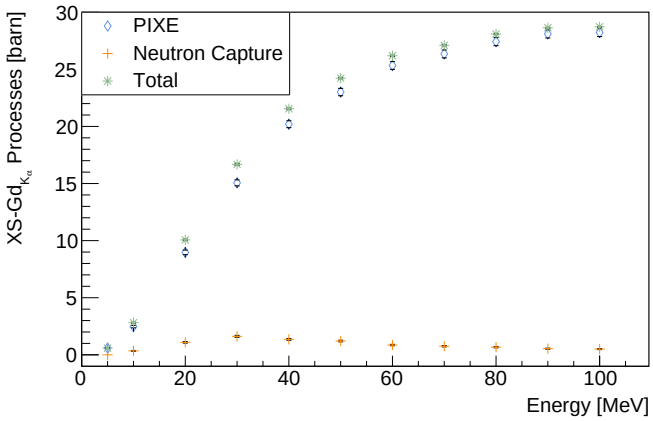

Figure 5.22. Total and individual cross-sections of neutron capture and PIXE for the emission of K_α^{Gd}.

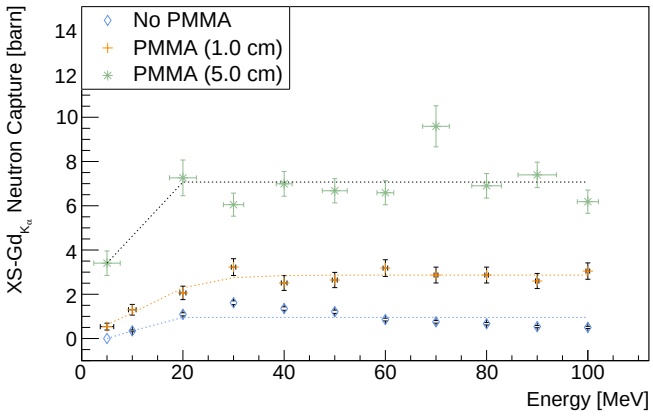

Figure 5.23. Cross-sections of neutron capture for the emission of K_α^{Gd} and different thickness of PMMA.

5.3 Dose-Dependent Spectra Variations in Gadolinium

[3] The PGS technique, with its extension to *X-ray* measurements, allows for time-resolved measurements during the delivery of a particle therapy treatment. By analyzing the microstructure of the particle beam, the spectral response of individual or grouped pencil beams can be obtained and evaluated, allowing access to the $K^{Gd}_{\alpha,\beta}$ photon emission yield from each pencil beam. Figure 5.24 shows the changes in the $K^{Gd}_{\alpha,\beta}$ yield comparatively to the changes in the dose delivered by each pencil beam to the GBCA target in the *Monte Carlo* simulation of the full treatment plan described in section 4.3.3.

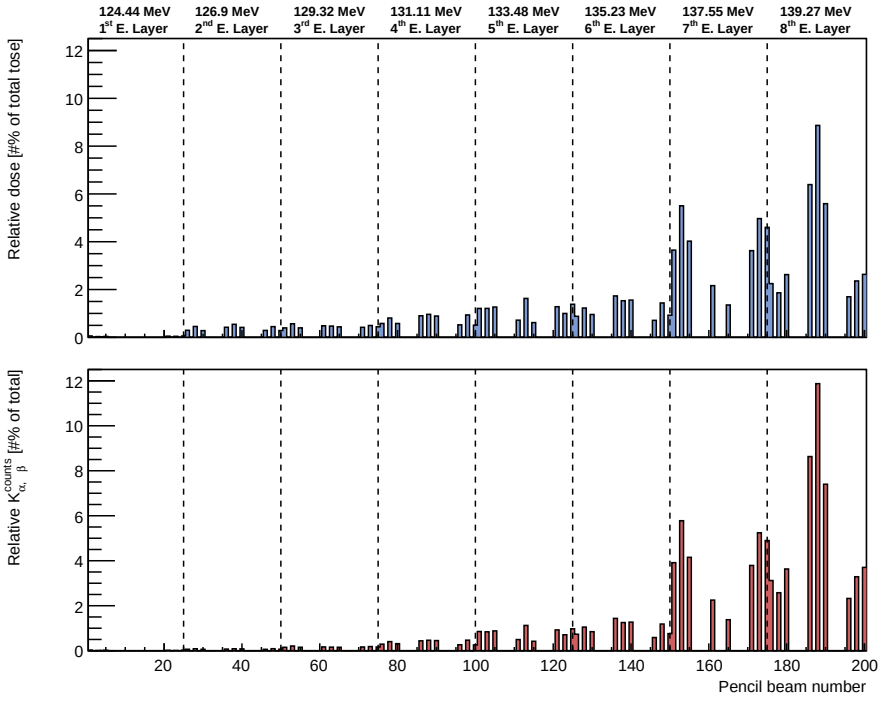

Figure 5.24. Relative dose delivered to the Gd target by single-spot proton beams in the treatment plan (top, blue bars) and the corresponding induced $K^{Gd}_{\alpha,\beta}$ yield (bottom, red bars).

The treatment plan points that most contribute to the dose coverage of the target are those from the high-energy plan, at $139.27\,\text{MeV}$ ($R_{CSDA} = 16.1\,\text{cm}$), contributing to $34\,\%$ of the prescribed dose. Conversely, the points in the plane orthogonal to the beam path with the highest contributions are the midpoints between the corners of the cubic-shaped target ($(0,1)$, $(0,-1)$, $(1,0)$ and $(-1,0)$, with units of cm) each contributing in average $11.8 \pm 0.1\,\%$ to the prescribed dose. Following these are the corner points ($(1,1)$, $(1,-1)$, $(-1,1)$, and $(-1,-1)$) and the central point ($(0,0)$), contributing $9.72 \pm 0.02\,\%$ and $14\,\%$

[3]Note: This section includes modified parts from the submitted work: Brás, M., **Freitas, H.**, Gonçalves, P., & Seco, J. (2024). In vivo dosimetry for proton therapy: A Monte Carlo study of the Gadolinium spectral response throughout the course of treatment.

to the total dose. A similar pattern is observed in the $K^{Gd}_{\alpha,\beta}$ yield of the individual pencil beams. The midpoints yield in average $11.7 \pm 0.7\,\%$ of the total emission, the corner points $9.56 \pm 0.20\,\%$ and the central point $15.0\,\%$. This shows a good agreement between the dose contributions of each pencil beam and the $K^{Gd}_{\alpha,\beta}$ photon emission yield.

Transverse Motion

The transverse displacements were analyzed by grouping the pencil beams along the beam direction (see Table 4.3 and Figure 4.13 as a reference for the subsequent analysis). Figure 5.25 relatively shows the effects that target displacements have in the dose and $K^{Gd}_{\alpha,\beta}$ yield. As the tumor shifts transversely, the dose deposition by the pencil beams changes significantly based on their position relative to the target. The significant single spot proton beams at the negative and central yz-plane (pencil beams number 1, 3, 11, 13, 21 and 23) deliver progressively less dose as the target moves out of their field, decreasing approximately $10\,\%$ for the maximum displacement. In contrast, the pencil beams at the positive yz-plane (pencil beams number 5, 15 and 25) contribute more dose as the tumor moves into their field. The variations in dose are mirrored in the $K^{Gd}_{\alpha,\beta}$ signal. This linear correlation is depicted in Figure 5.26 where variations in the dose are as a function of variations in the $K^{Gd}_{\alpha,\beta}$ signal. The relationship between dose and the $K^{Gd}_{\alpha,\beta}$ signal, considering the impact of full treatment and various transverse motions of the target, is depicted in Figure 5.27.

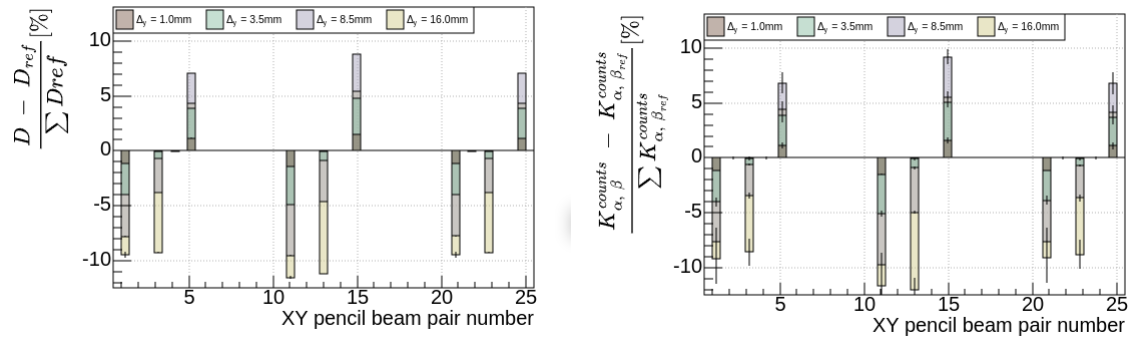

(a) Dose variations

(b) $K^{Gd}_{\alpha,\beta}$ variations

Figure 5.25. Deviations in (a) dose and (b) $K^{Gd}_{\alpha,\beta}$ yield from the standard scenario caused by transverse movements of the target.

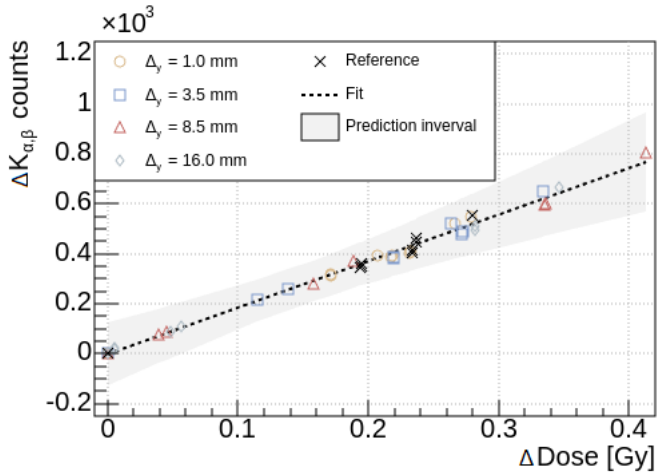

Figure 5.26. Correlation between variations in the dose delivered to the target by each pencil beam of the optimized treatment plan and variations the variations in the $K^{Gd}_{\alpha,\beta}$ yield, for various transverse tumor shifts. The linear fit (dashed, black) result in the following relation, $K^{counts}_{\alpha,\beta} = (1.90 \pm 0.02) \times 10^3\, Dose - (2 \pm 4)$

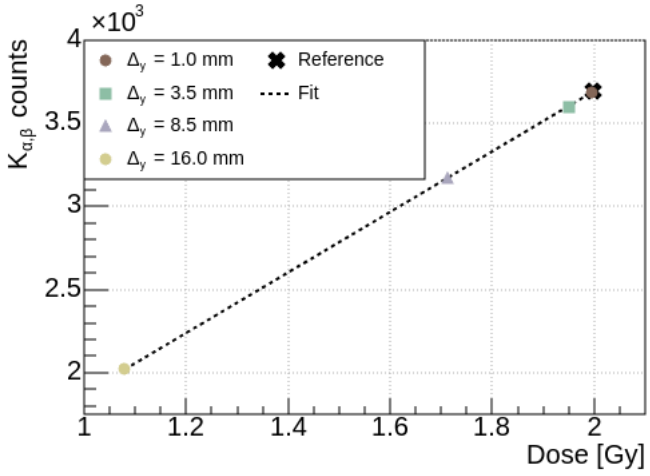

Figure 5.27. $K^{Gd}_{\alpha,\beta}$ yield as function of the total dose prescribed to the target for different transverse shifts. The linear fit (dashed, black) result in the following relation, $K^{counts}_{\alpha,\beta} = (1.82 \pm 0.01) \times 10^3\, Dose - (54 \pm 8)$.

Longitudinal Motion

Unlike the study of transverse target displacements, the impact of longitudinal shifts along the beam direction is better addressed by grouping pencil beams belonging to the same energy layer. Figure 5.28 depicts a similar analysis as the previous one. In this case, all the energy plans delivery progressively less dose to the target as it moves downstream. When the target shifts upstream, the points on the low-energy plans contribute more to overall dose deposition, while in higher energy plans the overall dose deposition decreases. Notably, the $K^{Gd}_{\alpha,\beta}$ increases with upstream shifts. This trend highlights a differing behavior between dose deposition and the $K^{Gd}_{\alpha,\beta}$ signal. The relationship between dose and the $K^{Gd}_{\alpha,\beta}$ signal, considering the impact of full treatment and various longitudinal motions of the target, is depicted in Figure 5.30.

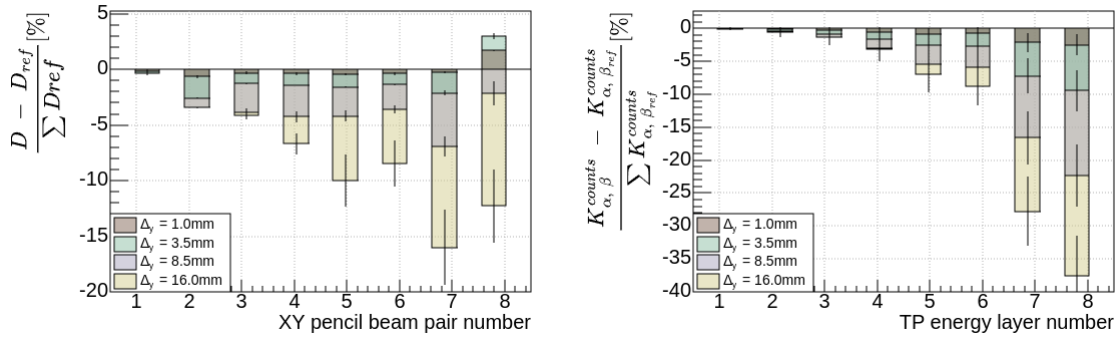

(a) Dose variations **(b)** $K^{Gd}_{\alpha,\beta}$ variations

Figure 5.28. Deviations in (a) dose and (b) $K^{Gd}_{\alpha,\beta}$ yield from the standard scenario caused by downstream movements of the target.

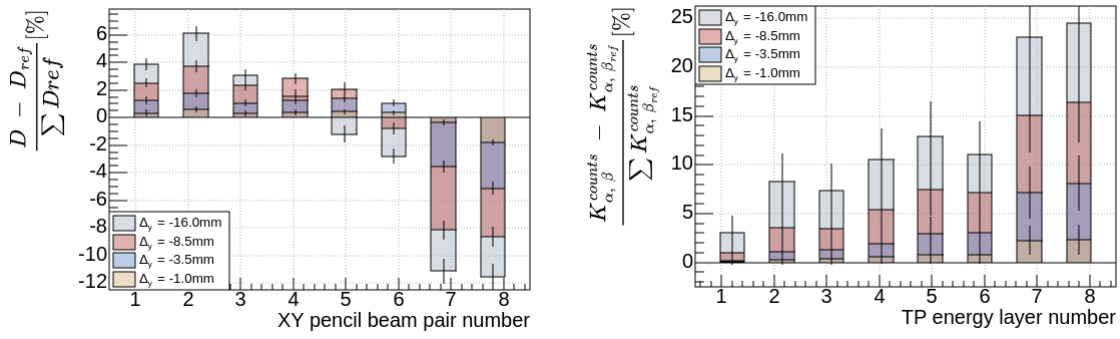

(a) Dose variations **(b)** $K^{Gd}_{\alpha,\beta}$ variations

Figure 5.29. Deviations in (a) dose and (b) $K^{Gd}_{\alpha,\beta}$ yield from the standard scenario caused by upstream movements of the target.

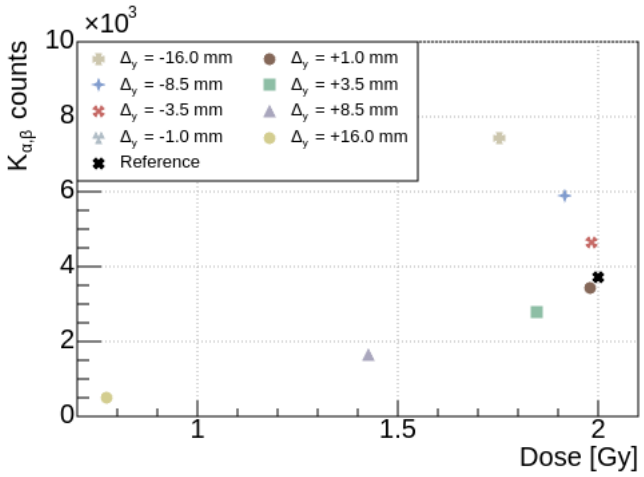

Figure 5.30. $K^{Gd}_{\alpha,\beta}$ yield as function of the total dose prescribed to the target for different shifts in the beam direction.

5.4 Range and Tumor Monitoring using Gadolinium and PGS

The treatment plan and setup of the Section 4.3.3 was used to obtain measurements of the $K^{Gd}_{\alpha,\beta}$ and ^{12}C line as a function of the depth. The accumulated results for each energy layer in Figure 4.13 are depicted in Figure 5.31.

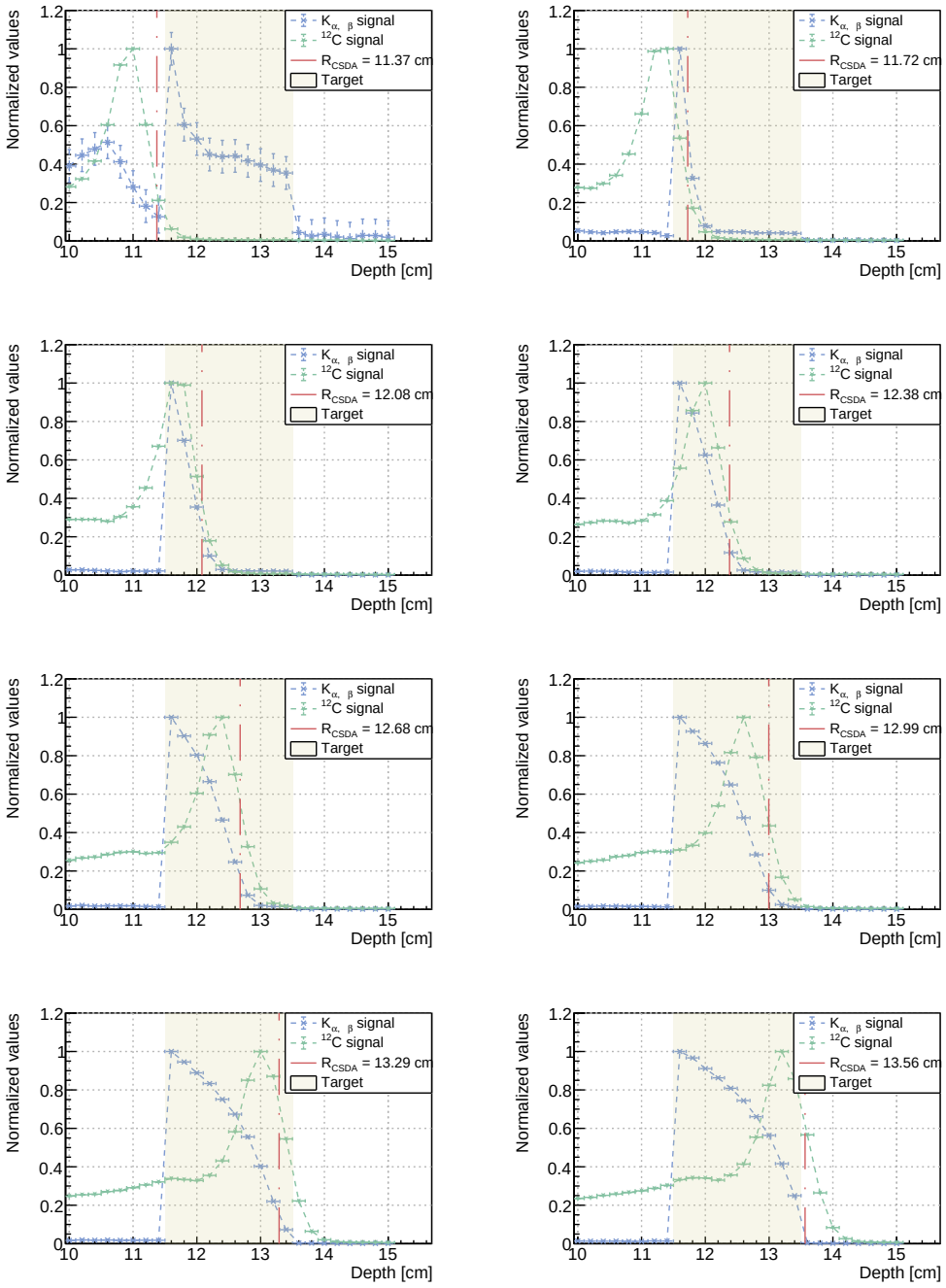

Figure 5.31. The $K^{Gd}_{\alpha,\beta}$ line (blue) and the ^{12}C line (green) are shown as a function of depth. The GBCA target and the range (red) are included for reference.

Chapter 6

Discussion

This thesis presents developmental advancements toward a novel application in prompt gamma-ray spectroscopy (PGS). The proposed application explores the potential of combining gadolinium(Gd)-based contrast agents (GBCAs) with PGS to enable real-time vivo particle monitoring. The study included a comprehensive benchmarking of PGS for proton therapy using various *Monte Carlo* simulation tools, experimental measurements of the gadolinium photon spectra response under different charged-ions irradiations, and an analysis of its spectral features across various doses and dose rates, including investigation of the underlying physics. Furthermore, the research explores the feasibility of using gadolinium as a surrogate for dose measurement and its integration with PGS for tumor and range monitoring. Therefore, this study aims to investigate the steps necessary to advance this promising PGS application toward practical implementation in clinical settings. In this chapter, the most critical findings, achievements, and limitations of the research are summarized and discussed in the following sub-sections addressing the following answers:

1. Which physics models are most suitable for use in *Monte Carlo* simulations of PGS?
2. Is using GBCAs as a surrogate for dose measurements feasible?
3. Can *in vivo* range monitoring be improved with synchronized tumor and range monitoring?
4. What are the underlying physics behind the spectral response of Gd under particle irradiation?
5. What are the theoretical limitations of this novel technique?

This study analyzed prompt gamma-ray spectra resulting from proton irradiation of a PMMA target at clinical energies. Punctual discrepancies were observed in the predicted prompt gamma-ray emissions simulated by `MCNP6`, `GEANT4`, and `FLUKA` when compared with

experimental data. To address this issue, a new GEANT4 model (EMPIRICAL) was developed using experimental and theoretical data from the literature.

In the context of PGS analysis, the most prominent low-energy prompt gamma-ray lines ($< 1.5MeV$) are the ^{10}B lines, reproduced only by GEANT4 (see Figure 5.6). Discrepancies in the EMPIRICAL model and others emerged from limited experimental data in this range (Kozlovsky et al. [2002]). However, experimental data for proton inelastic interactions with carbon have recently become available in the literature (Hosobuchi et al. [2023], Rahma et al. [2023]), providing valuable insights. For energies between 1.5 and 3.0 MeV, key de-excitation lines include ^{14}N, ^{11}C, and 2.223 MeV gamma-rays from neutron capture of ^{1}H. However, analyzing these lines in Figure 5.8 and 5.7 (left) is challenging due to significant contributions from competing reactions. The EMPIRICAL model and FLUKA perform better in this energy range, following the trends and magnitudes observed in the experimental data. At higher energies, the $^{12}C^{*}_{4.439\,\mathrm{MeV}} \rightarrow {}^{12}C_{g.s.}$ and $^{16}O^{*}_{6.130\,\mathrm{MeV}} \rightarrow {}^{16}O_{g.s.}$ lines are the most relevant. Results for the ^{12}C line, shown in Figure 5.7 (right), revealed some discrepancies. While FLUKA and GEANT4 reproduce their behavior, MCNP6 best matches the experimental magnitude. FLUKA tends to overestimate the line, whereas GEANT4 underestimates it by a factor of approximately 2, consistent with findings from previous studies (Schumann et al. [2015], Verburg et al. [2013]). While not accurately predicting the magnitude of the ^{12}C line, the EMPIRICAL model aligns well with experimental trends. For instance, compared to the experimental value of $(8.22 \pm 0.15) \times 10^{-8}$ events MeV^{-1}, the EMPIRICAL model's estimate of $(8.63 \pm 0.71) \times 10^{-8}$ events MeV^{-1} demonstrates reasonable agreement. Most *Monte Carlo* codes poorly reproduce the ^{16}O prompt gamma-ray line, but using the EMPIRICAL model significantly improved accuracy, bringing results closer to expected values for the beam energies studied (see Figure 2.8).

Across the different *Monte Carlo* toolkits, the inelastic cross-sections for proton interactions with ^{12}C and ^{16}O align well with experimental data (Verburg et al. [2012]). These processes rely on distinct physical models, influencing the prompt gamma-ray emission stage, which varies across toolkits. In MCNP6, prompt gamma-ray emission is more isotropic, closely matching experimental observations, contributing to its superior performance for the ^{12}C de-excitation line compared to the forward-biased prompt gamma-ray emission in GEANT4 (Kiener et al. [1998], Styczynski [2009]). Conversely, FLUKA and GEANT4 incorporate more advanced and adaptable nuclear de-excitation and photon-evaporation models (Agostinelli et al. [2003], Allison et al. [2006, 2016], Böhlen et al. [2014], Ferrari et al. [2005]). However, MCNP6, being library-dependent, lacks the customization of other toolkits, and its nuclear data tables' limited energy resolution constrains their application in simulations. For the photo-evaporation process, particularly the gamma-ray cascade in ^{16}O, the primary transition is an $E3$ transition emitting a 6.13 MeV photon (see Figure 2.5), as

the $E0$ transition (6.05 MeV) is forbidden for transitions between spin-zero states, decaying only via internal conversion (Kibédi et al. [2022], Zganjar and Wood [1995]). However, `GEANT4` prominently displays the $E0$ transition in its PG spectra. These discrepancies underscore the need for ongoing refinement of toolkit models. While empirical approaches, like the `EMPIRICAL` method, partially address these issues, further advancements in physical modeling are essential to enhance the predictive accuracy of ^{16}O PG emission simulations in proton therapy.

The future of real-time adaptation treatments relies on information not only about the beam's range but also about the target mapping. For example, recent research focuses on implementing image-guided systems in particle therapy treatment rooms (OncoRay [2024]). In this regard, gadolinium is crucial as it provides a *X-ray* signal that facilitates this process. This signal enables precise target positioning mapping, while PGS can offer range measurements and valuable feedback for real-time treatment adjustments. Figure 5.31 shows that tumor localization is still possible even for beams that undershoot the target.

The potential of gadolinium, or its form as a contrast agent, to serve as a surrogate for dose measurements in particle therapy is grounded in features presented in this study. When irradiated with charged ions, secondary induced radiation is emitted and can be detected in real-time using an external photon detector. Upon analysis of such radiation, a noticeable peak emerges when comparing the response of a GBCA solution to that of a tissue-like material, such as water. This peak appears within the energy range of the electron shell transitions and is better identified as the characteristic *X-ray* emission of Gd. Compared to prompt gamma-ray emission, the line presented in Figures 5.10, 5.12 and 5.14 exhibits a magnitude two orders higher. From the previous results, one can hypothesize using the Gd peak yield to extract information throughout the course of a particle treatment. Figure 5.16 presents the first preliminary studies supporting this application. A linear dependence on dose was observed as an essential attribute of an effective dose-monitoring detector. Such a detector must reliably measure dose across varying beam intensities or dose rates. This capability become even more critical with the growing interest in ultra-high dose rates, mainly due to recent discoveries about the FLASH effect. Interestingly, many detectors typically used in conventional radiotherapy underperform under these conditions.

The results shown in Figure 5.17 demonstrated a small dose dependence of the PGS system. However, this was attributed to limitations associated with using an over-dimensional $CeBr3$ inorganic scintillator unsuitable for energy measurements in the keV range. To address this, a more suitable detector, such as a $CdTe$ detector, was used alongside the $CeBr_3$ detector to analyze changes in the Gd signal for different ions. The $CdTe$ detector outperformed the $CeBr3$ in terms of resolution, although its efficiency was lower mainly due to its reduced size. Both carbon and helium ions show increased cross section for the Gd signal.

This was expected, as the primary physical process identified during the measurements was PIXE, scaling quadratically with the effective charge of the ion (Bakr et al. [2022]).

To correlate the Gd signal with the dose, the next logical step was to understand how its cross-section changes with proton energy in GBCA. For a thin target, neutron capture processes are almost negligible when compared to PIXE. This result aligns with initial expectations, as the production of neutrons is significantly low in a thin-target environment. However, in particle therapy, tumor depths can range from a few millimeters to depths of 20 cm or more, depending on their location. This variation in depth is a crucial factor to consider when using this technique. Simulating the tissue effect showed that neutron capture processes start to be significant at 5 cm deep. Analyzing these results, distinct cross-section behaviors are observed depending on the physical process involved. The neutron capture cross section remains approximately constant above ≈ 30 MeV while Gd PIXE cross section plateau is at ≈ 90 MeV (depths greater than 5 cm).

Towards clinical applicability, this technique was studied over the course of a *Monte Carlo* simulated treatment plan. Figure 5.24 shows how the induced photon secondary spectra would change for single-spot beams in a treatment plan. A more statistically robust approach is spot merging to improve data quality (Kim et al. [2019]). The use of this technique allows the tracking of patient geometry changes through variations in the Gd signal. For transverse motions, changes in dose delivered correlate directly with changes in the Gd signal (see Figure 5.25). Meanwhile, longitudinal shifts impact proton energy and range, reducing doses and signals for distal movements. Conversely, upstream shifts increase the Gd signal due to higher proton energy and an enhanced PIXE cross-section, even though the deposited dose may decrease (see Figure 5.30).

The dose-dependent spectra results show that the sensitivity of PIXE to particle energy is essential, as the energy deposited will significantly influence the Gd signal. This implies that the relationship between the Gd signal and the absorbed dose is not linear. A constant cross-section would be preferable for achieving more precise dose measurements. To address this challenge, one should determine the residual range of the proton or construct the Gd signal based on the type of physical interaction from which it originated. The former can be effectively achieved using PGS as a complementary technique. The latter challenge, distinguishing processes by time-resolving technique, is plausible given that neutrons are generally slower than time-resolved measurements, which can differentiate protons and secondary thermal neutron-induced interactions.

Finally, it is crucial to consider factors such as the concentration of Gd in the tumor, geometrical aspects like the source-detector distance, and photon attenuation in tissue. The concentration of Gd can be addressed using imaging techniques such as MRI. Specifically, quantitative MRI analysis, correlating T1 times with Gd concentrations, or PGS, could be

used to retrieve this information during the treatment. Photon attenuation is another critical factor, as Gd emits low-energy photons that are highly susceptible to attenuation depending on the amount of tissue between the tumor and the detector. Emerging techniques such as FLASH therapy could enhance the applicability of this approach. The high doses used in these methods may produce a sufficiently strong signal for detection, even after accounting for tissue attenuation. Specifically, in the case of FLASH therapy, this technique could address the limitations posed by the extremely high dose rates, where conventional dosimetry tools underperform.

Chapter 7

Conclusion

This study highlights the potential of integrating gadolinium-based contrast agents (GBCAs) with prompt gamma-ray spectroscopy (PGS) for real-time, *in vivo* particle therapy monitoring. The findings support the feasibility of this technique for dose measurement, range verification, and tumor localization.

In summary, the benchmarking of *Monte Carlo* tools revealed specific discrepancies for relevant de-excitation lines, particularly those associated with carbon and oxygen. Additionally, we applied a new model based on experimental and theoretical cross sections, which improved the reproduction of the oxygen de-excitation line. Then, irradiation of GBCA resulted in new findings related to the underlying physics of the most prominent Gd emission photon, the characteristic *X-ray* photon. Previous understanding and applications of this emission focused on the neutron capture by Gd. However, this study demonstrated that particle-induced *X-Ray* emission is the primary contributing process in the low and intermediary energies range. These findings underscore the importance of considering both physical processes for effective monitoring in clinical scenarios, particularly in deeper tumors. Spectral measurements across different ions hint at carbon therapy is the modality that would take more advantage of this technique. The ability to distinguish transverse and longitudinal motion through variations in the Gd signal demonstrates the robustness of this approach for real-time treatment adaptation.

Challenges such as photon attenuation, the non-linear relationship between the Gd signal and absorbed dose, and the need for time-resolved techniques to differentiate interactions were addressed. The study also mentions the potential of using imaging modalities like MRI for Gd concentration quantification and integrating PGS with novel techniques such as FLASH therapy to overcome the limitations of conventional dosimetry at high dose rates.

In conclusion, this research provides a strong foundation for advancing PGS combined with Gd for real-time vivo particle therapy monitoring. Future work should focus on refining simulation models, improving detector technology, and expanding experimental valida-

tion to facilitate clinical implementation and further improve the precision and efficacy of particle therapy.

Scientific Publications

Publications

*__Freitas, H.__, Nobakht, E., Grüner, F., & Seco, J. (2024). A Comparative Analysis of GEANT4, MCNP6, and FLUKA on Proton-Induced Gamma-Ray Simulation.

*Brás, M., __Freitas, H.__, Gonçalves, P., & Seco, J. (2024). In vivo dosimetry for proton therapy: A Monte Carlo study of the Gadolinium spectral response throughout the course of treatment.

*Submitted for publication (accepted under the condition of a minor revision).

Books

**Chapter "Imaging for Daily Range Monitoring of Treatment Beam," authored by Pryanichnikov, A.A., __Freitas, H.__, Parodi, K., and Volz, L., in the book "Introduction to Particle Therapy: An Educational Handbook" (Foka, Y., Vretenar, M., & Seco, J., eds.).

**Expected publication in 2025.

Conferences

__Freitas, H.__, Brás M., Nobahkt E., Grafe, J.L., Seco, J. (2024). Simultaneously Achieving Range Monitoring and Tumor Localization with Prompt Gamma-Ray Spectroscopy and Gadolinium-Based Contrast Agents. AAPM 66th Annual Meeting & Exhibition.

__Freitas, H.__, Cruzeiro, B., Brás, M., Correia, P., Seco, J. (2024). In-vivo dose measurements in proton therapy with PGS and Gadolinium-based contrast agents: A comparative analysis with MRI for GD detection. European Congress of Medical Physics.

Brás, M., **Freitas, H.**, Gonçalves, P., Seco, J. (2024). In vivo dosimetry for proton therapy: A Monte Carlo study of gadolinium as a surrogate for dose measurements. PTCOG 62;

Brás, M., **Freitas, H.**, Baumann, K., Gonçalves, P., Seco, J. (2024), In vivo range verification and treatment plan tracking in sync with tumor localization using a gadolinium-based contrast agent as a surrogate. European congress of medical physics.

Freitas, H., Brás, M., Brons, S., Gonçalves, P., Seco, J. (2022), Flash Dosimetry Using Prompt Gamma-X Spectroscopy During Proton Irradiation of GD-Based Contrast Agent, FRPT2022.

Bibliography

Sea Agostinelli, John Allison, K al Amako, John Apostolakis, H Araujo, Pedro Arce, Makoto Asai, D Axen, Swagato Banerjee, GJNI Barrand, et al. Geant4—a simulation toolkit. *Nuclear instruments and methods in physics research section A: Accelerators, Spectrometers, Detectors and Associated Equipment*, 506(3):250–303, 2003.

Steven P Ahlen. Theoretical and experimental aspects of the energy loss of relativistic heavily ionizing particles. *Reviews of Modern Physics*, 52(1):121, 1980.

John Allison, Katsuya Amako, JEA Apostolakis, HAAH Araujo, P Arce Dubois, MAAM Asai, GABG Barrand, RACR Capra, SACS Chauvie, RACR Chytracek, et al. Geant4 developments and applications. *IEEE Transactions on nuclear science*, 53(1):270–278, 2006.

John Allison, Katsuya Amako, John Apostolakis, Pedro Arce, Makoto Asai, Tsukasa Aso, Enrico Bagli, A Bagulya, S Banerjee, GJNI Barrand, et al. Recent developments in geant4. *Nuclear instruments and methods in physics research section A: Accelerators, Spectrometers, Detectors and Associated Equipment*, 835:186–225, 2016.

Inc Amptek. Xr-100cdte user manual user operating manual xr-100cdte x-ray detector & preamplifier. Datasheet, 2017.

Jake Atkinson, Eva Bezak, Hien Le, and Ivan Kempson. The current status of flash particle therapy: a systematic review. *Physical and Engineering Sciences in Medicine*, 46(2): 529–560, 2023.

Frank Herbert Attix. *Introduction to radiological physics and radiation dosimetry*. John Wiley & Sons, 2008.

Samer Bakr, David D Cohen, Rainer Siegele, Sebastien Incerti, V Ivanchenko, A Mantero, A Rosenfeld, and Susanna Guatelli. Latest geant4 developments for pixe applications. *Nuclear Instruments and Methods in Physics Research Section B: Beam Interactions with Materials and Atoms*, 436:285–291, 2018.

Samer Bakr, David D Cohen, Rainer Siegele, Sebastien Incerti, Vladimir Ivanchenko, Alfonso Mantero, Anatoly Rosenfeld, and Susanna Guatelli. Validation of the geant4 pixe component for incident carbon ions. *Nuclear Instruments and Methods in Physics Research Section B: Beam Interactions with Materials and Atoms*, 532:38–46, 2022.

Jean-Louis Basdevant, James Rich, and Michael Spiro. *Fundamentals in nuclear physics: From nuclear structure to cosmology*. Springer Science & Business Media, 2005.

W Bauhoff. Tables of reaction and total cross sections for proton-nucleus scattering below 1 gev. *Atomic Data and Nuclear Data Tables*, 35(3):429–447, 1986.

A Belhout, J Kiener, A Coc, J Duprat, C Engrand, Caroline Fitoussi, M Gounelle, A Lefebvre-Schuhl, N de Séréville, V Tatischeff, et al. γ-ray production by proton and α-particle induced reactions on c 12, o 16, mg 24, and fe. *Physical Review C—Nuclear Physics*, 76(3):034607, 2007.

Hans Bethe. Zur theorie des durchgangs schneller korpuskularstrahlen durch materie. *Annalen der Physik*, 397(3):325–400, 1930.

Maria Giuseppina Bisogni, Andrea Attili, Giuseppe Battistoni, Nicola Belcari, Niccolo' Camarlinghi, Piergiorgio Cerello, Silvia Coli, Alberto Del Guerra, Alfredo Ferrari, Veronica Ferrero, et al. Inside in-beam positron emission tomography system for particle range monitoring in hadrontherapy. *Journal of medical imaging*, 4(1):011005–011005, 2017.

Felix Bloch. Zur bremsung rasch bewegter teilchen beim durchgang durch materie. *Annalen der Physik*, 408(3):285–320, 1933.

TT Böhlen, Francesco Cerutti, MPW Chin, Alberto Fassò, Alfredo Ferrari, P Garcia Ortega, Andrea Mairani, Paola R Sala, George Smirnov, and Vasilis Vlachoudis. The fluka code: developments and challenges for high energy and medical applications. *Nuclear data sheets*, 120:211–214, 2014.

Niels Bohr. On the decrease of velocity of swiftly moving electrified particles in passing through matter. *The London, Edinburgh, and Dublin Philosophical Magazine and Journal of Science*, 30(178):581–612, 1915.

M Boromiza, C Borcea, P Dessagne, D Ghita, T Glodariu, G Henning, M Kerveno, N Marginean, C Mihai, R Mihai, et al. Nucleon inelastic scattering cross sections on o 16 and si 28. *Physical Review C*, 101(2):024604, 2020.

Thomas Bortfeld, Harald Paganetti, and H Kooy. Mo-a-t-6b-01: proton beam radiotherapy—the state of the art. *Medical Physics*, 32(6Part13):2048–2049, 2005.

Saverio Braccini. Compact medical cyclotrons and their use for radioisotope production and multi-disciplinary research. *Hospital*, 200(250):10–13, 2017.

William Henry Bragg and Richard Kleeman's. On the α particles of radium, and their loss of range in passing through various atoms and molecules. *The London, Edinburgh, and Dublin Philosophical Magazine and Journal of Science*, 10(57):318–340, 1905.

Rene Brun and Fons Rademakers. Root—an object oriented data analysis framework. *Nuclear instruments and methods in physics research section A: accelerators, spectrometers, detectors and associated equipment*, 389(1-2):81–86, 1997.

Caterina Cuccagna, Giuseppe Battistoni, Maria Giuseppina Bisogni, Piergiorgio Cerello, Alberto Del Guerra, Veronica Ferrero, Elisa Fiorina, Matteo Morrocchi, Francesco Pennazio, Roberto Sacchi, et al. Few-seconds range verification with short-lived positron emitters in carbon ion therapy. *Physica Medica*, 118:103209, 2024.

Riccardo Dal Bello. *Nuclear prompt gamma spectroscopy for range verification in ion-beam therapy*. PhD thesis, Heidelberg University, 2020.

Riccardo Dal Bello, Paulo Magalhaes Martins, João Graça, German Hermann, Thomas Kihm, and Joao Seco. Results from the experimental evaluation of cebr scintillators for he prompt gamma spectroscopy. *Medical physics*, 46(8):3615–3626, 2019.

Riccardo Dal Bello, Paulo Magalhaes Martins, Stephan Brons, German Hermann, Thomas Kihm, Michael Seimetz, and Joao Seco. Prompt gamma spectroscopy for absolute range verification of 12c ions at synchrotron-based facilities. *Physics in Medicine & Biology*, 65(9):095010, 2020.

E Draeger, D Mackin, S Peterson, H Chen, S Avery, S Beddar, and JC Polf. 3d prompt gamma imaging for proton beam range verification. *Physics in Medicine & Biology*, 63 (3):035019, 2018.

P. Dyer, D. Bodansky, A.G. Seamster, E.B. Norman, and D.R. Maxson. Cross sections relevant to gamma-ray astronomy: Proton induced reactions. *Physical Review C*, 23(5): 1865, 1981.

Alfredo Ferrari, Paola R Sala, Alberto Fasso, and Johannes Ranft. Fluka. *CERN-library in: http://fluka. web. cern. ch/fluka*, 55(99):100, 2005.

Veronica Ferrero, Elisa Fiorina, Matteo Morrocchi, Francesco Pennazio, Guido Baroni, Giuseppe Battistoni, Nicola Belcari, Niccolo' Camarlinghi, Mario Ciocca, Alberto Del Guerra, et al. Online proton therapy monitoring: clinical test of a silicon-photodetector-based in-beam pet. *Scientific reports*, 8(1):4100, 2018.

Beatrice Foglia, Chiara Gianoli, Takamitsu Masuda, Elisabetta De Bernardi, Thomas R Bortfeld, Katia Parodi, and Marco Pinto. Prompt gamma-based dose reconstruction strategies in proton therapy. In *AAPM 66th Annual Meeting & Exhibition*. AAPM, 2024.

KJ Foley, GL Salmon, and AB Clegg. Gamma radiation from the bombardment of 16o and 19f nuclei with 150 mev protons. *Nuclear Physics*, 31:43–52, 1962.

Tyler J Fraum, Daniel R Ludwig, Mustafa R Bashir, and Kathryn J Fowler. Gadolinium-based contrast agents: a comprehensive risk assessment. *Journal of Magnetic Resonance Imaging*, 46(2):338–353, 2017.

Hugo Freitas, Paulo Magalhaes Martins, Thomas Tessonnier, Benjamin Ackermann, Stephan Brons, and Joao Seco. Dataset for predicting single-spot proton ranges in proton therapy of prostate cancer. *Scientific data*, 8(1):252, 2021.

Panagiota Galanakou, Theodora Leventouri, and Wazir Muhammad. Non-radioactive elements for prompt gamma enhancement in proton therapy. *Radiation Physics and Chemistry*, 196:110132, 2022.

Shanmin Gao, Rongrong Fu, and Narayan S Hosmane. Nanomaterials for boron and gadolinium neutron capture therapy for cancer treatment. *Pure and Applied Chemistry*, 87(2):123–134, 2015.

Christian Golnik, Fernando Hueso-González, Andreas Müller, Peter Dendooven, Wolfgang Enghardt, Fine Fiedler, Thomas Kormoll, Katja Roemer, Johannes Petzoldt, Andreas Wagner, et al. Range assessment in particle therapy based on prompt γ-ray timing measurements. *Physics in Medicine & Biology*, 59(18):5399, 2014.

JL Gräfe, FE McNeill, SH Byun, DR Chettle, and MD Noseworthy. A benchmarked mcnp model of the in vivo detection of gadolinium by prompt gamma neutron activation analysis. *Nuclear Instruments and Methods in Physics Research Section B: Beam Interactions with Materials and Atoms*, 268(15):2451–2457, 2010.

JL Gräfe, FE McNeill, SH Byun, DR Chettle, and MD Noseworthy. The feasibility of in vivo detection of gadolinium by prompt gamma neutron activation analysis following gadolinium-based contrast-enhanced mri. *Applied Radiation and Isotopes*, 69(1):105–111, 2011.

JL Gräfe, FE McNeill, MD Noseworthy, and DR Chettle. Gadolinium detection via in vivo prompt gamma neutron activation analysis following gadolinium-based contrast agent injection: a pilot study in 10 human participants. *Physiological measurement*, 35(9): 1861, 2014.

S Greilich. *Tools to Measure and Improve the Microscopic Energy Deposition in Ion Beam Therapy*. PhD thesis, Habilitation Thesis Heidelberg University, 2017.

Th Haberer, W Becher, Dieter Schardt, and Gerhard Kraft. Magnetic scanning system for heavy ion therapy. *Nuclear Instruments and Methods in Physics Research Section A: Accelerators, Spectrometers, Detectors and Associated Equipment*, 330(1-2):296–305, 1993.

Th Haberer, Jürgen Debus, H Eickhoff, Oliver Jäkel, Daniela Schulz-Ertner, and Uli Weber. The heidelberg ion therapy center. *Radiotherapy and Oncology*, 73:S186–S190, 2004.

Josefine Handrack, Thomas Tessonnier, Wenjing Chen, Jakob Liebl, Jürgen Debus, Julia Bauer, and Katia Parodi. Sensitivity of post treatment positron emission tomography/computed tomography to detect inter-fractional range variations in scanned ion beam therapy. *Acta Oncologica*, 56(11):1451–1458, 2017.

Charles R. Harris, K. Jarrod Millman, Stéfan J. van der Walt, Ralf Gommers, Pauli Virtanen, David Cournapeau, Eric Wieser, Julian Taylor, Sebastian Berg, Nathaniel J. Smith, Robert Kern, Matti Picus, Stephan Hoyer, Marten H. van Kerkwijk, Matthew Brett, Allan Haldane, Jaime Fernández del Río, Mark Wiebe, Pearu Peterson, Pierre Gérard-Marchant, Kevin Sheppard, Tyler Reddy, Warren Weckesser, Hameer Abbasi, Christoph Gohlke, and Travis E. Oliphant. Array programming with NumPy. *Nature*, 585(7825):357–362, September 2020.

Yoshinori Hayakawa, Junichiro Tada, Norio Arai, Katsuhisa Hosono, Masaru Sato, Toshio Wagai, Hiroshi Tsuji, and Hirohiko Tsujii. Acoustic pulse generated in a patient during treatment by pulsed proton radiation beam. *Radiation Oncology Investigations*, 3(1): 42–45, 1995.

Mana Hosobuchi, Jun Kataoka, Fumiya Nishi, Ryo Tanaka, and Taku Inaniwa. Demonstrative measurement of proton-nuclear reaction by deconvolving the prompt gamma-ray spectra. *Nuclear Instruments and Methods in Physics Research Section A: Accelerators, Spectrometers, Detectors and Associated Equipment*, 1046:167659, 2023.

Fernando Hueso-González and Thomas Bortfeld. Compact method for proton range verification based on coaxial prompt gamma-ray monitoring: A theoretical study. *IEEE transactions on radiation and plasma medical sciences*, 4(2):170–183, 2019.

Fernando Hueso-González, Wolfgang Enghardt, Fine Fiedler, Christian Golnik, Guillaume Janssens, Johannes Petzoldt, Damien Prieels, Marlen Priegnitz, Katja E Römer, Julien Smeets, et al. First test of the prompt gamma ray timing method with heterogeneous

targets at a clinical proton therapy facility. *Physics in Medicine & Biology*, 60(16):6247, 2015.

Fernando Hueso-González, Moritz Rabe, Thomas A Ruggieri, Thomas Bortfeld, and Joost M Verburg. A full-scale clinical prototype for proton range verification using prompt gamma-ray spectroscopy. *Physics in Medicine & Biology*, 63(18):185019, 2018.

Nora Hünemohr, Bernhard Krauss, Christoph Tremmel, Benjamin Ackermann, Oliver Jäkel, and Steffen Greilich. Experimental verification of ion stopping power prediction from dual energy ct data in tissue surrogates. *Physics in Medicine & Biology*, 59(1):83, 2013.

Oliver Jäkel, Gerhard Kraft, and Christian P Karger. The history of ion beam therapy in germany. *Zeitschrift für medizinische Physik*, 32(1):6–22, 2022.

Kevin C Jones, François Vander Stappen, Christopher R Bawiec, Guillaume Janssens, Peter A Lewin, Damien Prieels, Timothy D Solberg, Chandra M Sehgal, and Stephen Avery. Experimental observation of acoustic emissions generated by a pulsed proton beam from a hospital-based clinical cyclotron. *Medical physics*, 42(12):7090–7097, 2015.

Yuri Kalambet, Yuri Kozmin, Ksenia Mikhailova, Igor Nagaev, and Pavel Tikhonov. Reconstruction of chromatographic peaks using the exponentially modified gaussian function. *Journal of Chemometrics*, 25(7):352–356, 2011.

Stephan Kellnberger, Walter Assmann, Sebastian Lehrack, Sabine Reinhardt, Peter Thirolf, Daniel Queirós, George Sergiadis, Günther Dollinger, Katia Parodi, and Vasilis Ntziachristos. Ionoacoustic tomography of the proton bragg peak in combination with ultrasound and optoacoustic imaging. *Scientific reports*, 6(1):29305, 2016.

Tibor Kibédi, AB Garnsworthy, and JL Wood. Electric monopole transitions in nuclei. *Progress in Particle and Nuclear Physics*, 123:103930, 2022.

J Kiener, M Berheide, NL Achouri, A Boughrara, A Coc, A Lefebvre, Francois de Oliveira Santos, and Ch Vieu. γ-ray production by inelastic proton scattering on 16 o and 12 c. *Physical Review C*, 58(4):2174, 1998.

Sung Hun Kim, Jong Hoon Park, Youngmo Ku, Hyun Su Lee, Young-su Kim, Chan Hyeong Kim, and Jong Hwi Jeong. Improvement of statistics in proton beam range measurement by merging prompt gamma distributions: a preliminary study. *Journal of Radiation Protection and Research*, 44(1):1–7, 2019.

Glenn F Knoll. *Radiation detection and measurement*. John Wiley & Sons, 2010.

Antje-Christin Knopf and Antony Lomax. In vivo proton range verification: a review. *Physics in Medicine & Biology*, 58(15):R131, 2013.

AM Koehler. Proton radiography. *Science*, 160(3825):303–304, 1968.

Benzion Kozlovsky, Ronald J. Murphy, and Reuven Ramaty. Nuclear deexcitation gamma-ray lines from accelerated particle interactions. *The Astrophysical Journal Supplement Series*, 141(2):523, 2002.

Aafke Christine Kraan. Range verification methods in particle therapy: underlying physics and monte carlo modeling. *Frontiers in oncology*, 5:150, 2015.

Dieter Kraft. A software package for sequential quadratic programming. *Forschungsbericht- Deutsche Forschungs- und Versuchsanstalt fur Luft- und Raumfahrt*, 1988.

J Krimmer, G Angellier, L Balleyguier, D Dauvergne, N Freud, J Hérault, Jean Michel Létang, H Mathez, M Pinto, E Testa, et al. A cost-effective monitoring technique in particle therapy via uncollimated prompt gamma peak integration. *Applied Physics Letters*, 110 (15), 2017.

J Krimmer, D Dauvergne, JM Létang, and És Testa. Prompt-gamma monitoring in hadrontherapy: A review. *Nuclear Instruments and Methods in Physics Research Section A: Accelerators, Spectrometers, Detectors and Associated Equipment*, 878:58–73, 2018.

Florian Kroll, Florian-Emanuel Brack, Constantin Bernert, Stefan Bock, Elisabeth Bodenstein, Kerstin Brüchner, Thomas E Cowan, Lennart Gaus, René Gebhardt, Uwe Helbig, et al. Tumour irradiation in mice with a laser-accelerated proton beam. *Nature Physics*, 18(3):316–322, 2022.

Gerald J Kutcher, Lawrence Coia, Michael Gillin, William F Hanson, Steven Leibel, Robert J Morton, Jatinder R Palta, James A Purdy, Lawrence E Reinstein, Goran K Svensson, et al. Comprehensive qa for radiation oncology: report of aapm radiation therapy committee task group 40. *MEDICAL PHYSICS-LANCASTER PA-*, 21:581–581, 1994.

FL Lang, CW Werntz, CJ Crannell, JI Trombka, and CC Chang. Cross sections for production of the 15.10-mev and other astrophysically significant gamma-ray lines through excitation and spallation of c 12 and o 16 with protons. *Physical Review C*, 35(4):1214, 1987.

Ernest O Lawrence and M Stanley Livingston. The production of high speed light ions without the use of high voltages. *Physical Review*, 40(1):19, 1932.

Sebastian Lehrack, Walter Assmann, Damien Bertrand, Sebastien Henrotin, Joel Herault, Vincent Heymans, Francois Vander Stappen, Peter G Thirolf, Marie Vidal, Jarno Van de Walle, et al. Submillimeter ionoacoustic range determination for protons in water at a clinical synchrocyclotron. *Physics in Medicine & Biology*, 62(17):L20, 2017.

K.T. Lesko, E.B. Norman, R.-M. Larimer, S. Kuhn, D.M. Meekhof, S.G. Crane, and H.G. Bussell. Measurements of cross sections relevant to γ-ray line astronomy. *Physical Review C*, 37(5):1808, 1988.

HW Lewis. Range straggling of a nonrelativistic charged particle. *Physical Review*, 85(1): 20, 1952.

Charles L Limoli and Marie-Catherine Vozenin. Reinventing radiobiology in the light of flash radiotherapy. *Annual Review of Cancer Biology*, 7(1):1–21, 2023.

Paulo Magalhaes Martins, Riccardo Dal Bello, Benjamin Ackermann, Stephan Brons, German Hermann, Thomas Kihm, and Joao Seco. Pibs: Proton and ion beam spectroscopy for in vivo measurements of oxygen, carbon, and calcium concentrations in the human body. *Scientific reports*, 10(1):7007, 2020a.

Paulo Magalhaes Martins, Riccardo Dal Bello, Michael Seimetz, German Hermann, Thomas Kihm, and Joao Seco. A single-particle trigger for time-of-flight measurements in prompt-gamma imaging. *Frontiers in Physics*, 8:169, 2020b.

Paulo Magalhaes Martins, Hugo Freitas, Thomas Tessonnier, Benjamin Ackermann, Stephan Brons, and Joao Seco. Towards real-time pgs range monitoring in proton therapy of prostate cancer. *Scientific reports*, 11(1):15331, 2021.

Faisal Mahmood, Ulla Gro Nielsen, Christian Brandt Jørgensen, Carsten Brink, Henrik S Thomsen, and Rasmus Hvass Hansen. Safety of gadolinium based contrast agents in magnetic resonance imaging-guided radiotherapy–an investigation of chelate stability using relaxometry. *Physics and imaging in radiation oncology*, 21:96–100, 2022.

Timothy D Malouff, Danushka S Seneviratne, Daniel K Ebner, William C Stross, Mark R Waddle, Daniel M Trifiletti, and Sunil Krishnan. Boron neutron capture therapy: a review of clinical applications. *Frontiers in oncology*, 11:601820, 2021.

Edwin M McMillan. The synchrotron—a proposed high energy particle accelerator. *Physical Review*, 68(5-6):143, 1945.

Chul Hee Min, Han Rim Lee, Chan Hyeong Kim, and Se Byeong Lee. Development of array-type prompt gamma measurement system for in vivo range verification in proton therapy. *Medical physics*, 39(4):2100–2107, 2012.

M.J.Berger, J.S. Coursey, M.A. Zucke, and J. Chang. Stopping-powers and range tables for electrons, protons, and helium ions, nist standard reference database 124, 2017.

Martina Moglioni, Aafke Christine Kraan, Guido Baroni, Giuseppe Battistoni, Nicola Belcari, Andrea Berti, Pietro Carra, Piergiorgio Cerello, Mario Ciocca, Angelica De Gregorio, et al. In-vivo range verification analysis with in-beam pet data for patients treated with proton therapy at cnao. *Frontiers in Oncology*, 12:929949, 2022.

M Muramatsu and A Kitagawa. A review of ion sources for medical accelerators. *Review of Scientific Instruments*, 83(2), 2012.

J Narayanaswamy, P Dyer, SR Faber, and Sam M Austin. Production of 6.13-mev gamma rays from the o 16 (p, p′ γ) o 16 reaction at 23.7 and 44.6 mev. *Physical Review C*, 24 (6):2727, 1981.

Wayne D Newhauser and Rui Zhang. The physics of proton therapy. *Physics in Medicine & Biology*, 60(8):R155, 2015.

NuDat. National Nuclear Data Center, Brookhaven National Laboratory, 2024. URL `https://www.nndc.bnl.gov/nudat/`. Accessed: 2024-11-03.

American Association of Physicists in Medicine et al. Diode in vivo dosimetry for patients receiving external beam radiation therapy. *AAPM Report*, 87, 2005.

OncoRay. Prototype for high-contrast live imaging in proton therapy. `https://tu-dresden.de/tu-dresden/newsportal/news/prototyp-zur-hochkontrast-live-bildgebung-in-der-protonentherapie?set_language=en`, 2024. Accessed: 2024-11-22.

D. Ondreka and U. Weinrich. The heidelberg ion therapy (hit) accelerator coming into operation. *European Physical Society Accelerator Group, Proceedings of EPAC*, pages 23–27, 2008.

Harald Paganetti. Range uncertainties in proton therapy and the role of monte carlo simulations. *Physics in Medicine & Biology*, 57(11):R99, 2012.

K Parodi, Wolfgang Enghardt, and T Haberer. In-beam pet measurements of β+ radioactivity induced by proton beams. *Physics in Medicine & Biology*, 47(1):21, 2001.

Particle Therapy Co-Operative Group. Ptcog: Particle therapy co-operative group. `https://ptcog.ch`. Accessed: 2024-11-11.

H Paul and O Bolik. Fitted empirical reference cross sections for k-shell ionization by alpha particles. *Atomic data and nuclear data tables*, 54(1):75–131, 1993.

Helmut Paul and Josef Sacher. Fitted empirical reference cross sections for k-shell ionization by protons. *Atomic Data and Nuclear Data Tables*, 42(1):105–156, 1989.

F. Pedregosa, G. Varoquaux, A. Gramfort, V. Michel, B. Thirion, O. Grisel, M. Blondel, P. Prettenhofer, R. Weiss, V. Dubourg, J. Vanderplas, A. Passos, D. Cournapeau, M. Brucher, M. Perrot, and E. Duchesnay. Scikit-learn: Machine learning in Python. *Journal of Machine Learning Research*, 12:2825–2830, 2011.

Sébastien Penninckx, Félicien Hespeels, Julien Smeets, Julien L Colaux, Stéphane Lucas, and Anne-Catherine Heuskin. Metallic nanoparticles: A useful prompt gamma emitter for range monitoring in proton therapy? *Radiation*, 1(4):305–316, 2021.

Johannes Petzoldt, KE Roemer, Wolfgang Enghardt, Fine Fiedler, Christian Golnik, Fernando Hueso-Gonzalez, S Helmbrecht, T Kormoll, H Rohling, J Smeets, et al. Characterization of the microbunch time structure of proton pencil beams at a clinical treatment facility. *Physics in Medicine & Biology*, 61(6):2432, 2016.

Trang Thanh Pham, Brendan Whelan, Bradley M Oborn, Geoff P Delaney, Shalini Vinod, Caterina Brighi, Michael Barton, and Paul Keall. Magnetic resonance imaging (mri) guided proton therapy: A review of the clinical challenges, potential benefits and pathway to implementation. *Radiotherapy and Oncology*, 170:37–47, 2022.

Pierluigi Piersimoni, Bruce A Faddegon, José Ramos Méndez, Reinhard W Schulte, Lennart Volz, and Joao Seco. Helium ct: Monte carlo simulation results for an ideal source and detector with comparison to proton ct. *Medical physics*, 45(7):3264–3274, 2018.

Ervin B Podgoršak et al. *Radiation physics for medical physicists*, volume 1. Springer, 2006.

Jerimy C Polf, Rajesh Panthi, Dennis S Mackin, Matt McCleskey, Antti Saastamoinen, Brian T Roeder, and Sam Beddar. Measurement of characteristic prompt gamma rays emitted from oxygen and carbon in tissue-equivalent samples during proton beam irradiation. *Physics in Medicine & Biology*, 58(17):5821, 2013.

Gerd Puehlhofer, Christian Bauer, Sabrina Bernhard, Massimo Capasso, Sebastian Diebold, Felix Eisenkolb, Daniel Florin, Christian Föhr, Stefan Funk, Arno Gadola, et al. Flashcam: a fully-digital camera for the medium-sized telescopes of the cherenkov telescope array. *arXiv preprint arXiv:1509.02434*, 2015.

Y Rahma, S Ouichaoui, J Kiener, EA Lawrie, JJ Lawrie, V Tatischeff, A Belhout, D Moussa, W Yahia-Cherif, H Benhabiles-Mezhoud, et al. γ-ray emission in proton-induced nuclear reactions on natc and mylar targets over the incident energy range, ep= 30–200 mev. astrophysical implications. *Nuclear Physics A*, 1032:122622, 2023.

Christian Richter, G Pausch, S Barczyk, M Priegnitz, I Keitz, J Thiele, J Smeets, F Vander Stappen, L Bombelli, C Fiorini, et al. First clinical application of a prompt gamma based in vivo proton range verification using a knife-edge slit camera. *Radiotherapy and Oncology*, 118:S89–S90, 2016.

K Roemer, G Pausch, D Bemmerer, M Berthel, A Dreyer, C Golnik, F Hueso-González, T Kormoll, J Petzoldt, H Rohling, et al. Characterization of scintillator crystals for usage as prompt gamma monitors in particle therapy. *Journal of Instrumentation*, 10(10): P10033, 2015.

CG Ryan, E Clayton, WL Griffin, SH Sie, and DR Cousens. Snip, a statistics-sensitive background treatment for the quantitative analysis of pixe spectra in geoscience applications. *Nuclear Instruments and Methods in Physics Research Section B: Beam Interactions with Materials and Atoms*, 34(3):396–402, 1988.

Uwe Scheeler, C Krantz, S Sievers, M Strohmeier, Thomas Haberer, R Cee, E Feldmeier, M Galonska, K Höppner, J Mosthaf, et al. Recommissioning of the marburg ion-beam therapy centre (mit) accelerator facility. In *Proc. 7th Intl. Particle Accelerator Conf.(IPAC'16)*, pages 1908–1910, 2016.

Uwe Schneider and Eros Pedroni. Proton radiography as a tool for quality control in proton therapy. *Medical physics*, 22(4):353–363, 1995.

Reinhard Schulte, Vladimir Bashkirov, Tianfang Li, Zhengrong Liang, Klaus Mueller, Jason Heimann, Leah R Johnson, Brian Keeney, HF-W Sadrozinski, Abraham Seiden, et al. Conceptual design of a proton computed tomography system for applications in proton radiation therapy. *IEEE Transactions on Nuclear Science*, 51(3):866–872, 2004.

A Schumann, J Petzoldt, P Dendooven, W Enghardt, C Golnik, F Hueso-González, T Kormoll, G Pausch, K Roemer, and F Fiedler. Simulation and experimental verification of prompt gamma-ray emissions during proton irradiation. *Physics in Medicine & Biology*, 60(10):4197, 2015.

Stephen M Seltzer and Martin J Berger. Improved bremsstrahlung cross sections for transport calculations. *IEEE Transactions on Nuclear Science*, 30(6):4368–4370, 1983.

Julien Smeets, F Roellinghoff, D Prieels, F Stichelbaut, A Benilov, C Fiorini, Roberta Peloso, M Basilavecchia, Tommaso Frizzi, JC Dehaes, et al. Prompt gamma imaging with a slit camera for real-time range control in proton therapy. *Physics in Medicine & Biology*, 57(11):3371, 2012.

Giancarlo Sportelli, Nicola Belcari, Niccolo' Camarlinghi, GAP Cirrone, G Cuttone, S Ferretti, A Kraan, JE Ortuño, F Romano, A Santos, et al. First full-beam pet acquisitions in proton therapy with a modular dual-head dedicated system. *Physics in Medicine & Biology*, 59(1):43, 2013.

F Stichelbaut and Y Jongen. Verification of the proton beam position in the patient by the detection of prompt gamma-rays emission. In *39th Meeting of the Particle Therapy Co-Operative Group*, volume 16, 2003.

John R Styczynski. *Assessment of the use of prompt gamma emission for proton therapy range verification*. PhD thesis, Massachusetts Institute of Technology, 2009.

Hideaki Tashima, Eiji Yoshida, Yuma Iwao, Hidekatsu Wakizaka, Akram Mohammadi, Munetaka Nitta, Atsushi Kitagawa, Taku Inaniwa, Fumihiko Nishikido, Atsushi B Tsuji, et al. Development of a multiuse human-scale single-ring openpet system. *IEEE Transactions on Radiation and Plasma Medical Sciences*, 5(6):807–816, 2020.

M Testa, M Bajard, M Chevallier, D Dauvergne, N Freud, P Henriquet, S Karkar, F Le Foulher, JM Létang, R Plescak, et al. Real-time monitoring of the bragg-peak position in ion therapy by means of single photon detection. *Radiation and environmental biophysics*, 49:337–343, 2010.

David J Thomas. Icru report 85: fundamental quantities and units for ionizing radiation, 2012.

Liheng Tian, Guillaume Landry, Georgios Dedes, Florian Kamp, Marco Pinto, Katharina Niepel, Claus Belka, and Katia Parodi. Toward a new treatment planning approach accounting for in vivo proton range verification. *Physics in Medicine & Biology*, 63(21): 215025, 2018.

Mahboob Ur Rehman, Omar A Zeidan, Twyla Willoughby, Sanford L Meeks, Patrick Kelly, and Kevin Erhart. Dosimetric comparison of various spot placement techniques in proton pencil beam scanning. *International Journal of Particle Therapy*, 9(1):54–63, 2022.

U.S. Food and Drug Administration. Dotarem (gadoteric acid) Prescribing Information, 2017. URL `https://www.accessdata.fda.gov/drugsatfda_docs/label/2017/204781s001lbl.pdf`. Accessed: 2024-11-08.

Kurt W Van Delinder, Daniel Crawford, Tiezhi Zhang, Rao Khan, and James L Gräfe. Investigating neutron activated contrast agent imaging for tumor localization in proton therapy: a feasibility study for proton neutron gamma-x detection (pngxd). *Physics in Medicine & Biology*, 65(3):035005, 2020.

VI Veksler. The principle of coherent acceleration of charged particles. *The Soviet Journal of Atomic Energy*, 2(5):525–528, 1957.

Joost M Verburg, Helen A Shih, and Joao Seco. Simulation of prompt gamma-ray emission during proton radiotherapy. *Physics in Medicine & Biology*, 57(17):5459, 2012.

Joost M Verburg, Kent Riley, Thomas Bortfeld, and Joao Seco. Energy-and time-resolved detection of prompt gamma-rays for proton range verification. *Physics in Medicine & Biology*, 58(20):L37, 2013.

Pauli Virtanen, Ralf Gommers, Travis E. Oliphant, Matt Haberland, Tyler Reddy, David Cournapeau, Evgeni Burovski, Pearu Peterson, Warren Weckesser, Jonathan Bright, Stéfan J. van der Walt, Matthew Brett, Joshua Wilson, K. Jarrod Millman, Nikolay Mayorov, Andrew R. J. Nelson, Eric Jones, Robert Kern, Eric Larson, C J Carey, İlhan Polat, Yu Feng, Eric W. Moore, Jake VanderPlas, Denis Laxalde, Josef Perktold, Robert Cimrman, Ian Henriksen, E. A. Quintero, Charles R. Harris, Anne M. Archibald, Antônio H. Ribeiro, Fabian Pedregosa, Paul van Mulbregt, and SciPy 1.0 Contributors. SciPy 1.0: Fundamental Algorithms for Scientific Computing in Python. *Nature Methods*, 17:261–272, 2020.

L Volz, CA Collins-Fekete, E Bär, S Brons, C Graeff, RP Johnson, A Runz, C Sarosiek, RW Schulte, and J Seco. The accuracy of helium ion ct based particle therapy range prediction: an experimental study comparing different particle and x-ray ct modalities. *Physics in Medicine & Biology*, 66(23):235010, 2021.

Lennart Volz. *Particle imaging for daily in-room image guidance in particle therapy*. PhD thesis, Heidelberg University, 2021.

Lennart Volz, Laurent Kelleter, Stephan Brons, L Burigo, C Graeff, NI Niebuhr, R Radogna, S Scheloske, C Schömers, S Jolly, et al. Experimental exploration of a mixed helium/carbon beam for online treatment monitoring in carbon ion beam therapy. *Physics in Medicine & Biology*, 65(5):055002, 2020.

Christopher John Werner, Jerawan Chudoung Armstrong, Forrest Brooks Brown, Jeffrey S. Bull, Laura Casswell, Lawrence James Cox, David A. Dixon, Robert Arthur Forster, III, John Timothy Goorley, Henry Grady Hughes, III, Jeffrey A. Favorite,

Roger Lee Martz, Stepan Georgievich Mashnik, Michael Evan Rising, Clell Jeffrey Solomon, Jr., Avneet Sood, Jeremy Ed Sweezy, Anthony J. Zukaitis, Casey Alan Anderson, Jay Samuel Elson, Joe W. Durkee, Jr., Russell Craig Johns, Gregg Walter McKinney, Garrett Earl McMath, John S. Hendricks, Denise B. Pelowitz, Richard Edward Prael, Thomas Edward Booth, Michael R. James, Michael Lorne Fensin, Trevor A. Wilcox, and Brian Christopher Kiedrowski. MCNP User's Manual Code Version 6.2. Technical Report LA-UR-17-29981, Los Alamos National Laboratory, Los Alamos, NM, USA, 2017. URL `http://permalink.lanl.gov/object/tr?what=info:lanl-repo/lareport/LA-UR-17-29981`.

Christopher John Werner, Jeffrey S Bull, Clell Jeffrey Solomon, Forrest B Brown, Gregg Walter McKinney, Michael Evan Rising, David A Dixon, Roger Lee Martz, Henry G Hughes, Lawrence James Cox, et al. Mcnp version 6.2 release notes. Technical report, Los Alamos National Laboratory (LANL), Los Alamos, NM (United States), 2018.

TA Wilcox, GW McKinney, and T Kawano. Mcnp6 gets correlated with cgm 3.4-paper 41. Technical report, American Nuclear Society-ANS, 555 North Kensington Avenue, La Grange Park, 2014. URL `https://www.osti.gov/biblio/23082883`.

Aleksandra Wrońska, Jonas Kasper, Arshiya Anees Ahmed, Achim Andres, Piotr Bednarczyk, Grzegorz Gazdowicz, Katrin Herweg, Ronja Hetzel, Adam Konefał, Paweł Kulessa, et al. Prompt-gamma emission in geant4 revisited and confronted with experiment. *Physica Medica*, 88:250–261, 2021.

Yunhe Xie, El Hassane Bentefour, Guillaume Janssens, Julien Smeets, François Vander Stappen, Lucian Hotoiu, Lingshu Yin, Derek Dolney, Stephen Avery, Fionnbarr O'Grady, et al. Prompt gamma imaging for in vivo range verification of pencil beam scanning proton therapy. *International Journal of Radiation Oncology* Biology* Physics*, 99 (1):210–218, 2017.

Hiroki Yoneda, Felix Aharonian, Paolo Coppi, Thomas Siegert, and Tadayuki Takahashi. Line profile of nuclear de-excitation gamma-ray emission from very hot plasma. *Monthly Notices of the Royal Astronomical Society*, 526(1):1460–1470, 2023.

EF Zganjar and JL Wood. Electric monopole transitions: What they can tell us about nuclear structure. In *ENAM 95: International Conference on Exotic Nuclei and Atomic Masses: Arles, France, June 19-23, 1995*, page 437. Atlantica Séguier Frontières, 1995.

Zhuxian Zhou and Zheng-Rong Lu. Gadolinium-based contrast agents for magnetic reso-

nance cancer imaging. *Wiley Interdisciplinary Reviews: Nanomedicine and Nanobiotechnology*, 5(1):1–18, 2013.

Klemens Zink, Kilian Simon Baumann, Ulrike Theiss, Florentine Subtil, Sonja Lahrmann, Fabian Eberle, and Sebastian Adeberg. Organization and operation of multi particle therapy facilities: the marburg ion-beam therapy center, germany (mit). *Health and Technology*, pages 1–10, 2024.

Acknowledgments

Since the beginning of my Ph.D. program, I relied on the support of countless people and institutions, which help me to achieve this moment and to whom I am very grateful. To Professor Doctor João Seco I thank you for the monitoring, support and sharing of valuable knowledge for this work. To the group Biomedical Physics in Radiation Oncology, I thank you for all the support and friendship. To the institute Deutsches Krebsforschungszentrum for the logistical and human support given during my dissertation. To the institutes Heidelberg Ion-Therapy Center and Marburg Ion-Therapy Center, and its service of medical physics, Dr. Stephan Brons and Dr. Kilian Baumann. Special thanks to my great friends and all others who have a mutual friendship. The greatest thanks go to those who continue to believe in me and have supported me at all times Rui Mendes, Ana Lindade, my parents, my brother, all my grandparents, and the whole family.

This work was supported by FCT under a PhD grant of reference 2020.05031.BD (https://doi.org/10.54499/2020.05031.BD).